Broadband Planar Waveguide to Vertical Mode Couplers

Ross Cassells

Institute of Photonics

Physics

University of Strathclyde, Glasgow

January 30, 2026

Abstract

The research presented in this thesis focuses on the development of a broadband and low loss vertical coupling regime for photonic integrated circuits, using a combination of laser lithography and grayscale lithography. Existing coupling regimes in photonic integration often struggle to meet four key requirements: low optical loss, broad spectral bandwidth, rapid fabrication turnaround, and wafer scale testability. To address this, a low cost platform based on SU8 on glass was fabricated, employing a multistage process with grayscale lithography to realise 2.5D turning mirrors at 45°, coated with a highly reflective thin film comprising 50 nm titanium and 200 nm gold. Planar SU8 waveguides were fabricated to embed the turning mirrors, enabling a broadband edge coupled waveguide to vertical mirror architecture. Optical characterisation of these devices was carried out across a wavelength range of 516 to 1630 nm, with measurements of facet coupling losses, propagation losses, and additional mirror related coupling losses. The optical losses introduced by the mirror across the measured spectral band were below 1 dB when collected in free space. For wafer scale testability, direct coupling to single mode fibre at 1550 nm was demonstrated with losses of 0.8 dB. Finally, hybrid integration of the waveguide vertical couplers was achieved through additional microfabrication and transfer printing of μLEDs and VCSEL arrays. Successful probing of these active photonic devices was achieved, and end facet imaging was recorded.

Contents

List of Figures

List of Tables

Acknowledgements

I would first like to express my deepest gratitude to my supervisor, Prof. Michael Strain, for his invaluable guidance, encouragement, and unwavering support throughout the entirety of my PhD. His mentorship has been central not only to the work presented in this thesis but also to my development as a researcher. Words cannot fully convey my appreciation for all he has done.

I am also sincerely grateful to Dr. Ian Watson, Dr. Benoit Guilhabert, Dr. Yunzhou Cheng, Dr. Jack Smith, and Mr. Ronnie Roger for their expertise and assistance within the cleanroom. Their support with training, fabrication, and operation has been essential in enabling myself and others to carry out research effectively. I would particularly like to thank Dr. Jack Smith for his further guidance and training in the optics laboratory. My thanks also extend to Sharon Kelly and Lorraine Annand for their excellent administrative support and to Leanore Ferrans and the rest of the IT department for all the IT support over the years.

I would like to thank those involved with the research contribution related to the integration of active photonic devices with the waveguide mirror devices. Dr. Zubair Ahmed, Dr. Eleni Margariti, Dr. Sean Bommer and Dr. Benoit Guilhabert for the integration of VCSELs, and finally to Dr. Zhongyi Xia for the integration and testing of μLED devces.

The pursuit of a PhD naturally comes with both challenges and triumphs, and I am profoundly grateful to my close friends and family for their constant encouragement throughout this journey. I would also like to acknowledge my secondary school teachers in Mathematics and Physics, whose support, guidance, and inspiration laid the foundations that ultimately led me to pursue this path in research.

Finally, I wish to thank my partner, Monica, for her unwavering love, patience, and support.

Chapter 1

Introduction

1.1 Motivation

The rapid growth in global data consumption, driven by cloud services, artificial intelligence, autonomous systems, and emerging communication networks, has led to unprecedented demand for high performance and energy efficient information technologies [1, 2]. At the same time, society increasingly relies on portable and compact devices that demand reduced power consumption and enhanced functionality without sacrificing performance. Meeting these requirements with purely electronic solutions is becoming increasingly difficult, as the scaling of transistor dimensions approaches fundamental physical limits and data transfer between transistors increasingly dominates system power consumption and latency. The historical trend described by Moore's law, which has predicted the doubling of transistor density every two years [3] (fig. 1.1), is slowing as devices shrink to only a few nanometres in size. At such dimensions, quantum mechanical effects such as tunnelling, along with leakage currents, compromise device reliability and efficiency [4]. In addition, conventional copper interconnects face fundamental bandwidth and energy efficiency limitations, forming a critical bottleneck for further scaling of high-performance computing systems. This has created an urgent need to explore alternative or complementary technologies that can continue to advance information processing and communication performance.

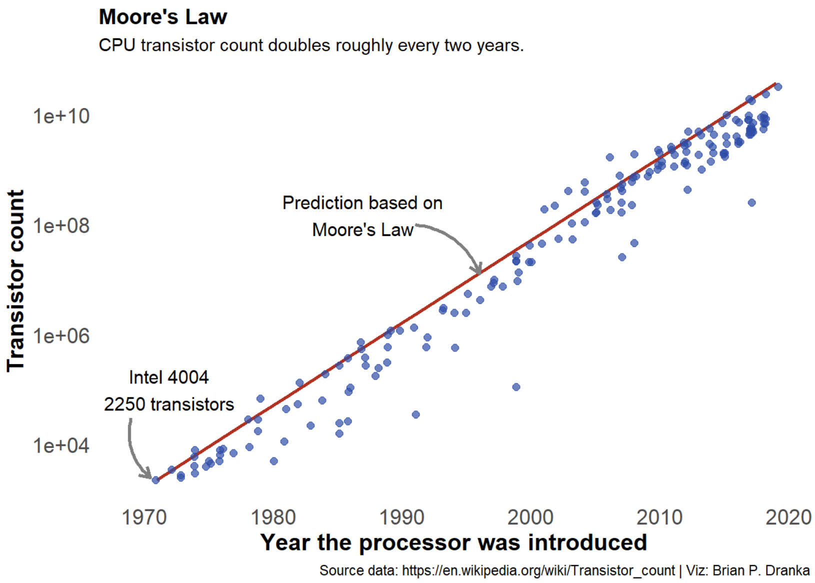

Figure 1.1: Prediction of Moore's law and transistor count. Credit: [5]

Photonic technologies have emerged as a promising candidate to meet these demands [6, 7] ,particularly as a means of alleviating interconnect bottlenecks through optical data transfer.. Unlike electronics, which rely on the movement of charge carriers, photonics uses light to transfer and process information. Photons travel at the speed of light, do not suffer from resistive heating, and can propagate without electrical crosstalk, making them inherently suited for high-speed and low-power operation. These advantages have motivated significant interest in co-packaged and chip-scale electro-optic integration [8], where photonic components are placed in close proximity to electronic processors to reduce interconnect energy and latency. These attributes position photonic systems as enabling technologies for applications such as high bandwidth communication links [9], optical signal processing [10], quantum information science [11], and precision sensing [12]. Beyond data communication, photonic computing has also been proposed as a longer-term paradigm for accelerating specific classes of computation, offering a potential future complement to electronic processors [13].

Photonic integrated circuits are the leading platform for realising such systems on a compact and scalable chip scale [14, 15]. They combine passive elements, such as optical waveguides, splitters, and filters, with active devices, including modulators, detectors, and light sources, to perform complex optical functions. A central feature of any photonic integrated circuit is the optical waveguide, which confines and guides light in a controlled manner across the chip [16]. To interface with the external world, efficient coupling strategies are required to connect the waveguides to optical fibres or free space beams, enabling light to be injected into and extracted from the circuit [17, 18]. These building blocks, when fabricated using techniques adapted from semiconductor manufacturing, allow dense integration of diverse optical components on a single platform [19]. The combination of high functional density, potential for wafer scale fabrication, and compatibility with existing electronic integration strategies makes photonic integrated circuits a critical technology for the next generation of information processing and communication systems [20, 21].

1.2 The Road to Photonic Integrated Circuit Manufacturing

1.2.1 Photonic Circuits

To understand the manipulation of light, it is useful to return to one of the earliest principles of optics: Snell's law. Formulated in the seventeenth century, it quantifies the relationship between the angle of incidence θ_i and the angle of refraction θ_t when light passes between two media of refractive indices n_1 and n_2:

$$n_1 \sin\theta_i = n_2 \sin\theta_t.$$

A pivotal phenomenon arising from this law is total internal reflection (TIR), first studied in the nineteenth century. TIR occurs when light propagating in a medium of higher refractive index encounters an interface with a medium of lower refractive index at an angle greater than the critical angle, given by

$$\theta_c = \sin^{-1}\left(\frac{n_2}{n_1}\right).$$

Above this angle, no refraction occurs and light is completely reflected. This principle underpins the operation of both optical fibres and integrated optical waveguides [22]. For example, fig. 1.2, shows the path light takes as TIR takes place, allowing for light to propagate in a confined medium. The twentieth century saw the first practical exploitation of TIR in the development of optical fibres, which enabled low-loss transmission of light over long distances [23]. It is important to note that this is a simplified explanation and for nano/micro photonic devices, Maxwell's equations give a full description

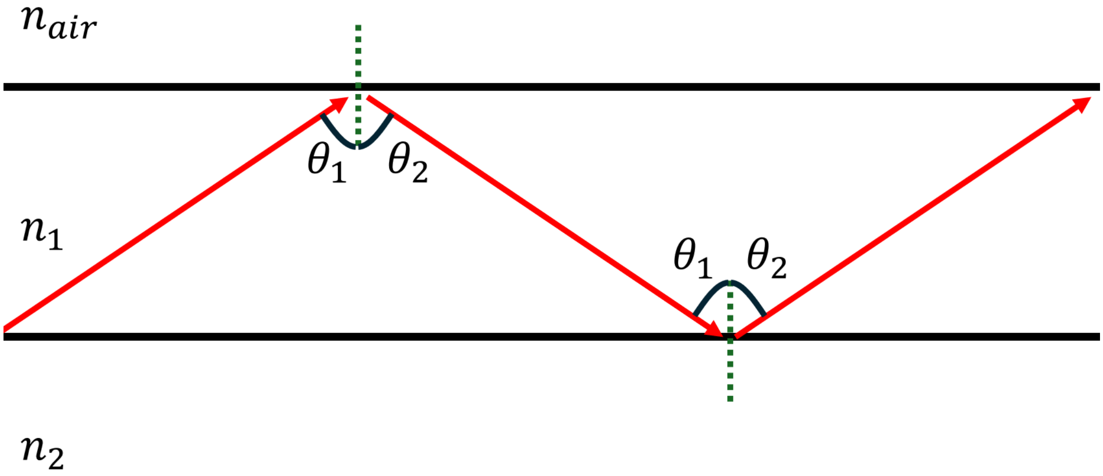

Figure 1.2: Illustration of TIR as a ray diagram in a photonic waveguide

The subsequent miniaturisation of optical components on chip-scale platforms was made possible by advances in semiconductor processing [24, 25]. Planar waveguide technologies extended the concepts of fibre guidance into lithographically defined structures, allowing precise control of optical confinement and circuit topology. Crucially, the integration of low-loss waveguides [26], efficient couplers [27], and high-speed modulators [28] enabled the realisation of functional photonic circuits. Grating couplers, which use periodic surface structures to scatter light between a waveguide and an optical fibre, provided a practical means of fibre-to-chip interfacing, while edge couplers offered an alternative approach through adiabatic tapering of the waveguide. For signal modulation, devices such as Mach–Zehnder interferometers, based on the controlled interference of two optical paths, and ring resonators, which exploit wavelength-selective resonance in a closed loop waveguide, became central components.

Furthermore, heterogeneous integration techniques [29], including wafer bonding and epitaxial growth, facilitated the inclusion of III–V semiconductor materials for active components such as lasers and detectors on silicon substrates. The maturation of these approaches has led to photonic integrated circuits that combine passive routing elements with active light sources and detectors, enabling compact, high-speed, and energy-efficient optical systems [30, 31, 32].

Today, photonic integrated circuits are pivotal in a wide range of applications, from high-speed data communications and quantum photonics to biosensing and LIDAR. Their development represents the culmination of centuries of optical science and a testament to the interplay between physics, materials science, and engineering.

1.3 Material Platforms

1.3.1 Silicon

Silicon on Insulator (SOI) has established itself as a leading platform for the development of photonic integrated circuits (PICs), due to its unique combination of material properties, fabrication compatibility with standard silicon-based manufacturing processes [33, 34, 35, 36], and optical performance. The platform's rise is closely tied to the maturity of CMOS electronics manufacturing, from which it inherits both the infrastructure and design principles, allowing photonic devices to be fabricated with high precision and reproducibility at wafer scale [9]. Silicon photonics is a $10bn industry with current state of the art photonic waveguides being 100-500nm thick [37]. This section provides a comprehensive exploration of SOI as a photonic platform, focusing on its structural features, wave-guiding properties, fabrication methods, key advantages, limitations, and its critical role in the evolution of integrated optics.

At the core of the SOI platform lies a three layer material stack comprising a top silicon device layer, a buried oxide (BOX) layer, and a silicon substrate, as illustrated in fig. 1.3.

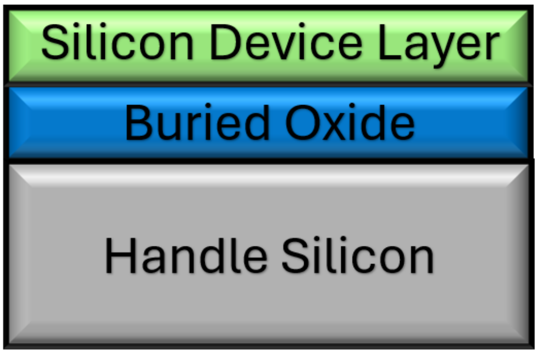

Figure 1.3: SOI platform material stack

The device layer, typically between 100 and 500 nanometres in thickness, acts as the optical guiding medium and is where photonic devices are patterned. Beneath this lies the BOX, usually around 2 microns thick, which serves to isolate the guiding layer from the silicon substrate and prevent leakage of the optical mode. The large refractive index contrast between silicon (n = 3.48 at 1550 nm) and silicon dioxide (n = 1.44) leads to strong confinement of light, enabling sub-micron waveguides and tight waveguide bend radii [38, 39]. An example of the highly confined waveguide mode and tight bend radii by Dong, et. al., is shown in fig. 1.4 with COMSOL simulations and SEM images of fabricated devices.

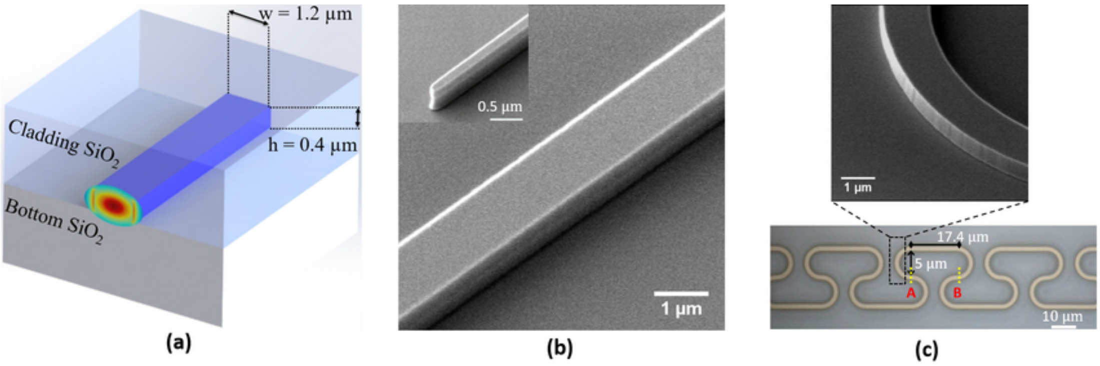

Figure 1.4: (a) Schematic of SOI waveguide mode simulated using COMSOL. (b) SEM image of straight waveguide. (c) Optical and SEM image of waveguide radii bend of 5um. Credit: [38]

These properties allow dense integration of photonic components, a key requirement for miniaturised and complex circuits. Furthermore, silicon's transparency window in the near infrared - from roughly 1.1 to 8 microns makes it particularly suitable for applications in the telecom bands, especially around 1310 and 1550 nm.

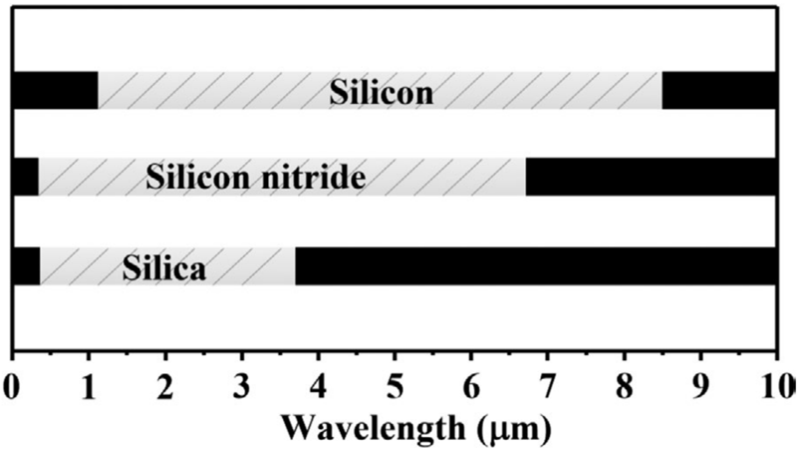

Figure 1.5: Material absorption characteristics of silicon, silicon nitride, and silica are shown. The shaded regions indicate the optically transparent windows, while the black regions denote wavelength ranges with high absorption loss. Credit: [36]

SOI photonic circuits are typically fabricated using processes adapted directly from CMOS technology, which allows for high volume and cost effective production [9]. Device patterns are defined using lithographic techniques such as deep or extreme ultraviolet (DUV, EUV) photolithography or electron beam lithography. The defined patterns are then transferred into the silicon device layer using reactive ion etching (RIE), often employing inductively coupled plasma (ICP) to achieve vertical sidewalls and minimise scattering losses [39]. Outlined in fig. 1.6, is a typical fabrication process for SOI waveguides. For active devices, such as modulators and photodetectors, doping is achieved through ion implantation followed by thermal annealing, and electrical contacts are formed by standard metallisation techniques [40]. The availability of process design kits (PDKs) and multi project wafer (MPW) services has played a key role in democratising access to SOI foundries, allowing research groups and start-ups to fabricate high performance PICs without having to invest in full scale fabrication facilities [9].

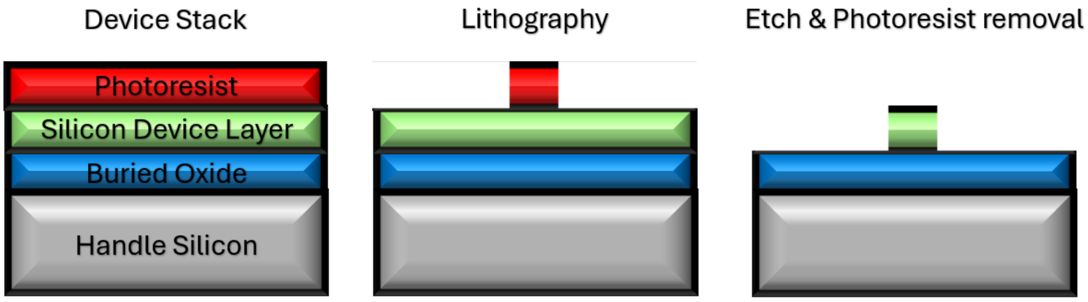

Figure 1.6: Structure and fabrication process of Silicon photonic wire waveguide.

However, because of silicon's indirect bandgap, achieving an efficient on-chip photon source has been a long-standing challenge [21]. This limitation has motivated extensive research into hybrid and heterogeneous integration of III–V semiconductors with SOI, an approach that is now central to the development of fully integrated silicon photonic platforms.

1.3.2 SiN

Silicon nitride (SiN) has emerged as a highly promising material platform for photonic integrated circuits (PICs), particularly in applications that require low optical loss, wide transparency windows, and robust environmental stability [41, 42]. Unlike the high index contrast and strong nonlinearity associated with silicon on insulator (SOI), silicon nitride offers complementary advantages that have made it increasingly attractive for both research and commercial applications. These include ultra low propagation losses (<dB/m) in the IR [43] broad spectral coverage extending from the visible to the mid infrared [44], and compatibility with CMOS fabrication infrastructure [45]. As the field of integrated photonics continues to diversify beyond telecommunications, silicon nitride has established itself as a versatile platform for precision photonics, biosensing, quantum optics, and nonlinear optical signal processing.

The fundamental appeal of silicon nitride lies in its optical and material properties. With a refractive index of approximately 2 in the near infrared, it provides moderate index contrast when paired with silicon dioxide cladding (n = 1.44), resulting in larger mode areas compared to Silicon, but still being highly confined and reduced sensitivity to fabrication imperfections [46]. This moderate confinement allows the design of low-loss waveguides that can tolerate variations in etch depth, sidewall roughness, and film thickness, making the platform highly manufacturable and robust.An example of a simulated SiN waveguide mode structure is shown in fig. 1.7 with an oxide cladding layer.

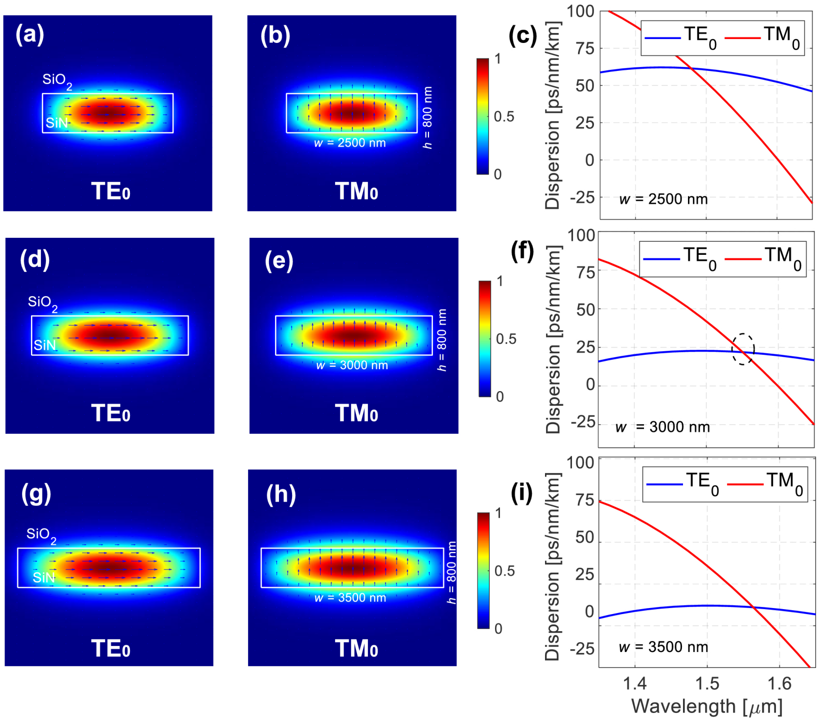

Figure 1.7: SiN waveguide TE and TM mode simulation. Credit: [47]

One of the most significant advantages of silicon nitride is its extremely low optical propagation loss, which can reach below 0.1 dB/m in optimised conditions [43]. This is achieved through the use of high temperature annealing processes that remove hydrogen and other residual impurities from the film, thereby minimising absorption at telecom and visible wavelengths. Such performance is critical in applications requiring long optical delays or high-Q resonators.

The transparency window of silicon nitride spans a wide range of wavelengths, from around 400 nm in the visible spectrum to beyond 2.3 um [44] in the infrared, making it suitable for a variety of applications that extend beyond the capabilities of SOI. In

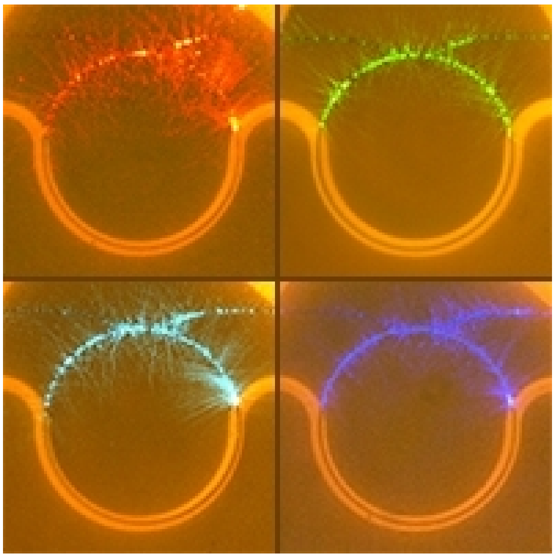

Figure 1.8: Imaged scattering of SiN waveguides across the visible spectrum. Credit: [48]

the visible regime, where silicon suffers from strong absorption, silicon nitride supports low loss guidance of light and is thus ideal for visible light PIC applications, such as, biomedical sensors for microflow cytometers. An example of the visible light application is the observation of scattering from SiN waveguides in fig. 1.8.

From a fabrication perspective, silicon nitride waveguides are typically formed using low pressure chemical vapour deposition (LPCVD), which yields SiN films with excellent optical quality [46]. However, due to the significant intrinsic stress in thick LPCVD films, special techniques such as stress management through alternating tensile and compressive layers or thermal cycling are often required to prevent wafer bowing and cracking [41]. Plasma enhanced chemical vapour deposition (PECVD) provides an alternative for lower temperature processes but generally results in higher propagation losses unless carefully optimised [43]. Patterning is carried out using electron beam or DUV lithography, followed by dry etching, typically with fluorine or chlorine-based chemistries, to define waveguides with smooth sidewalls and accurate dimensional control. Post-fabrication annealing at temperatures above 1100°C is commonly used to further reduce optical loss and improve film uniformity [41]. Typical fabrication steps used for SiN waveguides are illustrated in fig. 1.9. The relatively large mode sizes supported by SiN waveguides also facilitates fibre-to-chip coupling, allowing the use of edge couplers with adiabatic tapers that improve alignment tolerances and minimise insertion loss.

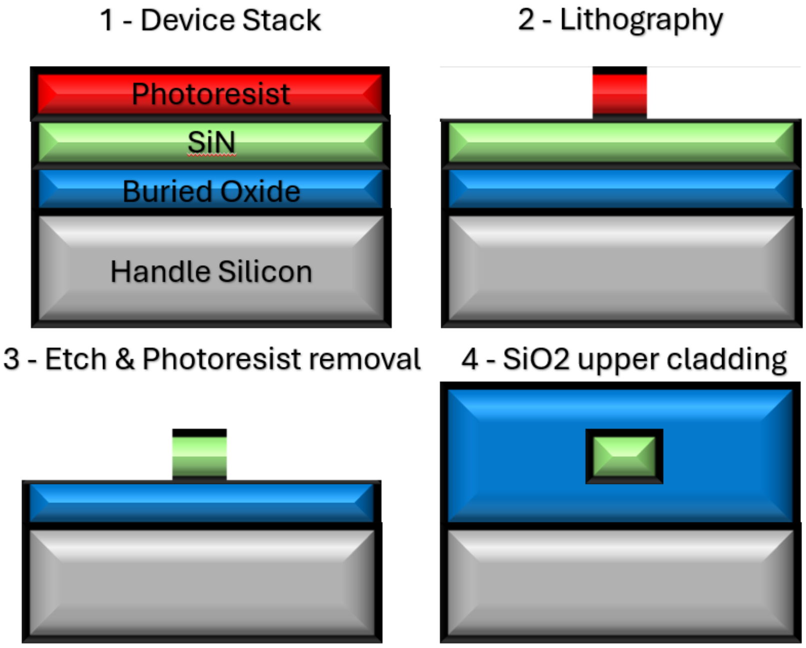

Figure 1.9: Fabrication process of SiN waveguides buried in oxide layer.

The design of silicon nitride PICs benefits from the relaxed confinement and fabrication tolerance relative to SOI. Larger waveguide dimensions based on the bulk index of the material reduce modal dispersion which is important for long range data transmission, as modal dispersion causes multiple signals to travel at different speeds - thus signals arriving at different times, and allow for the realisation of low loss bends and splitters with moderate radii [46]. While this limits the packing density of devices compared to SOI, it greatly enhances stability and reproducibility an important consideration for sensing and quantum applications where phase noise and optical coherence are essential. Additionally, the platform enables the fabrication of high finesse microring and racetrack resonators, which are widely used for wavelength selective filtering, optical delay lines, frequency comb generation, and sensing [41]. The low linear and nonlinear losses ensure that these resonators can achieve loaded Q factors in excess of one million, even in compact footprints. Yi Xuan, et. al. displayed Silicon Nitride resonators with loaded Q's up to 8.25 million [49], as indicated in fig.1.10.

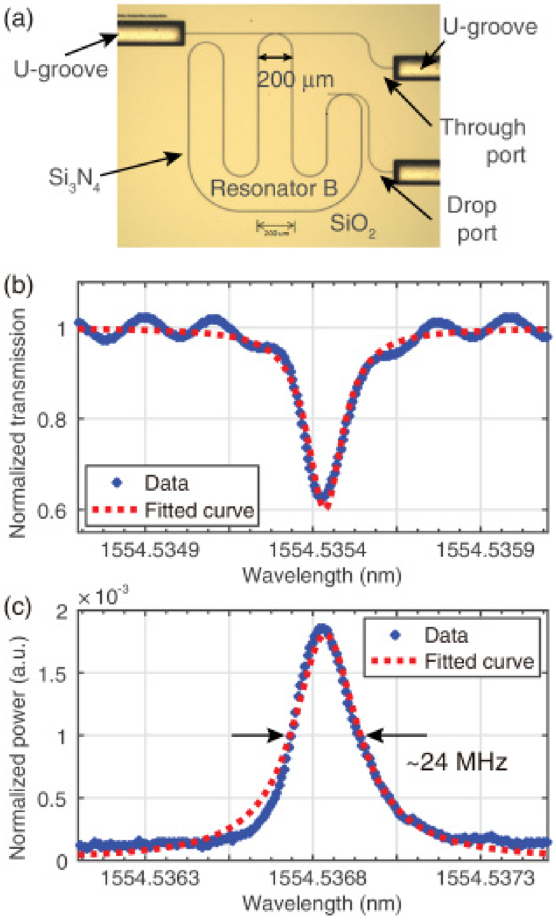

Figure 1.10: (a) Optical image of a resonator with through and drop ports (resonator B); coupling gaps are 400nm (through) and 700nm (drop). (b) Normalized through-port transmission. (c) Normalized drop-port transmission showing a loaded Q of 8.25×10^6. Spectra were recorded in separate scans, causing minor resonance wavelength differences. Credit: [49]

Silicon nitride's excellent nonlinear properties also make it a competitive platform for integrated nonlinear optics. While its nonlinear refractive index is lower than that of silicon, the absence of two photon absorption allows higher optical intensities to be used, which compensates for the lower intrinsic nonlinearity. This has led to the demonstration of efficient four wave mixing and Kerr frequency combs on chip, particularly when the waveguide dispersion is carefully engineered to support phase matching [44, 50].

Another compelling feature of silicon nitride is its compatibility with heterogeneous and hybrid integration. The moderate index contrast allows SiN waveguides to be integrated alongside silicon, lithium niobate, III–V semiconductors, or polymers within the same chip or package [42]. This enables multifunctional PICs that combine the low loss passive routing of silicon nitride with the active modulation, detection, or emission capabilities of other materials. Bonding techniques, such as adhesive bonding, direct wafer bonding, and transfer printing, allow the co-integration of various material systems with high alignment accuracy. This hybrid approach is particularly attractive in quantum photonics, where silicon nitride is often used as a low noise interconnect and interferometric platform, while sources and detectors are integrated separately.

In terms of commercial deployment, silicon nitride PICs have already found widespread adoption in fibre optic gyroscopes, narrow linewidth lasers, atomic clocks, medical diagnostics, and programmable optical processors. Foundries now offer process design kits specifically tailored to SiN, and multi project wafer runs are enabling widespread access to high quality fabrication without the need for in house cleanroom facilities. The maturity of the platform is evident in the growing number of startups and commercial players offering silicon nitride based solutions across sensing, communications, and metrology [51, 52, 53].

1.3.3 Polymers

Polymer based photonic integrated circuits (PICs) have garnered increasing interest due to their versatility, ease of fabrication, and compatibility with non traditional substrates and environments [54, 55]. Among the many polymers employed in photonic applications, SU8 stands out as a particularly promising material. Originally developed as a thick film, negative tone photoresist for microfabrication of micro-electromechanical systems (MEMS) [56], originally developed by IBM for UV lithography compatible processes, allowing for high aspect ratio features, low cost and rapid manufacturing. SU8 has become a popular choice for the realisation of optical waveguides and components, especially where low cost, rapid prototyping or large area integration is required. Its favourable optical properties, chemical stability, and lithographic flexibility make it an effective medium for both passive and active photonic devices.

SU-8 is an epoxy based thermosetting polymer that exhibits a refractive index of approximately 1.57 at 1550 nm, which is suitable for guiding light when combined with appropriate cladding materials, such as air or fluorinated polymers, that offer sufficient refractive index contrast. The material is largely transparent in the near infrared regime, with optical propagation losses typically in the range of a few dB/cm for well fabricated waveguides. This makes it suitable for short-to-medium-distance photonic interconnects and integrated optical circuits [57, 58].

One of the most appealing aspects of SU8 is the simplicity and accessibility of its fabrication process. Because SU8 can be directly patterned using standard ultraviolet lithography, optical waveguides can be formed without the need for complex etching or high temperature deposition processes [59]. A strip loaded SU-8 waveguide with an oxide buffer layer on silicon is shown in fig. 1.11, as a cross sectional SEM image of the device. Furthermore, fig. 1.12 illustrates the fabrication process of SU-8 waveguides using a direct write laser to expose the desired regions of the waveguides while the developer removes excess resists.

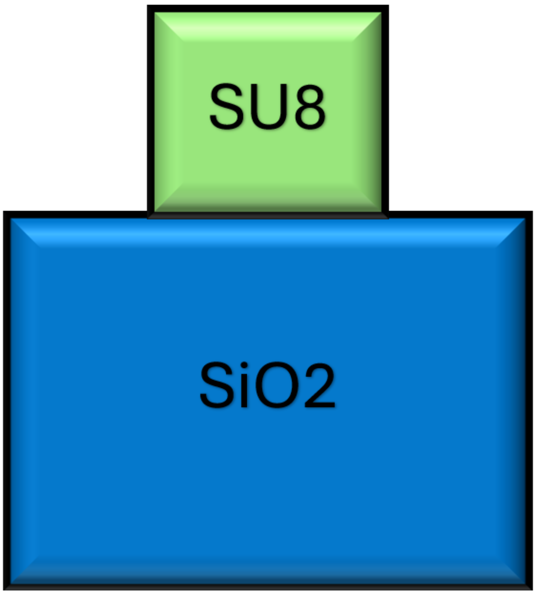

Figure 1.11: Cross section illustration of SU-8 waveguide.

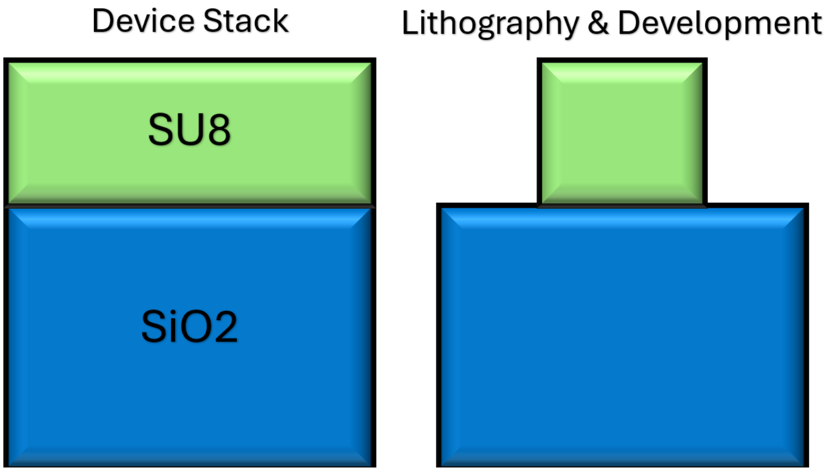

Figure 1.12: Fabrication of modified SU-8 waveguides using direct write laser lithography.

This process not only reduces fabrication time and cost, but also enables the use of substrates that would otherwise be incompatible with high temperature processing, such as plastics, glasses, or flexible materials. By adjusting the spin coating parameters, SU-8 can be deposited in thicknesses ranging from a few microns to several hundred microns, allowing for flexibility in optical mode size and confinement. This tunability is particularly useful for applications requiring large mode area waveguides for efficient fibre interfacing or for integration with free space optics [60].

Material	Propagation losses (dB/cm)	Reference
SU8	1 3 dB/cm	[61]
PMMA	4.2 dB/cm	[62]
Parylene	3.5-6.1 dB/cm	[63]

Table 1.1: Typical propagation losses for selection of polymer waveguide mediums

The mechanical and chemical robustness of cured SU 8 is another notable advantage. Once crosslinked, SU 8 exhibits high structural integrity, with excellent resistance to most solvents and acids. It also shows good adhesion to a variety of substrates, including silicon, glass, and metals, which makes it an ideal candidate for hybrid integration with other materials and platforms.

While SU-8 offers great optical properties and ease of fabrication, it is important to note some other forms of polymers that can be used for waveguides.

Polymethyl methacrylate (PMMA) is a widely used polymer in integrated photonics due to its optical transparency, ease of fabrication, and low cost. PMMA waveguides are employed in optical interconnects, lab-on-a-chip systems, and biosensors, where scalability and flexibility are important [62, 64]. They are highly transparent from 400nm to 1100nm and can be processed via spin or dip coating to form uniform films. Waveguides can be patterned with femtosecond lasers, achieving propagation losses of 4dB/cm at 632.8nm [62]. However, PMMA has limited thermal stability, with a glass transition temperature around 105°C, restricting its use in high-temperature environments [65].

Parylene, including variants such as Parylene-C and Parylene-N, is valued for chemical stability, biocompatibility, and mechanical flexibility, making it suitable for flexible or implantable photonic systems [63, 66]. Typically paired with PDMS as a cladding layer, Parylene-C is transparent in the optogenetic range (460–690nm) and has a high refractive index (n = 1.639), while PDMS has a lower index (n = 1.407), producing a strong index contrast. This enables compact, highly confining waveguides, with propagation losses ranging from 3.5dB/cm to 10dB/cm at 680nm [63].

1.3.4 Material Platform Summary

As discussed in this section, various material platforms are used for PICs, each with their own advantages and disadvantages. Table 1.1, summarises each platform, including their operating wavelengths, typical propagation losses, advantages and disadvantages.

Material Platform	**Operating Wavelengths**	**Propagation Losses**	**Advantages**	**Disadvantages**
SOI	IR	dB/m	Low loss and compatibility with existing telecom infrastructure	Incompatible with visible-wavelength PICs
SiN	VIS–IR	dB/cm–dB/m	Low loss and broadband operation	Longer fabrication time and higher cost
Polymers	VIS–IR	dB/cm	Low-cost and rapid-turnaround	High losses over large chip lengths

Table 1.2: Summary of material platforms used for PICs. IR = infrared, VIS = visible.

1.4 Off-chip Coupling Interfaces For Photonic Integrated Circuits

Off-chip coupling is a critical aspect of photonic integrated circuits, since devices must exchange light efficiently with optical fibres. The effectiveness of a coupling scheme is commonly assessed by key metrics including coupling loss, spectral bandwidth, polarisation dependence, alignment tolerance, and back reflection. Low insertion loss and broadband operation are particularly important to ensure efficient signal transfer without limiting system performance, while relaxed alignment tolerances and wafer-scale testability reduce packaging cost and enable scalable manufacturing. These requirements make the design of robust and efficient coupling strategies one of the central challenges in the development and commercialisation of photonic integrated circuits.

1.4.1 Edge Coupling

Edge coupling involves aligning the cleaved facet of an optical fibre to the polished facet of a photonic chip such that light is coupled directly into the waveguide. The effectiveness of this process hinges on the mode field diameter (MFD) matching between the fibre and the waveguide. For example, as illustrated in fig. 1.13 shows edge coupling between a fibre and a photonic waveguide.

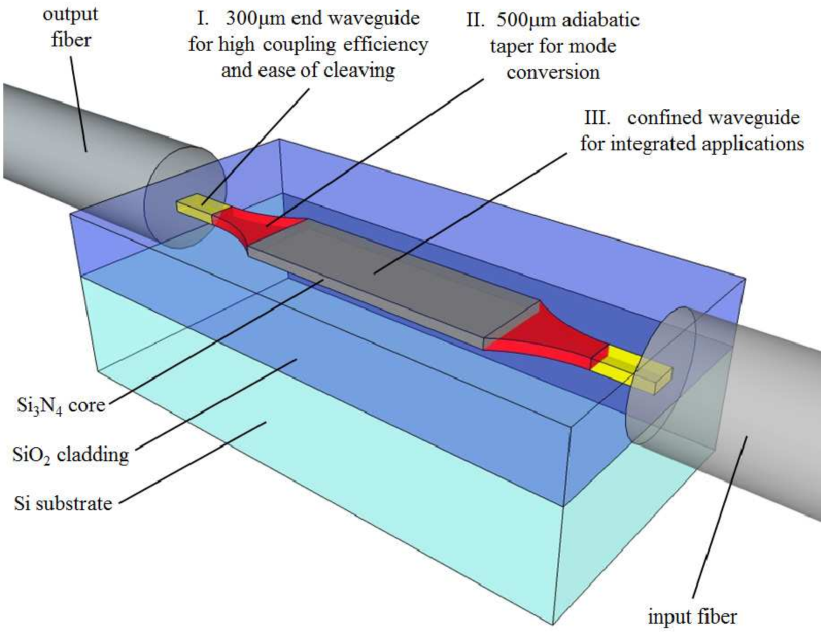

Figure 1.13: Butt coupled fibre to waveguide setup. Credit: [67]

Spot size converters (SSCs), such as inverse tapers and adiabatic mode transformers, are often integrated into the chip to gradually expand the on chip mode to better match the fibre's MFD. These converters are critical in achieving low loss, polarisation insensitive coupling [68, 69].

Key parameters influencing edge coupling include the waveguide geometry, taper profile, cladding material, and fibre type. Inverse taper structures gradually reduce the waveguide width to sub 100 nm scales, enabling the optical mode to expand into the surrounding cladding, thereby increasing the effective mode size.

Cladding engineering, often involving the use of low index polymers, plays a vital role in mode shaping and mechanical protection [27]. The coupling interface must also accommodate angular and lateral misalignments, prompting the use of v groove alignment and active alignment techniques during packaging. An example of using spot size convertors was displayed by Roelkens, et.al. by using a polymer waveguide taper structure with a SOI waveguide where losses induced by the tapering region was around 1dB.

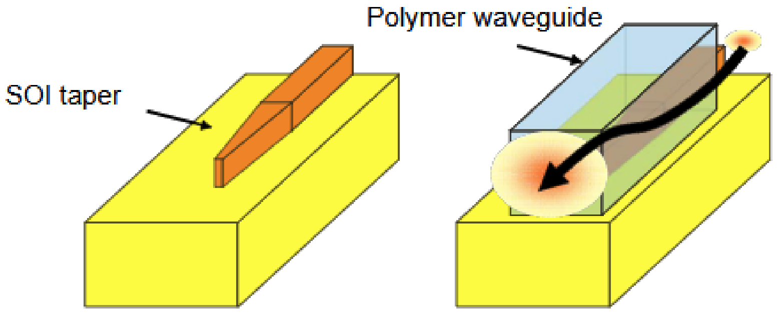

Figure 1.14: Polymer waveguide on SOI tapered waveguide for SSC. Credit: [27]

In addition to on-chip mode engineering, lensed fibres are frequently employed to relax alignment tolerances at the fibre–chip interface [70]. By tapering or shaping the fibre tip into a microlens, the emitted mode can be expanded or focused to better match the on-chip optical mode. This reduces sensitivity to lateral, vertical, and angular displacement, enabling more stable and manufacturable coupling. Lensed fibres are therefore particularly beneficial in high-density packaging or when edge coupling to waveguides with small effective mode sizes [71]. To illustrate the physics behind the lensed fibre, Fig. 1.15 shows the lensed region (blue), where the fibre tip is shaped into a small convex lens that focuses the light into a focal beam waist, improving coupling efficiency into the waveguide by allowing the working distance to be adjusted.

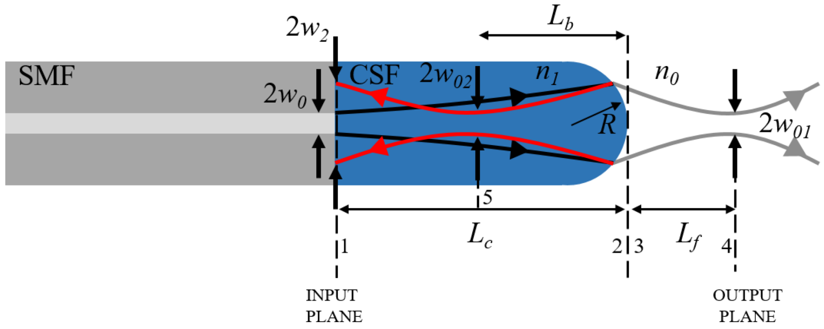

Figure 1.15: Working principle of lensed fibre to collimate output beam. Credit: [70]

Edge coupling techniques have demonstrated coupling losses as low as 0.1 dB per facet [72], with typical values ranging between 1–2 dB depending on the platform and alignment precision. The achievable bandwidth often exceeds 100 nm, with negligible polarisation dependence in well designed SSCs.

Experimental implementations have shown the robustness of edge coupling in high speed data transmission, quantum photonics, and sensing applications. Integration with fibre arrays enables high density, multi-channel optical interconnects, which are essential for scalable PIC systems [71, 73].

Despite its advantages, edge coupling faces challenges in terms of packaging complexity, sensitivity to alignment, and requirements for polished facets. Advances in passive alignment techniques, automated fibre attachment, and integration with photonic wire bonding are actively addressing these limitations.

Emerging trends include the use of 3D printed micro optics, such as mode adaptors and lens arrays, directly on the chip facet or fibre tip, as well as hybrid material integration to extend coupling performance across wider wavelength ranges and photonic platforms.

Future work is expected to focus on increasing fabrication tolerance, improving thermal stability, and scaling up to wafer-level packaging for volume manufacturing.

1.4.2 Grating Couplers

Bragg gratings are periodic perturbations in the refractive index of an optical waveguide, which cause constructive and destructive interference of propagating light at specific wavelengths [74, 75]. The Bragg condition shown,

$$\lambda_B = n_{\text{eff}}\Lambda, \tag{1.1}$$

where λ_B is the Bragg wavelength, n_{eff} is the effective refractive index, and Λ is the grating period, defines the central wavelength of reflection in a traditional in-plane waveguide configuration, where fig 1.16 illustrates an example schematic of fibre to chip coupling using grating couplers.

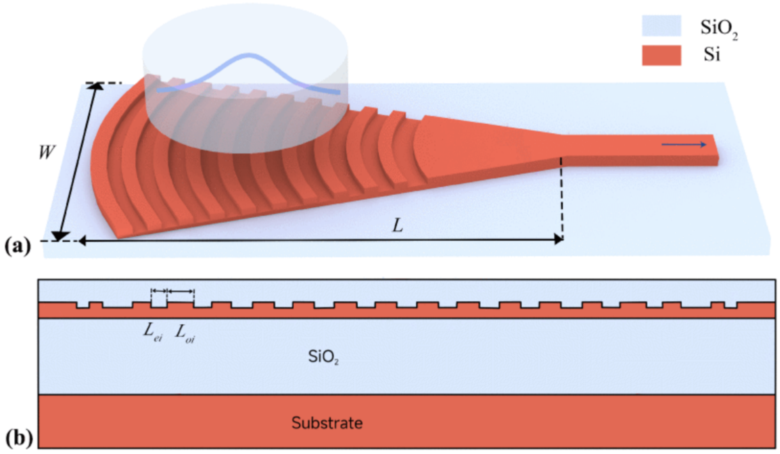

Figure 1.16: Fundamental schematic of SOI grating coupler. Credit: [76]

For fibre-to-chip coupling, a vertical Bragg condition must be considered, whereby the grating period is chosen such that the diffracted light exits at a defined angle relative to the chip surface. This condition arises from phase matching between the guided mode in the waveguide and the radiated mode in the cladding, and can be expressed as

$$\beta \pm k_{\mathrm{g}} = k_0 \sin\theta, \tag{1.2}$$

where $\beta = n_{\mathrm{eff}} k_0$ is the propagation constant of the guided mode, $k_{\mathrm{g}} = 2\pi/\Lambda$ is the reciprocal lattice vector of the grating, $k_0 = 2\pi/\lambda$ is the free-space wavenumber, and θ is the radiation angle relative to the chip normal. For vertical emission ($\theta = 0$), this simplifies to

$$\Lambda = \frac{m\lambda}{n_{\mathrm{eff}}}, \tag{1.3}$$

with diffraction order m. In most cases, the first diffraction order ($m = 1$) is employed to maximise coupling efficiency. More generally, when light is intentionally radiated at a slight angle—for example, to improve fibre alignment or to reduce back reflection—the Bragg condition takes the form

$$\Lambda = \frac{\lambda}{n_{\mathrm{eff}} - n_{\mathrm{clad}} \sin\theta}, \tag{1.4}$$

where n_{clad} is the refractive index of the cladding medium, typically close to unity for air.

In this case, the coupling process is governed not only by the grating resonance but also by mode matching between the fibre mode (typically Gaussian with a ~ 10 μm mode field diameter at 1550 nm) and the diffracted waveguide mode. This contrasts with conventional Bragg reflectors, where only longitudinal resonance is relevant, making vertical grating couplers a more complex design problem. To better illustrate the components of the bragg condition, fig. 1.17 illustrates the components with a schematic of a surface grating coupler.

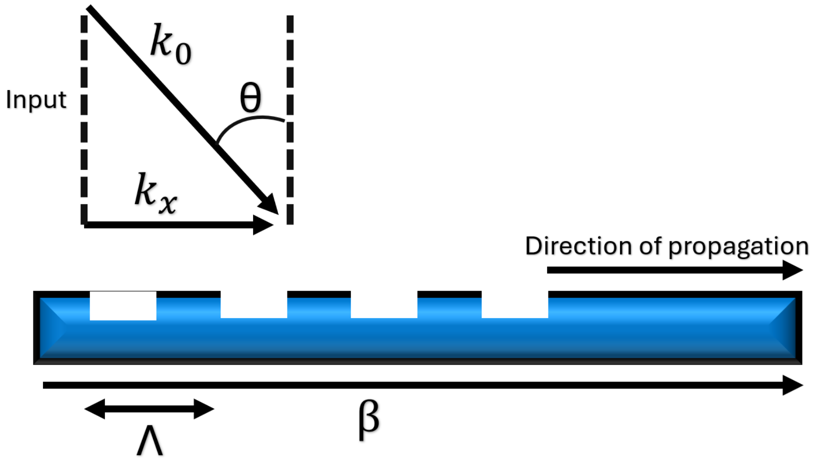

Figure 1.17: Operating principle of grating coupler.

Surface grating couplers are the most common realisation and are patterned directly onto the top surface of the waveguide layer, allowing vertical fibre coupling without polished facets. The fabrication of Bragg gratings for coupling applications typically involves electron beam lithography (EBL) or deep ultraviolet (DUV) lithography, followed by reactive ion etching (RIE). In high-index contrast platforms such as silicon-on-insulator (SOI), precise etch depth control is critical: small deviations can significantly alter coupling strength and directionality.

The performance of Bragg grating couplers depends on parameters such as grating period, duty cycle, etch depth, and apodisation profile. In practice, fibres are often placed at a small angle (8–10°) relative to the chip surface to suppress back reflection from second-order diffraction. As illustrated in fig. 1.18, state of the art grating couplers used for wavelengths around the 1550nm telecoms band use apodised grating profiles and metal back reflectors on a SOI platfroms to achieve peak coupling efficiencies of -0.58 dB, with a 3-dB bandwidth of 71 nm [77].

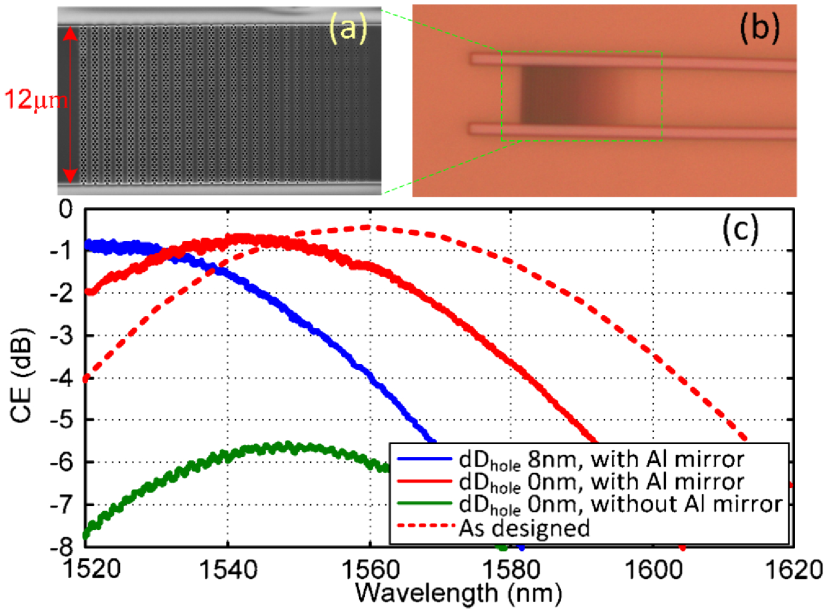

Figure 1.18: (a) Scanning electron microscopy (SEM) and (b) optical microscopy images of the fabricated grating coupler. (c) Measured CE for the fabricated coupler with Al mirror with and without 8 nm hole size change as well as for the same grating coupler fabricated on the same type of SOI wafer without Al mirror. Credit: [77]

Furthermore, gratings have been developed for visible photonic circuit applications, using the SiN platform. Shown in fig. 1.19 is fabricated SiN grating couplers for wavelengths 638 nm and 532 nm, achieving 8 dB reduced back reflections and coupling losses of 0.8 dB

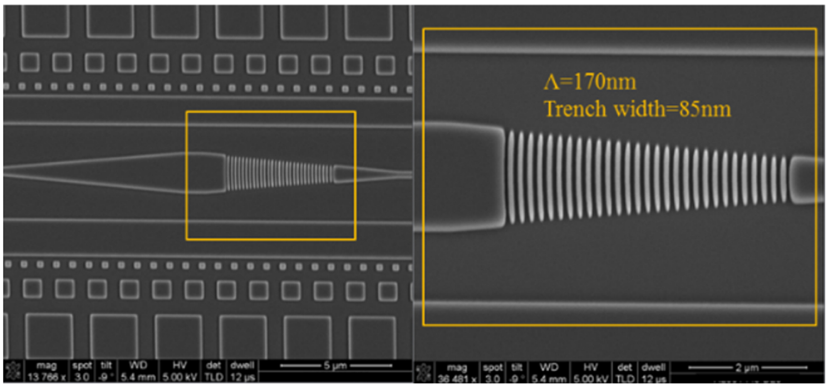

Figure 1.19: SEM image of SiN grating coupler for visible wavelengths. Credit: [78]

When discussing the drawbacks of using grating couplers, it is important to consider their limited operational bandwidth. As shown in Fig. 1.20, the coupling efficiency for both uniform and apodised gratings falls off by several dB over a wavelength range of approximately 40 nm on either side of the peak coupling wavelength. [79].

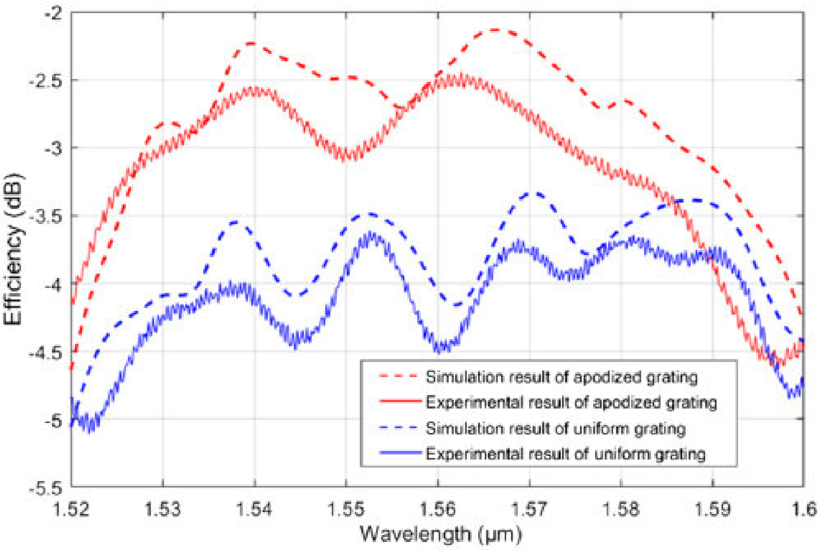

Figure 1.20: Experimental and theoretical comparison of loss and bandwidth for grating couplers. Credit: [79]

Bragg grating couplers have been demonstrated across a range of applications, from high-density data communications and telecom interconnects to sensing and emerging quantum photonics. Their ability to enable wafer-scale optical testing, combined with the versatility of asymmetric and inverse designs, continues to make them a cornerstone in the development of practical and scalable photonic integrated circuits.

1.4.3 Waveguide to vertical turning mirror couplers

Two-photon polymerisation (2PP) is an advanced additive manufacturing technique that enables the direct fabrication of three-dimensional micro- and nano-structures with sub-micron resolution [80, 81]. Unlike conventional lithography, which is typically limited to planar geometries, 2PP exploits the non-linear absorption of femtosecond laser pulses in a photosensitive resin to achieve true 3D patterning. Polymerisation occurs only within the focal volume where two photons are absorbed simultaneously, confining the chemical reaction to a voxel (volumetric pixel) that can be scanned in three dimensions. An illustration in fig. 1.21, depicts the 2PP process, where the focal point region undergoes the pricess, leaving the surrounding region uncured. By precisely controlling the laser focus through a computer-aided design (CAD) file, complex freeform geometries can be written directly into the resist with high fidelity.

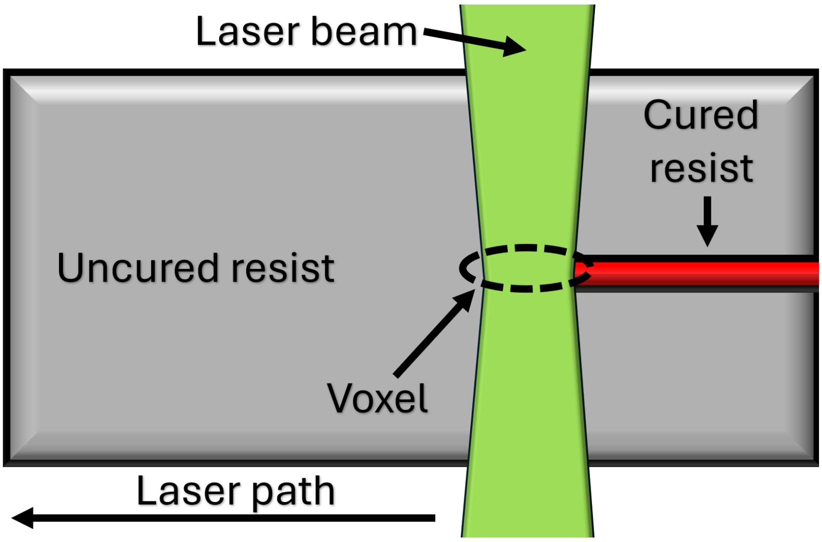

Figure 1.21: Schematic of 2PP.

With the ability to fabricate 3D structures, researchers have taking full advantage of this technology to develop novel coupling techniques for PICs. For example, turning mirrors for vertical chip to fibre systems have been developed by S. Yu, et.al. [82]. Unlike grating couplers, which are narrowband, or edge couplers, which require chip facet access, the reflective 2PP structures exploit total internal reflection to achieve low-loss and broadband operation. The fabricated devices consist of SiN trenches were the polymer material is defined at the end facet of a SiN waveguide fig. 1.22a.

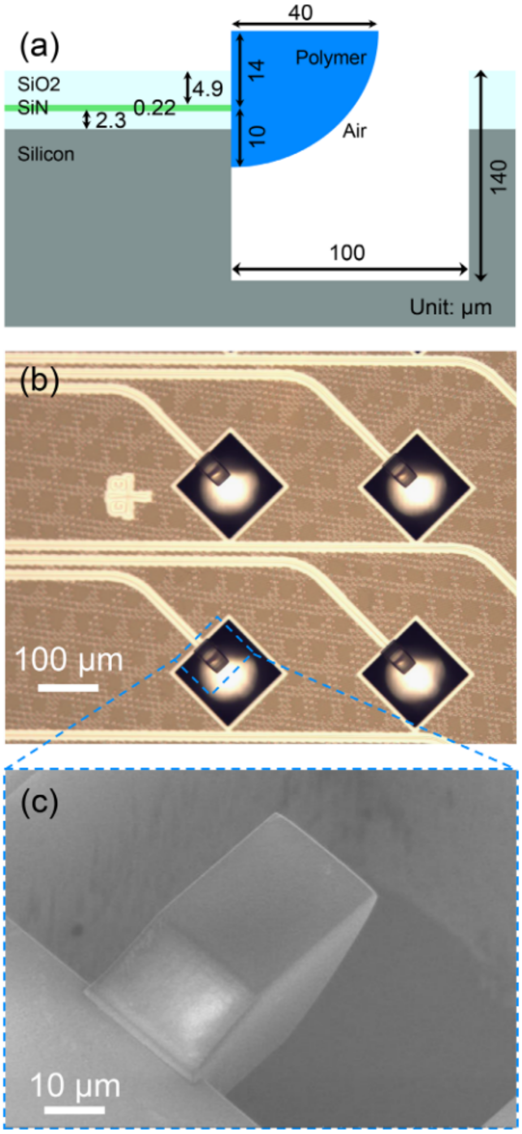

Figure 1.22: (a) Schematic cross-section of the 2PP mirror b) Top view optical image of processed chip. c) Close-up view of the coupler structure. Credit: [82].

The couplers achieve an experimentally measured insertion loss as low as 0.5 dB at 1550 nm, representing the lowest reported value for surface-normal coupling. Moreover, they exhibit a record 1-dB bandwidth of 300 nm (1340–1640 nm) and maintain <2 dB

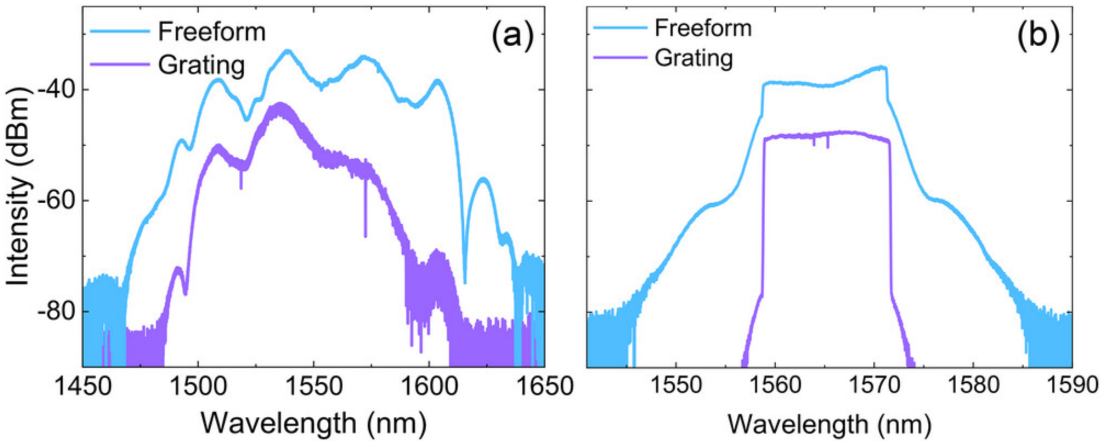

Figure 1.23: Free-form micro-optical couplers (blue curves) and grating couplers (purple curves) losses. Credit: [82]

loss across the full O- to U-band telecom window. Fig 1.23 shows the experimental loss of the system with a on-graph comparison to grating coupler losses.

These results establish 2PP-fabricated free-form reflectors as a promising packaging solution for ultra-broadband, low-loss, and scalable optical interfacing, with clear advantages over conventional grating and edge coupling in integrated photonics. However, post processing on foundry SiN can play a major role in the lack of scalability due to the foundry production costs.

Another group using 2PP for free-form micro-optic couplers was demonstrated by P. Dietrich et al. While free-form turning mirrors had previously been shown, their work extended the concept by fabricating a broader range of 2PP coupling devices, including facet-attached lenses and beam expanders. The printed lenses enabled efficient coupling between edge-emitting lasers and single-mode fibres, reaching losses as low as 0.6 dB, which approaches the theoretical optimum (Fig. 1.24).

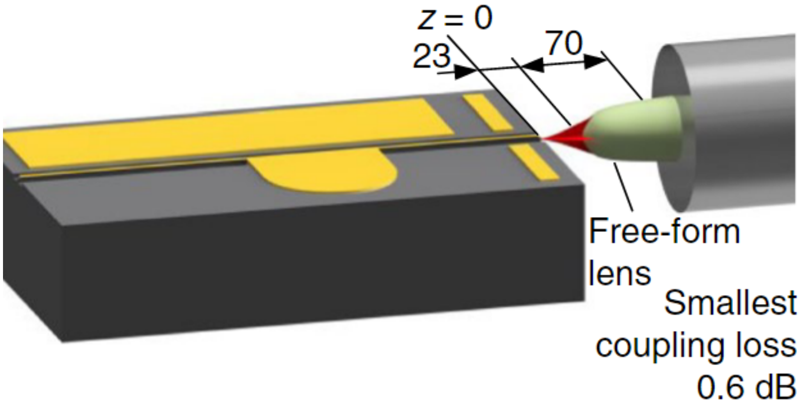

Figure 1.24: Free form lens printed on fibre (right) to produce 0.6dB coupling losses with InP laser (left). Credit: [83]

Similarly, free-form total internal reflection (TIR) mirrors were used to both redirect and shape beams, yielding 0.6 dB losses in fibre-to-fibre links and 1.1 dB in VCSEL-to-fibre coupling (Fig. 1.25). These results significantly outperform conventional microlens or lensed-fibre approaches, which typically exhibit several dB higher losses.

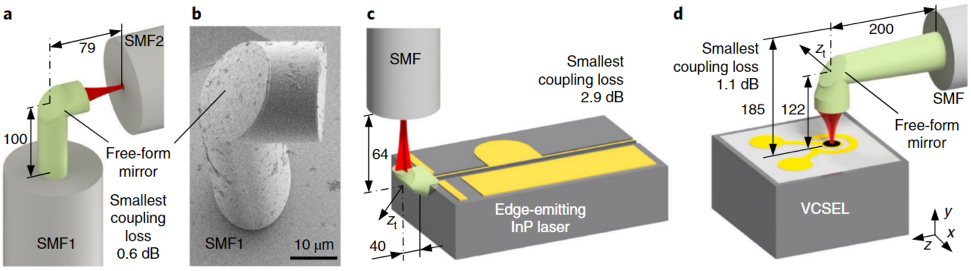

Figure 1.25: (a) fibre–fibre coupling with 0.6 dB loss, (b) SEM image of printed mirror, (c) laser–fibre coupling with 2.9 dB loss, (d) VCSEL–fibre coupling with reduced assembly height <200 µm. Credit: [83].

Beyond these, Dietrich et al. demonstrated beam expanders that relaxed alignment tolerances to ±5 µm laterally, while still maintaining sub-1 dB coupling loss (Fig. 1.26). This level of tolerance is sufficient to enable cost-effective passive alignment, a key step toward scalable packaging.

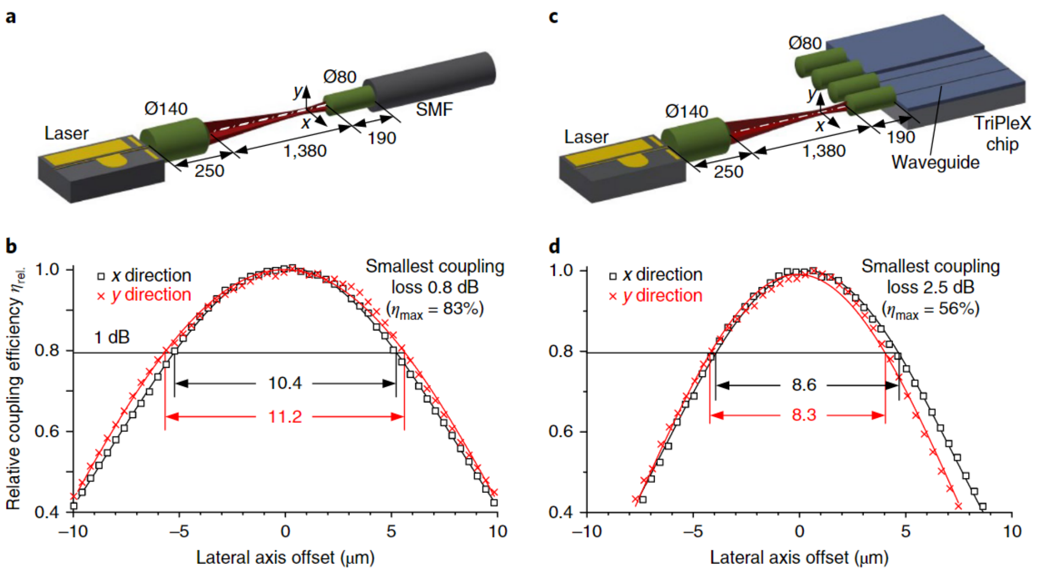

Figure 1.26: Coupling with beam expanders: (a) laser–SMF setup, (b) 0.8 dB loss with ±5 μm tolerance, (c) laser–TriPleX setup, (d) 2.5 dB loss with ±4 μm tolerance, enabling passive alignment. Credit: [83].

Furthermore different fabrication methods have been explored to realise such coupling schemes. In silicon photonics, anisotropic etching along the 111 planes naturally produces facets at 54.7°, which act as efficient mirrors for redirecting guided modes (Fig. 1.27).

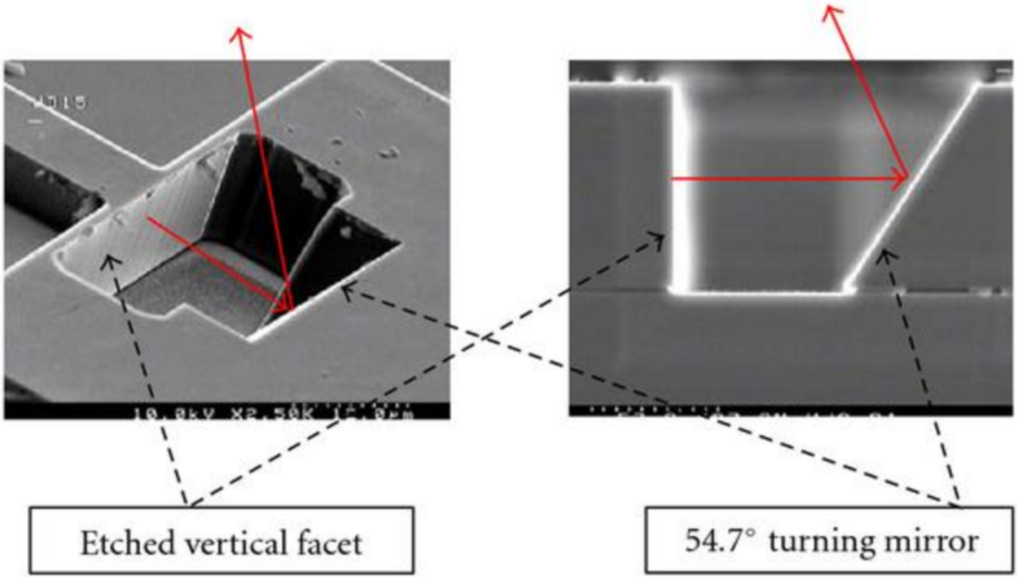

Figure 1.27: SEM of waveguide facet (LHS) and turning mirror (RHS). Credit: [84].

Light emerging from a ridge waveguide can traverse a small air gap before being reflected vertically towards a detector or fibre [84]. Other approaches include mechanically cutting 45° grooves through or adjacent to the guiding region using a dicing saw (Fig. 1.28).

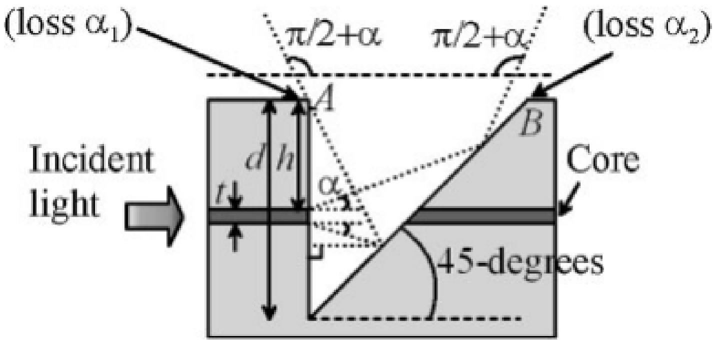

Figure 1.28: Model of beam propagation inside groove and definition of loss due to shadowing by corners of groove. Credit: [85].

After groove formation, the structure is planarised and low-index materials can be used to suppress excess reflection. Devices fabricated in this way have achieved insertion losses as low as 1.3 dB compared to straight waveguides, and related designs have also been demonstrated as optical taps with only 0.5 dB excess loss, as indicated in the measurements under optimum conditions shown in fig. 1.29 [85].

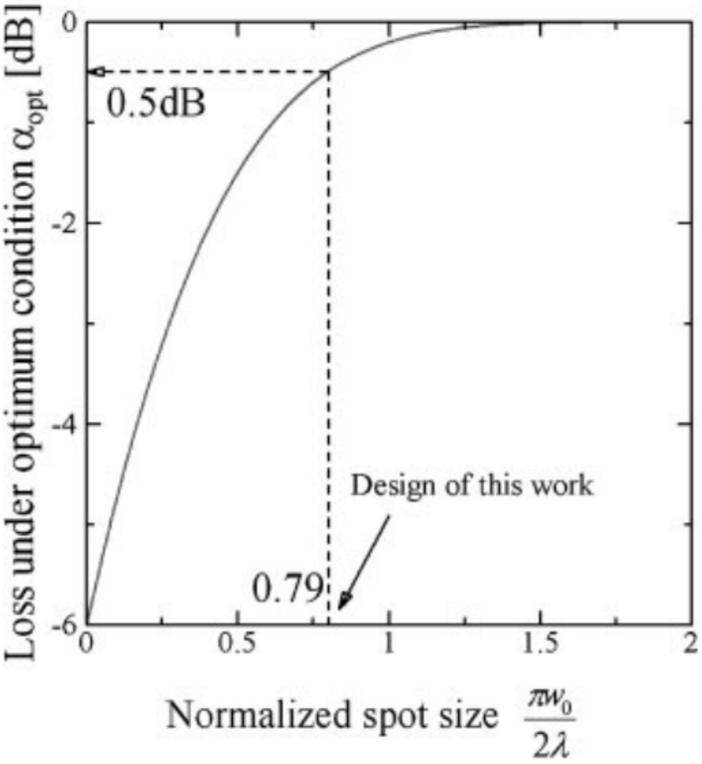

Figure 1.29: Loss under optimum condition of h vs normalized spot size. Credit: [85]

Despite these encouraging results, drawbacks remain inherent to the air-gap geometry. The discontinuity at the waveguide–air interface leads to beam divergence within the gap, which reduces coupling efficiency. In addition, back reflections at the air–material boundaries can couple into the guided mode, degrading overall performance. Mitigation typically requires careful optimisation of groove geometry, spot-size design, and facet orientation.

Emerging approaches to turning mirror technology, including advanced fabrication methods, hybrid integration, and 3D design innovations, collectively address the critical limitations of conventional designs. By combining advances in materials science, microfabrication, automation, and additive manufacturing, these developments provide a robust pathway toward scalable, high performance photonic integration in next generation systems.

1.5 Summary

In summary, this chapter has discussed the growing need for photonic integrated circuits (PICs) as global data consumption increases and the physical limits of electronic transistors are approached. PICs provide a chip scale photonic platform with dense and scalable components such as waveguides, resonators, and coupling devices. Demonstrated material platforms include silicon on insulator (SOI), silicon nitride (SiN), and photosensitive polymers. SOI supports highly compact photonic systems with strong mode confinement and tight bend radii, but it suffers from absorption at visible wavelengths. SiN and polymers are more suitable in this spectral range because of their wide optical transparency and compatibility with CMOS fabrication. SiN often delivers the best optical performance, for example ultra low propagation losses, but it is more expensive and has longer fabrication times. In contrast, polymers such as SU-8 offer low cost and rapid prototyping, making them attractive for fast device development.

An essential challenge for all platforms is coupling light on and off the photonic chip. Several techniques have been developed, each with advantages and drawbacks. Edge coupling is widely used, where optical fibres are butt coupled to waveguides. This approach faces large mode mismatch and strict alignment requirements, which has led to research on methods to improve coupling efficiency. Spot size converters (SSCs) reduce large fibre mode diameters using tapered waveguides embedded in larger polymer structures, which improves efficiency but still leaves significant losses and tight alignment tolerances.

Grating couplers provide another option, coupling light vertically through periodic structures. They can achieve high efficiency but operate only over narrow spectral ranges of tens of nanometres, and they require sub wavelength fabrication precision.

More recently, polymers have enabled coupling devices fabricated by two photon polymerisation (2PP). This method produces free form optics such as turning mirrors, beam expanders, and microlenses on fibre facets. These elements typically provide working bandwidths spanning several hundred nanometres around the central wavelength. However, challenges remain with repeatability, scalability, and integration onto foundry fabricated devices, where post processing carries significant risk.

The following chapters present the design and characterisation of a chip to fibre coupling device for PICs that aims to achieve ultra broadband operation with high coupling efficiency, extending from the visible spectrum into the infrared.

Bibliography

[1] Cisco Systems. Cisco annual internet report (2018–2023). *White Paper*, 2020.

[2] David A. B. Miller. Device requirements for optical interconnects to silicon chips. *Proceedings of the IEEE*, 97(7):1166–1185, 2009.

[3] Gordon E. Moore. Cramming more components onto integrated circuits. *Electronics*, 38(8):114–117, 1965.

[4] Robert H. Dennard, Frank H. Gaensslen, Hwa-Nien Yu, V. Leo Rideout, Ernest Bassous, and Andre R. LeBlanc. Design of ion-implanted mosfets with very small physical dimensions. *IEEE Journal of Solid-State Circuits*, 9(5):256–268, 1974.

[5] Wikimedia Commons. File:moore's law transistor count 1970-2020.png — wikimedia commons, the free media repository, 2025. [Online; accessed 30-September-2025].

[6] Laurent Vivien and Lorenzo Pavesi. *Handbook of Silicon Photonics*. CRC Press, 2013.

[7] Graham T. Reed and Andrew P. Knights. *Silicon Photonics: An Introduction*. John Wiley & Sons, 2004.

[8] Wenchao Tian, Huahua Hou, Haojie Dang, Xinxin Cao, Dexin Li, Si Chen, and Bingxu Ma. Progress in research on co-packaged optics. *Micromachines*, 15(10):1211, 2024.

[9] David J. Thomson, Andrew Zilkie, John E. Bowers, Tin Komljenovic, Graham T. Reed, Laurent Vivien, Delphine Marris-Morini, Eric Cassan, Laurent Virot, Jean-

Marc Fédéli, Jean-Michel Hartmann, Jens H. Schmid, Dan-Xia Xu, Frédéric Boeuf, Peter O'Brien, Goran Z. Mashanovich, and Milos Nedeljkovic. Roadmap on silicon photonics. *Journal of Optics*, 18(7):073003, 2016.

[10] J. Leuthold, C. Koos, and W. Freude. Nonlinear silicon photonics. *Nature Photonics*, 4:535–544, 2010.

[11] Jeremy L. O'Brien. Optical quantum computing. *Science*, 318(5856):1567–1570, 2007.

[12] Martin D. Baaske, Matthew R. Foreman, and Frank Vollmer. Single-molecule nucleic acid interactions monitored on a label-free microcavity biosensor platform. *Nature Nanotechnology*, 9:933–939, 2014.

[13] Xiao-Yun Xu and Xian-Min Jin. Integrated photonic computing beyond the von neumann architecture. *ACS Photonics*, 10(4):1027–1036, 2023.

[14] Lukas Chrostowski and Michael Hochberg. *Silicon Photonics Design: From Devices to Systems*. Cambridge University Press, 2015.

[15] Po Dong, Eric Lively, Hong Liang, Nan Feng, David Li, Hong Chen, Lars L. Buhl, Andy Nolting, Gerald E. Hoefler, Barry R. Koch, Ashok V. Krishnamoorthy, and Mehrdad Asghari. Low power and compact reconfigurable multiplexing devices based on silicon microring resonators. *Optics Express*, 18(10):9852–9858, 2010.

[16] Hermann A. Haus. *Waves and Fields in Optoelectronics*. Prentice Hall, 1984.

[17] Yusheng Qian, Seunghyun Kim, Jiguo Song, Gregory P. Nordin, and Jianhua Jiang. Compact and low loss silicon-on-insulator rib waveguide 90° bend. *Opt. Express*, 14(13):6020–6028, 2006.

[18] Pavel Cheben, Robert Halir, Jens H. Schmid, Harry A. Atwater, and David R. Smith. Subwavelength integrated photonics. *Nature*, 560:565–572, 2018.

[19] Richard Soref. The past, present, and future of silicon photonics. *IEEE Journal of Selected Topics in Quantum Electronics*, 12(6):1678–1687, 2006.

[20] Xiangfei Chen, Chen Li, Xian Zhang, Daoxin Dai, and Sailing He. The emergence of silicon photonics as a flexible technology platform. *Proceedings of the IEEE*, 106(12):2101–2116, 2018.

[21] Di Liang and John E. Bowers. Recent progress in lasers on silicon. *Nature Photonics*, 4:511–517, 2010.

[22] Helmut Ermert. Guiding and radiation characteristics of planar waveguides. *IEE Journal on Microwaves, Optics and Acoustics*, 3:59–62, 1979.

[23] M. E. Lines. The search for very low loss fiber-optic materials. *Science*, 226(4675):663–668, 1984.

[24] R. Nagarajan, C.H. Joyner, R.P. Schneider, J.S. Bostak, T. Butrie, A.G. Dentai, V.G. Dominic, P.W. Evans, M. Kato, M. Kauffman, D.J.H. Lambert, S.K. Mathis, A. Mathur, R.H. Miles, M.L. Mitchell, M.J. Missey, S. Murthy, A.C. Nilsson, F.H. Peters, S.C. Pennypacker, J.L. Pleumeekers, R.A. Salvatore, R.K. Schlenker, R.B. Taylor, Huan-Shang Tsai, M.F. Van Leeuwen, J. Webjorn, M. Ziari, D. Perkins, J. Singh, S.G. Grubb, M.S. Reffle, D.G. Mehuys, F.A. Kish, and D.F. Welch. Large-scale photonic integrated circuits. *IEEE Journal of Selected Topics in Quantum Electronics*, 11(1):50–65, 2005.

[25] Francisco M. Soares, Moritz Baier, Tom Gaertner, Norbert Grote, Martin Moehrle, Tobias Beckerwerth, Patrick Runge, and Martin Schell. Inp-based foundry pics for optical interconnects. *Applied Sciences*, 9(8):1588, 2019.

[26] Martijn J. R. Heck, Jared F. Bauters, Michael L. Davenport, Daryl T. Spencer, and John E. Bowers. Ultra-low loss waveguide platform and its integration with silicon photonics. *Laser & Photonics Reviews*, 8(5):667–686, 2014.

[27] Gunther Roelkens, Pieter Dumon, Wim Bogaerts, Dries Van Thourhout, and Roel Baets. Efficient silicon-on-insulator fiber coupler fabricated using 248-nm-deep UV lithography. *IEEE Photonics Technology Letters*, 17:2613–2615, 2006.

[28] Jeremy Witzens. High-speed silicon photonics modulators. *Proceedings of the IEEE*, 106(12):2158–2182, 2018.

[29] Tao Li, Jie Hou, Jinli Yan, Rulin Liu, Hui Yang, and Zhigang Sun. Chiplet heterogeneous integration technology–status and challenges. *Electronics*, 9(4):670, 2020.

[30] Tin Komljenovic, Duanni Huang, Paolo Pintus, Minh A. Tran, Michael L. Davenport, and John E. Bowers. Photonic integrated circuits using heterogeneous integration on silicon. *Proceedings of the IEEE*, 106(12):2246–2257, 2018.

[31] Mikhail Churaev, Rui Ning Wang, Annina Riedhauser, Viacheslav Snigirev, Terence Blésin, Charles Möhl, Miles H. Anderson, Anat Siddharth, Youri Popoff, Ute Drechsler, Daniele Caimi, Simon Hönl, Johann Riemensberger, Junqiu Liu, Paul Seidler, and Tobias J. Kippenberg. A heterogeneously integrated lithium niobate-on-silicon nitride photonic platform. *Nature Communications*, 14:39047, 2023.

[32] Jack A. Smith, Paul Hill, Charalambos Klitis, Lukas Weituschat, Pablo A. Postigo, Marc Sorel, Martin D. Dawson, and Michael J. Strain. High precision integrated photonic thermometry enabled by a transfer printed diamond resonator on gan waveguide chip. *Opt. Express*, 29(18):29095–29106, 2021.

[33] K. Okamoto. Progress and technical challenge for planar waveguide devices: silica and silicon waveguides. *Laser & Photonics Reviews*, 6(1):14–23, 2012.

[34] Richard Soref. The past, present, and future of silicon photonics. *IEEE Journal of Selected Topics in Quantum Electronics*, 12(6):1678–1687, 2006.

[35] Bahram Jalali and Sasan Fathpour. Silicon photonics. *Journal of Lightwave Technology*, 24(12):4600–4615, 2006.

[36] Yikai Su, Yong Zhang, Ciyuan Qiu, Xuhan Guo, and Lu Sun. Silicon photonic platform for passive waveguide devices: Materials, fabrication, and applications. *Advanced Materials Technologies*, 5(8):1901153, 2020.

[37] G. Z. Mashanovich, G. T. Reed, B. D. Timotijevic, and S. P. Chan. *Silicon Photonic Waveguides*, chapter 2, pages 15–46. John Wiley Sons, Ltd, 2008.

[38] Bowei Dong, Xin Guo, Chong Ho, Bo Li, Hong Wang, Chengkuo Lee, Xianshu Luo, and Patrick Lo. Silicon-on-Insulator waveguide devices for broadband mid-infrared photonics. *IEEE Photonics Journal*, 9:2692039, 2017.

[39] Wim Bogaerts, Roel Baets, Pieter Dumon, Vincent Wiaux, S. Beckx, Dirk Taillaert, Bert Luyssaert, Joris Van Campenhout, Peter Bienstman, and Dries Van Thourhout. Nanophotonic waveguides in silicon-on-Insulator fabricated with CMOS technology. *Journal of Lightwave Technology*, 23:401–412, 2005.

[40] G. T. Reed, G. Mashanovich, F. Y. Gardes, and D. J. Thomson. Silicon optical modulators. *Nature Photonics*, 4(8):518–526, 2010.

[41] K. Luke, A. Dutt, C. B. Poitras, and M. Lipson. Overcoming sin film stress limitations for high quality factor ring resonators. *Optics Express*, 21(19):22829–22833, 2013.

[42] J. Puckett, M. Bajcsy, and A. et al. Ryou. Silicon nitride photonics for low-loss and high-q integrated devices. *Optics Express*, 23(1):113–123, 2015.

[43] X. Ji, M. Yan, and R. et al. Luo. Ultra-low-loss silicon nitride waveguides with high-aspect-ratio cross-sections. *Optica*, 4(6):665–670, 2017.

[44] J. S. Levy, M. A. Foster, A. L. Gaeta, and M. Lipson. Cmos-compatible multiple-wavelength oscillator for on-chip optical communications. *Nature Photonics*, 4(1):37–40, 2010.

[45] J. Leuthold, C. Koos, and W. Freude. Nonlinear silicon photonics. *Nature Photonics*, 4(8):535–544, 2010.

[46] J. F. Bauters, M. J. R. Heck, and D. et al. John. Ultra-low-loss high-aspect-ratio sin waveguides. *Optics Express*, 19(4):3163–3174, 2011.

[47] Shota Ishimura, Abdulaziz E. Elfiqi, Takashi Kan, Hidenori Takahashi, and Takehiro Tsuritani. Silicon-nitride photonic integrated waveguide for dual-polarization traveling-wave four-wave-mixing applications. *Optics Express*, 33(9):19546–19557, 2025.

[48] Mateus Corato-Zanarella, Xingchen Ji, Aseema Mohanty, and Michal Lipson. Absorption and scattering limits of silicon nitride integrated photonics in the visible spectrum. *Opt. Express*, 32(4):5718–5728, 2024.

[49] Yi Xuan, Yang Liu, Leo T. Varghese, Andrew J. Metcalf, Xiaoxiao Xue, Pei-Hsun Wang, Kyunghun Han, Jose A. Jaramillo-Villegas, Abdullah Al Noman, Cong Wang, Sangsik Kim, Min Teng, Yun Jo Lee, Ben Niu, Li Fan, Jian Wang, Daniel E. Leaird, Andrew M. Weiner, and Minghao Qi. High-q silicon nitride microresonators exhibiting low-power frequency comb initiation. *Optica*, 3(11):1171–1180, 2016.

[50] Y. Okawachi, J. S. Levy, M. Lipson, and A. L. Gaeta. Octave-spanning frequency comb generation in a silicon nitride chip. *Optics Letters*, 36(17):3398–3400, 2011.

[51] LIGENTECH. https://www.lionix-international.com/, 2025. [Online; accessed 30-September-2025].

[52] LioniX. https://www.ligentec.com/, 2025. [Online; accessed 30-September-2025].

[53] Cornerstone. https://cornerstone.sotonfab.co.uk/, 2025. [Online; accessed 30-September-2025].

[54] Roger Dangel, Christoph Berger, RenÉ Beyeler, Laurent Dellmann, Max Gmur, RÉgis Hamelin, Folkert Horst, Tobias Lamprecht, Thomas Morf, Stefano Oggioni, Mauro Spreafico, and Bert Jan Offrein. Polymer-waveguide-based board-level optical interconnect technology for datacom applications. *IEEE Transactions on Advanced Packaging*, 31(4):759–767, 2008.

[55] H. Ma, A.K.-Y. Jen, and L.R. Dalton. Polymer-based optical waveguides: Materials, processing, and devices. *Advanced Materials*, 14(19):1339–1365, 2002.

[56] Patrick Abgrall, Veronique Conedera, Henri Camon, Anne-Marie Gue, and Nam-Trung Nguyen. Su-8 as a structural material for labs-on-chips and microelectromechanical systems. *Electrophoresis*, 28(24):4539–4551, 2007.

[57] Maria Nordström, Dan A. Zauner, Anja Boisen, and Jörg Hübner. Monolithic single-mode su-8 waveguides for integrated optics. In *Proceedings of SPIE: Mi-*

crofluidics, BioMEMS, and Medical Microsystems IV, volume 6112, page 611206, 2006.

[58] Maria Nordström, Dan A. Zauner, Anja Boisen, and Jörg Hübner. Single-mode waveguides with su-8 polymer core and cladding for moems applications. *J. Lightwave Technol.*, 25(5):1284–1289, 2007.

[59] Jhonattan C. Ramirez, Juliana N. Schianti, Maria G. Almeida, Aristides Pavani, Roberto R. Panepucci, Hugo E. Hernandez-Figueroa, and Lucas H. Gabrielli. Low-loss modified su-8 waveguides by direct laser writing at 405 nm. *Opt. Mater. Express*, 7(7):2651–2659, 2017.

[60] Hanan H. Hamid, Thomas Fickenscher, and David V. Thiel. Experimental assessment of su-8 optical waveguides buried in plastic substrate for optical interconnections. *Appl. Opt.*, 54(22):6623–6631, 2015.

[61] A. Piruska, Ali Asgar Bhagat, Kaijian Zhou, E. T. K. Peterson, Ian Papautsky, and C. Seliskar. Characterization of SU-8 optical multimode waveguides for integrated optics and sensing on microchip devices. In *Microfluidics, BioMEMS, and Medical Microsystems IV*, volume 6112, page 611206. SPIE, 2006.

[62] Seiji Sowa, Wataru Watanabe, Takayuki Tamaki, Junji Nishii, and Kazuyoshi Itoh. Symmetric waveguides in poly(methyl methacrylate) fabricated by femtosecond laser pulses. *Opt. Express*, 14(1):291–297, 2006.

[63] Jay W. Reddy, Maya Lassiter, and Maysamreza Chamanzar. Parylene photonics: a flexible, broadband optical waveguide platform with integrated micromirrors for biointerfaces. *Microsystems & Nanoengineering*, 6:12, 2020.

[64] Anne Rasmusson and Electra Gizeli. Comparison of poly(methyl methacrylate) and novolak waveguide coatings for an acoustic biosensor. *Journal of Applied Physics*, 90(12):5911–5914, 2001.

[65] M. Ferriol, A. Gentilhomme, M. Cochez, N. Oget, and J.L. Mieloszynski. Thermal degradation of poly(methyl methacrylate) (pmma): modelling of dtg and tg curves. *Polymer Degradation and Stability*, 79(2):271–281, 2003.

[66] O. I. Szentesi and E. A. Noga. Parylene c films for optical waveguides. *Appl. Opt.*, 13(11):2458–2459, 1974.

[67] Tiecheng Zhu, Yiwen Hu, Pradip Gatkine, Sylvain Veilleux, Joss Bland-Hawthorn, and Mario Dagenais. Ultrabroadband high coupling efficiency fiber-to-waveguide coupler using Si_3N_4/SiO_2 waveguides on silicon. *IEEE Photonics Journal*, 8:1–12, 2016.

[68] Yaxiao Lai, Yu Yu, Songnian Fu, Jing Xu, Perry Ping Shum, and Xinliang Zhang. Efficient spot size converter for higher-order mode fiber-chip coupling. *Opt. Lett.*, 42(18):3702–3705, 2017.

[69] Yan Zhang, Siyang Liu, Wenhao Zhai, Chao Peng, Zhewei Wang, Junbo Feng, and Jin Guo. Reconfigurable spot size converter for the silicon photonics integrated circuit. *Opt. Express*, 29(23):37703–37711, 2021.

[70] Soongho Park, Sunghwan Rim, Ju Wan Kim, Jinho Park, Ik-Bu Sohn, and Byeong Ha Lee. Analysis of design and fabrication parameters for lensed optical fibers as pertinent probes for sensing and imaging. *Sensors*, 18(12):4150, 2018.

[71] J.H.C. Van Zantvoort, S.G.L. Plukker, E.C.A. Dekkers, G.D. Petkov, G.D. Khoe, A.M.J. Koonen, and H. Waardt. Lensed fiber-array assembly with individual fiber fine positioning in the submicrometer range. *IEEE Journal of Selected Topics in Quantum Electronics*, 12(5):931–939, 2006.

[72] W. Emkey and C. Jack. Analysis and evaluation of graded-index fiber lenses. *Journal of Lightwave Technology*, 5(9):1156–1164, 1987.

[73] L. Liao, A. Liu, D. Rubin, J. Basak, Y. Chetrit, H. Nguyen, R. Cohen, N. Izhaky, and M. Paniccia. 40gbit/s silicon optical modulator for high-speed applications. *Electronics Letters*, 43:1196–1197, 2007.

[74] A. Yariv. *Optical Electronics in Modern Communications.* Number v. 1 in Oxford series in electrical and computer engineering. Oxford University Press, 1997.

[75] T. Erdogan. Fiber grating spectra. *Journal of Lightwave Technology*, 15(8):1277–1294, 1997.

[76] Guangbiao Zhong, Haoda Xu, Ruitao Zhang, Zhe Kang, Yegang Lu, Huihong Zhang, and Ye Tian. Inverse design of efficient perfectly vertical grating couplers on 220-nm soi platform based on adjoint optimization. *IEEE Journal of Quantum Electronics*, 61(6):1–5, 2025.

[77] Yunhong Ding, Christophe Peucheret, Haiyan Ou, and Kresten Yvind. Fully etched apodized grating coupler on the SOI platform with 0.58 dB coupling efficiency. *Optics Letters*, 39(18):5348–5350, 2014.

[78] Jeong Hwan Song, Tangla D. Kongnyuy, Benedetto Troia, Sandeep Seema Saseendran, Philippe Soussan, Roelof Jansen, and Xavier Rottenberg. Grating devices on a silicon nitride technology platform for visible light applications. *OSA Continuum*, 2(4):1155–1165, 2019.

[79] Pengfei Xu, Yanfeng Zhang, Zengkai Shao, Lin Liu, Lidan Zhou, Chunchuan Yang, Yujie Chen, and Siyuan Yu. High-efficiency wideband SiNx-on-SOI grating coupler with low fabrication complexity. *Optics Letters*, 42:3391–3394, 2017.

[80] Shoji Maruo, Osamu Nakamura, and Satoshi Kawata. Three-dimensional microfabrication with two-photon-absorbed photopolymerization. *Opt. Lett.*, 22(2):132–134, 1997.

[81] Xiaoqin Zhou, Yihong Hou, and Jieqiong Lin. A review on the processing accuracy of two-photon polymerization. *AIP Advances*, 5(3):030701, 2015.

[82] Shaoliang Yu, Luigi Ranno, Qingyang Du, Samuel Serna, Colin McDonough, Nicholas Fahrenkopf, Tian Gu, and Juejun Hu. Free-form micro-optics enabling ultra-broadband low-loss off-chip coupling. *Laser and Photonics Reviews*, 17(6):e202200025, 2023.

[83] P. I. Dietrich, M. Blaicher, I. Reuter, M. Billah, T. Hoose, A. Hofmann, C. Caer, R. Dangel, B. Offrein, U. Troppenz, M. Moehrle, W. Freude, and C. Koos. In situ 3D nanoprinting of free-form coupling elements for hybrid photonic integration. *Nature Photonics*, 12:241–247, 2018.

[84] B. Luff, Dazeng Feng, Daniel Lee, Wei Qian, Hong Liang, and Mehdi Asghari. Hybrid silicon photonics for low-cost high-bandwidth link applications. *Advances in Optical Technologies*, 2008:245131, 2008.

[85] Yasutomo Johraku and Yasuo Kokubun. Low loss vertical optical path conversion using 45° mirror for coupling between optical waveguide devices and planar devices. *Japanese Journal of Applied Physics*, 47(8S1):6744, 2008.

Chapter 2

Design and Fabrication of Broadband Vertical Waveguide Mirror Couplers

2.1 Introduction

Off-chip coupling to free-space and fibre is a fundamental requirement for photonic integrated circuits (PICs), with the trade-off between operating bandwidth and insertion loss representing a critical design concern. High losses in coupling schemes, particularly for output coupling, are especially detrimental, as excessive loss can result in information generated on chip being irretrievably lost. Furthermore, a standardised coupling structure capable of supporting the hybrid integration of active optical sources is required to enable scalable and flexible system architectures. The work presented in this thesis is primarily motivated by applications in short-reach optical interconnects and chip-level light emission, where compact, alignment-tolerant interfaces between photonic circuits and incoherent or weakly coherent sources are essential. In this context, a 5 x 10 vertical mirror geometry is chosen to support multimode operation within an SU-8 waveguide platform, providing relaxed fabrication tolerances and efficient coupling to extended emission sources such as light-emitting diodes (LEDs). Such an approach prioritises broadband performance and robustness over single-mode operation, aligning with the requirements of low-cost, hybrid-integrated photonic systems. Therefore, we present a rapid-prototyping, commercially available photoresist-based vertical coupling device that offers broadband spectral capability and low insertion loss.

2.2 Optical Design and Simulations

2.2.1 Design

The materials presented in chapter 1 highlight the importance and application driven selection of each material that can be used for PICs. For example, if we are looking for broadband materials, SiN or photosensitive polymer resist would be ideal candidates. With SiN, it is a well established platform [1, 2] but comes at the cost of being expensive with a slow fabrication time compared to polymers. Therefore, polymers that are also photosensitive are easy to prototype, commercially available and low cost per unit device fabricated [3, 4, 5]. However, it is important to note that polymers are often not offered on commercial multi-project wafer (MPW) for photonic waveguides due to specific processing requirements and difficulty to integrate. The polymer of choice is SU8, manufactured by only Kayaku [6]. The first aspect of the design is considering the propagation medium and the dimensions. For initial investigation, we chose SU8 which can be spun to 5 micron thick and patterned to be 10 micron wide as indicated in fig. 2.1. Furthermore, as displayed in fig. 2.1, the substrate is chosen to be glass which acts as a lower index medium, allowing for propagation in the SU8 medium and further offers as a low cost and rapid turnaround option [7, 8]. The y and z axis in fig. 2.1 indicates the simulation area in which mode simulations can be carried out in. The simulation tool used is Tidy3D, an online cloud based photonic device simulator [9, 10]. The principle behind the simulations is solving Maxwell's equation, spatially and temporally to output electromagnetic field intensity distributions for confined waveguide mediums and other photonic devices [10]. Within the software, user selected field and mesh sizes define the accuracy of the region where maxwells equations are solved (2D or 3D solving). In Tidy3D, user-defined simulation regions and mesh sizes set the solution accuracy in two or three dimensions, with sub-wavelength features often requiring single-digit nanometre grids that significantly increase computational cost. The fields are advanced on a staggered Yee grid, with material properties defined through spatially varying permittivity and loss, sources implemented as modes or broadband excitations, and open boundaries modelled using perfectly matched layers. The approach assumes linear, time-invariant materials and represents geometry on a Cartesian grid, leading to discretisation errors for curved interfaces and limiting the efficiency for large or high-Q structures, while remaining well suited to modelling complex integrated photonic components. Tidy3D, as a cloud based simulator offers low cost and accessible platform for simulating photonic devices without the need of a high end PC. It is important to note there are other available simulation tools such as Ansys Lumerical and MEEP.

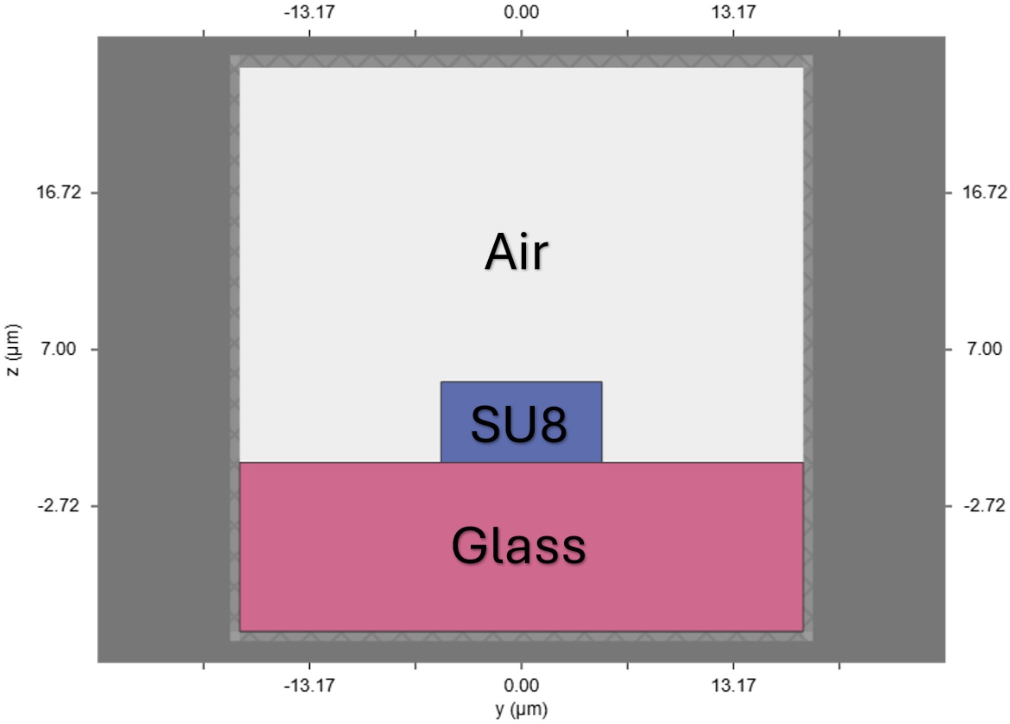

Figure 2.1: Cross sectional simulation setup for SU8 on glass design

For broad ranges of wavelengths, these waveguides will be multimode at shorter visible wavelengths, which for long range data communication dispersion effects become an issue [11, 12]. However, for spectroscopy, the multi mode regime will benefit from the amount of light coupled to the waveguide [13, 14]. The modal overlap between single mode fibre (SMF, or typically SMF-28) and waveguide will also be high, allowing for already low coupling losses between fibre and facet [15]. Using the simulation setup shown in Fig. 2.1, a mode simulation at 635 nm reveals the modal structure within the SU-8 waveguide, as shown in Fig. 2.2. The scale bar on the right-hand side indicates the intensity of the electromagnetic field within the waveguide medium. At visible wavelengths the waveguide operates in a highly multimode regime, as the 5 × 10 µm cross-section is several times larger than the optical wavelength, allowing multiple transverse field distributions to be supported simultaneously. This results in a complex modal structure, with significant leakage into the substrate and air cladding arising from the relatively low refractive-index contrast of the confined modes. Finally, these dimensions provide a large surface area for adhesion to the substrate, reducing the likelihood of feature delamination.[16].

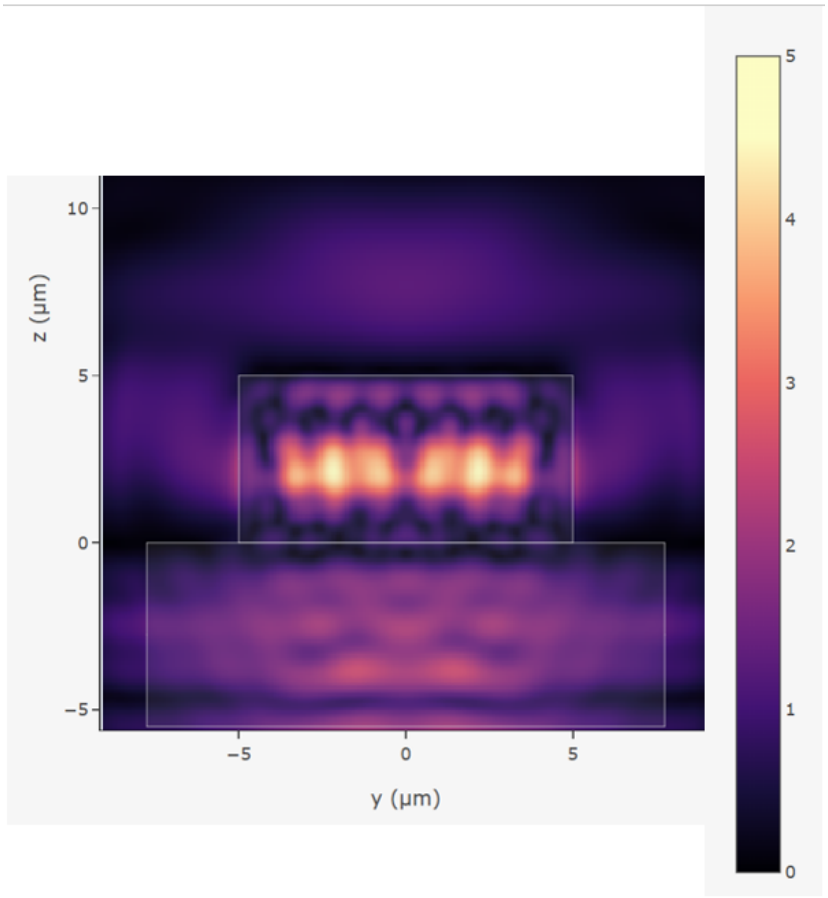

Figure 2.2: Tidy3D simulation of SU8 waveguide structure at a wavelength of 635nm

With the substrate and waveguide medium selected, we have to consider a coupling regime that is effective across an ultra broadband range of wavelengths. By introducing 45° slopes to the waveguides, we create a region where incident light is total internally reflected, causing a beam perpendicular to the direction of propagation within the waveguide [17, 18]. Furthermore, a gold reflective surface used on the turning mirror slope allows for overlayed waveguides, which keeps the mode confined. In turn, this solves a problem for using an air gap between waveguide and mirror medium that would increase losses due to expanding beam propagation in air (fig. 2.3).

2.2.2 Simulation

To predict the performance of the waveguides and vertical couplers, further designs and simulations can be carried out, once again using Tidy3D. The photonic structures were modelled from the waveguide foundations in fig. 2.1, with the addition of an embedded gold prism as a reflective layer, as indicated in fig. 2.3. The prism at 45-degrees to the glass substrate would redirect the input mode that is initially injected, as indicated by the red arrow in fig. 2.3a. It is important to note that at shorter wavelengths, the Au prism will absorb more light and alternative metals can be used, such as Aluminium (Al) when working with devices that emit in the green or blue such as GaN LED's. Furthermore, dielectric mirrors fabricated using SU8 could be used but fabrication limits can apply due to the distance between SU8 waveguide and SU8 prism.

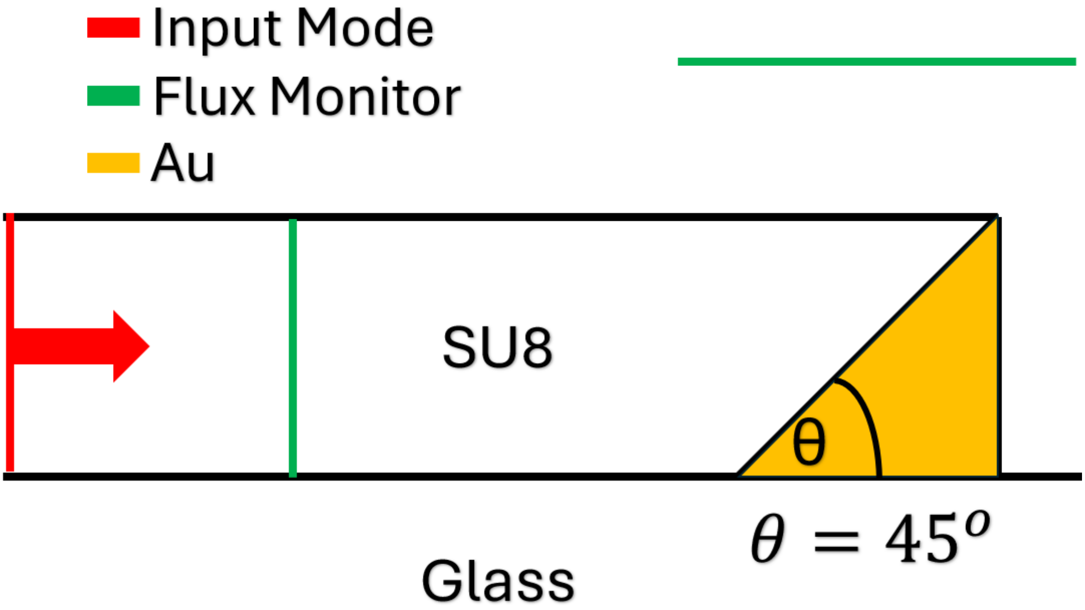

Figure 2.3: Schematic of simulation setup, highlighting the input mode and monitors for data acquisition and

To monitor the field dynamics and obtain a theoretical loss measurement induced by the vertical scattering of light, two flux monitors indicated in green on fig. 2.3a are inserted within the waveguide (F1) and above the point of vertical scattering (F2). By analysing the recorded flux values at these locations, it is possible to estimate the losses introduced by the mirror vertical coupling structure. Furthermore, the design illustration in fig. 2.3a is shown within the Tidy3D simulation window (fig. 2.3b), where the mode monitor is setup for a z-section view of the electromagnetic field distribution of the system. Simulations were carried out at wavelengths of 635nm and 1550nm in fig 2.4 and fig. 2.5 respectively.

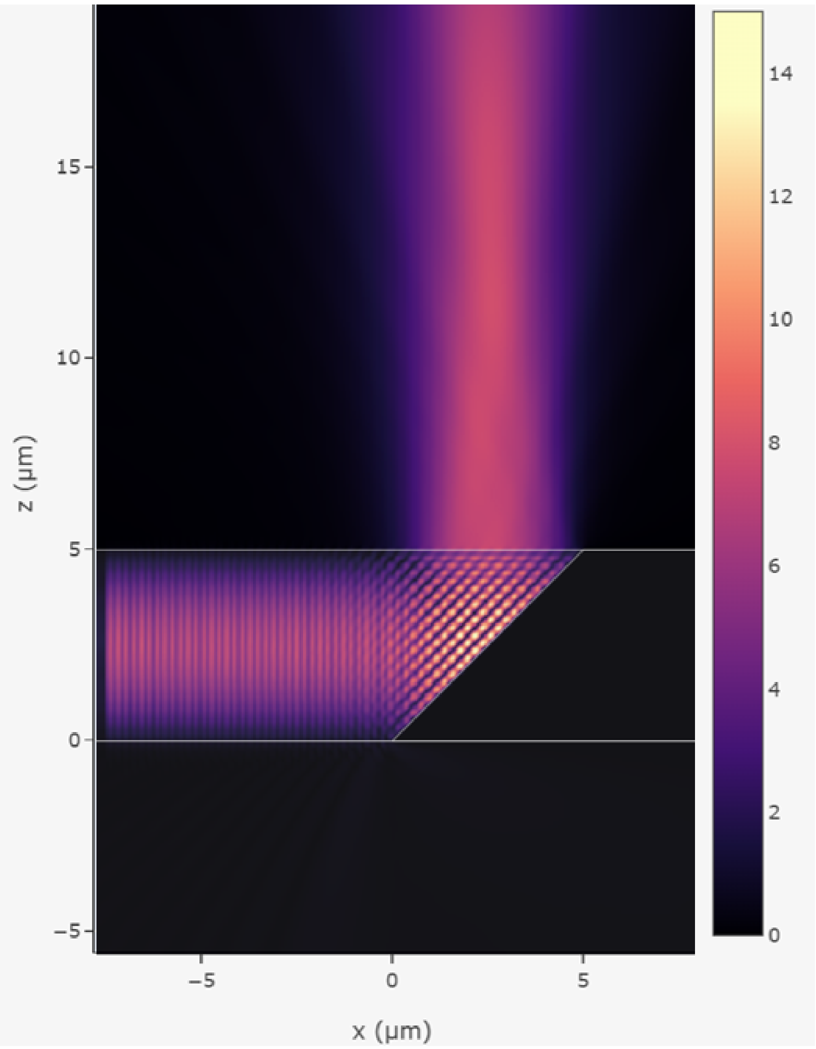

Figure 2.4: Waveguide mirror simulations at wavelength of 635nm

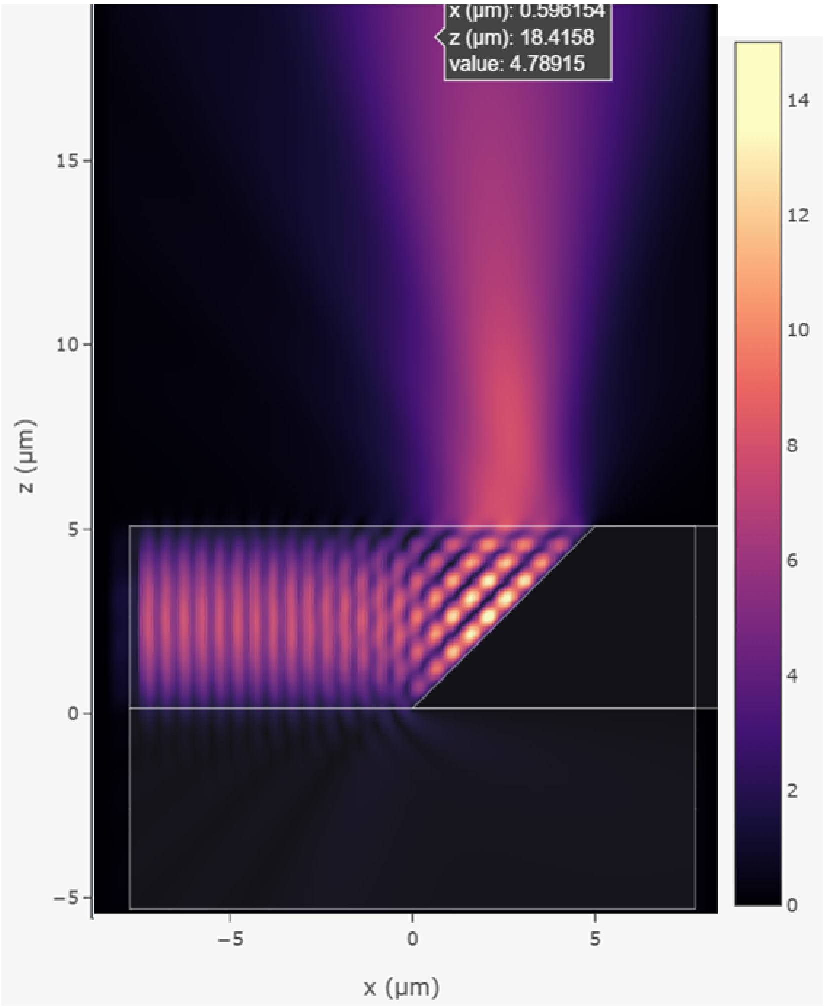

Figure 2.5: Waveguide mirror simulations at wavelength of 1550nm

By simulating at these wavelengths, we can target the initial broadband behaviour and characteristics of the devices. A comparison between the two simulation scenarios reveals that the most prominent differences lie in the beam divergence and the presence of interference fringes around the gold (Au) mirror region.

Assuming an idealised, lossless waveguide, flux monitors indicated in fig. 2.3, recorded flux values can be taken at these locations, where it is possible to estimate the losses introduced by the mirror vertical coupling structure. It is important to emphasise that these simulated losses are primarily due to back reflections resulting from angular mismatch at the mirror interface. In contrast, experimental losses in fabricated devices are typically more pronounced, owing to fabrication related imperfections such as surface roughness, metal grain boundaries, and waveguide misalignments.

The optical loss introduced by the mirror region can be calculated using the flux ratio between the monitors:

$$L_{\text{Mirror}} = 10Log_{10}(F_2/F_1)$$

Obtaining the following theoretical results in fig. 2.6 and fig. 2.7.

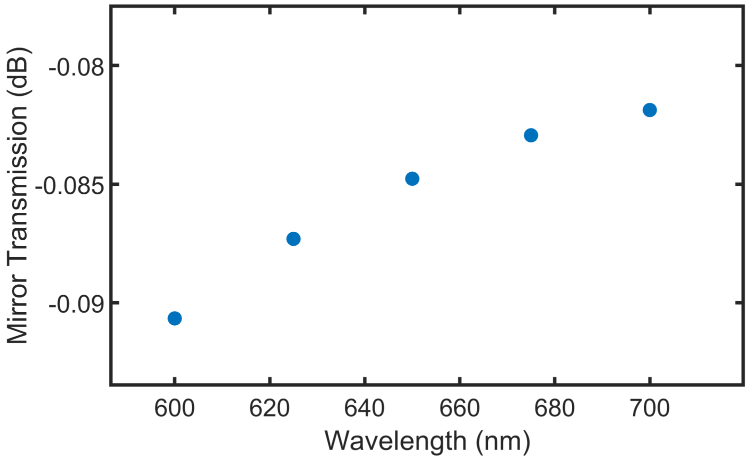

Figure 2.6: 600-700nm transmission simulation results

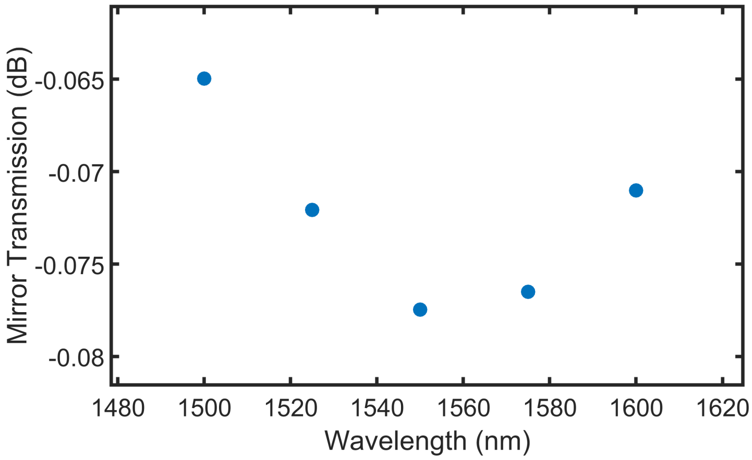

Figure 2.7: 1500-1600nm transmission simulation results

Based on the simulation results and the data obtained from the flux monitors in fig 2.6 and fig 2.7, the losses induced by the gold mirror coupling region are found to be less than 0.1dB across the simulated wavelength range. These losses are primarily attributed to back reflections caused by incident rays striking the mirror at angles that deviate from the optimal angle required for efficient vertical coupling. Furthermore, additional losses arise from the simple reflections at a refractive index boundary between layers [19] .This behaviour is evident in the mode simulations, where interference patterns are observed in the vicinity of the coupling region. Finally, most losses can be attributed to the absorption of light by the Au mirror. This value range up to a 2% absorption of incident light.

However, in practical implementations, the actual losses are expected to be considerably higher. This discrepancy arises from fabrication induced imperfections [20], including the surface quality and uniformity of the Au mirror, as well as imperfections in the overlaying waveguide region. Such non idealities introduce additional vertical scattering and reflection, thereby degrading the overall coupling efficiency.

2.3 Fabrication methods

2.3.1 Platform Selection

To achieve rapid prototyping and low cost production of vertical couplers for integrated photonic circuits, materials must be readily available, and be compatible with the largest range of wavelengths possible. As previously mentioned in literature, Silicon Nitride and SU8 have large transparency windows. However, to minimise fabrication time, SU8 was selected for this work. To have a compatible substrate that doesn't absorb light, a glass substrate is suitable due to the lower refractive index when compared to the index of the passive SU8 waveguides. Furthermore, a glass substrate allows for backside illumination, especially for visible wavelengths where an SOI platform would absorb these wavelengths.

2.3.2 Grayscale Lithography

To fabricate planar photonic structures with arbitrary surface relief profiles, direct write laser lithography (DWL) presents a flexible and precise method for producing customised patterns in photo responsive resists [21, 22]. This approach enables the direct fabrication of integrated photonic structures on a chip scale platform without the need for photomasks, thus supporting rapid prototyping and bespoke device geometries. The achievable resolution and aspect ratio are primarily governed by the wavelength of the writing laser and the associated spot size, with shorter wavelengths and tighter focusing enabling finer features and steeper sidewall angles. Furthermore, the thickness of the resist also plays an important role for the aspect ratios that can be achieved. For example, in thicker resists, high aspect ratio features are difficult [23, 24]. Due to the nature of the laser writing process, the fabrication of high-quality devices with large physical dimensions is often time-consuming and inherently limited in throughput, making the technique poorly scalable to full wafer-level production. As patterns are written serially, fabrication time increases rapidly with device length and complexity, which restricts its suitability for large-scale or high-volume manufacturing. Furthermore, stitching errors arising from the finite write-field size are difficult to completely eliminate when fabricating extended or densely patterned structures. These stitching artefacts can introduce discontinuities, line-edge roughness and dimensional non-uniformities, ultimately degrading the optical performance of the fabricated devices through increased scattering loss and phase errors.

Standard DWL systems, such as the Heidelberg DWL66+ (fig. 2.8), operate under the assumption of a uniform intensity distribution during exposure, effectively restricting the process to two dimensional (2D) patterning. However, by locally modulating the exposure dose in a spatially resolved manner, so called "2.5D" structures may be realised—structures that possess smoothly varying topography in the vertical dimension, though still constrained to fabrication strategies that cannot accommodate true undercuts or disconnected volumes [25, 26]. Unlike two photon polymerisation (2PP) systems, which allow volumetric (3D) writing with sub diffraction limit resolution, DWL systems cannot fabricate structures that require internal voids or significant overhangs due to the inability to focus intensity below the surface layer of a spun, planar layer of photoresist.

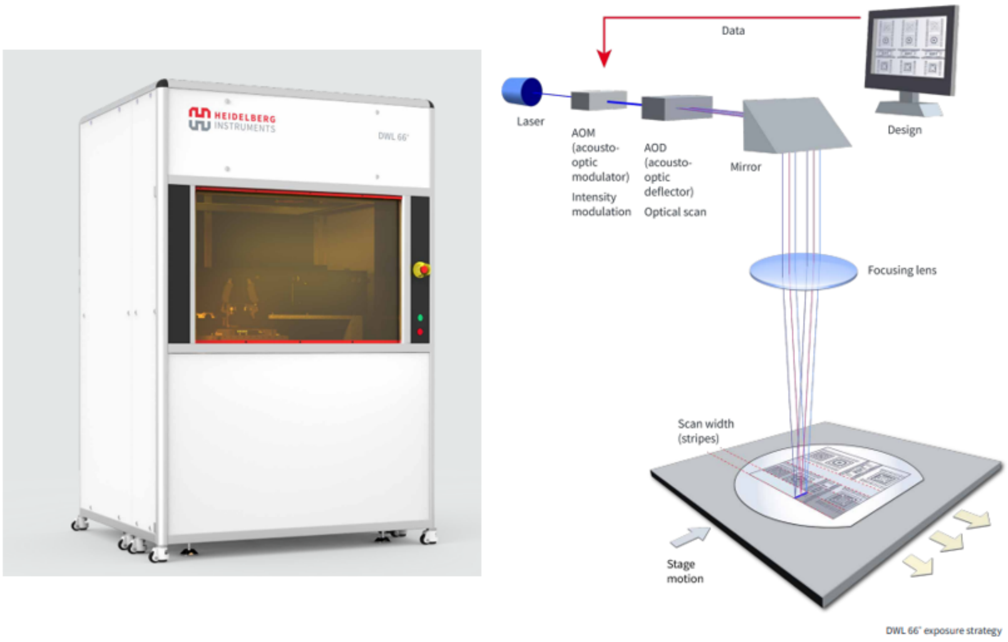

Figure 2.8: Heidelberg DWL66+ System

The realisation of 2.5D structures using grayscale lithography necessitates two interrelated components: a design representation of the structure and a method for controlling the spatial exposure intensity. In this context, two widely adopted digital formats are used: stereolithography (.STL) and bitmap (.BMP) files. Both formats are compatible with the DWL66+ system, which interprets the vertical dimension of the desired structure as a series of 256 discrete grey levels, corresponding to incremental changes in exposure dose.

STL files represent 3D structures as triangulated surface meshes, typically created in CAD environments such as Autodesk Fusion 360 or generated through algorithmic methods using scripting languages like Python. For instance, a simple planar optical component might be designed as a 5μm thick waveguide taper with a 45° slope on either side. These STL files are highly flexible and allow the creation of arbitrarily shaped surfaces. However, the DWL66+ imposes a stringent size limitation of $100\times100\mu m^2$ per exposure for STL based elements. This poses a challenge for large designs as it requires complex strategies for design layout and overlap. To implement larger designs, complex exposure grid configuration strategies must be adopted. Moreover, due to the polygonal approximation inherent in mesh representations, smoothly varying features such as spherical lenses can suffer from discretisation artefacts unless extremely fine mesh resolution is used, which increases processing time and computational complexity.

As an alternative, BMP files provide a direct method for encoding grayscale information. Each pixel in a BMP image represents a discrete intensity level, enabling fine control over the vertical profile of the fabricated structure. These images can be programmatically generated using numerical computing environments such as Python, MATLAB, or Octave. Unlike STL files, BMP based exposures are not intrinsically limited in lateral size, although practical constraints arise due to file size and computational demands. For the DWL66+, two write heads are available: a standard 5mm head and a high resolution (HiRes) head. The Hi-Res head achieves a pixel size of approximately 50nm, while the 5mm head has a larger pixel size of 200nm. Consequently, high resolution structures over large areas can produce extremely large files—for example, a $300\times300\mu\mathbf{m}^2$ BMP design for the HiRes head may approach 1GB in size, which can result in software processing failures. To mitigate these issues, large BMP designs are often split into smaller subregions, each processed independently within the Heidelberg software environment.

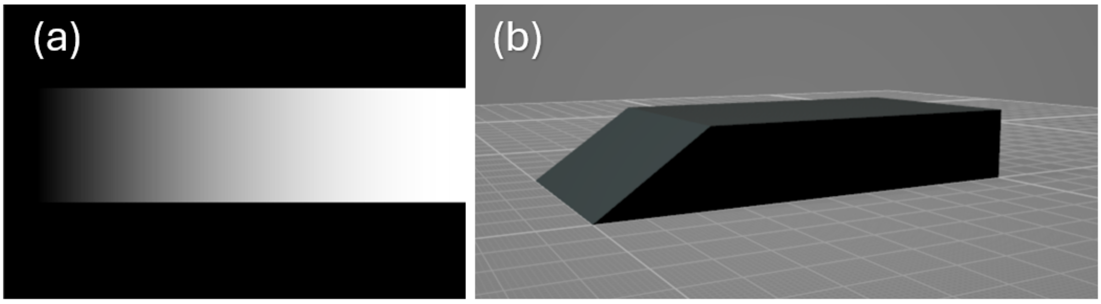

Figure 2.9: Example of .BMP design and .STL structure for 45 dergee micro structures

To better illustrate the design profiles in correlation to grayscale, fig. 2.9 displays the .BMP format (a) and .STL format (b). The white structure (max grayvalue) os the .BMP gradually decreases from right to left to form a 45-degree turning mirror while the STL component offers a user design 3D model of the turning mirror design.

The exposure intensity at each point in the design is controlled by mapping pixel grey values to laser intensity or exposure dose. For a negative tone photoresist, grey value 0 typically corresponds to 0 exposure (i.e. complete removal during development), while grey value 255 corresponds to maximum calibrated intensity. The exposure dose profile along a structure, such as a sloped surface, can be designed by specifying a monotonic gradient in grey values e.g., from 5 to 100 exposure along a linear ramp, corresponding to grey values 1 and 255. However, the actual physical topography resulting from this exposure gradient does not necessarily correlate linearly with the intended grey value distribution.

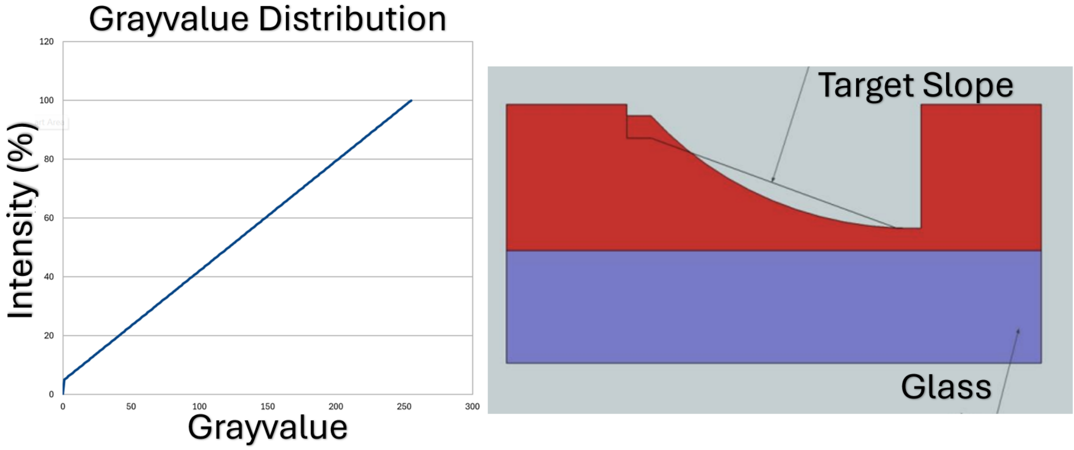

Figure 2.10: Linear grayvalue distribution applied to fabrication process, resulting in nonlinear slope for positive resist

As displayed in fig 2.10, the intensity distribution is plotted on the left hand side with a linear increase intensity with grayvalue. With this example applied to a positive resist on the right hand side, the target slope is illustrated as a linear decrease in resist height, while the fully developed sample displays a nonlinear slope that needs correction.

This discrepancy arises due to a combination of proximity effects, scattering, and nonlinear resist behaviour. The writing spot, while highly focused, has finite spatial extent and can lead to inadvertent exposure of adjacent regions—a phenomenon known as the proximity effect [27]. Additionally, back reflections from the substrate–resist interface and internal scattering further complicate dose distribution, especially in closely packed or high aspect ratio features. As a result, the fabricated topography often exhibits parabolic or otherwise distorted profiles relative to the intended design. This effect is displayed in fig. 2.11, where a lithography beam is focused on to the substrate, indicated in green and the beck reflections at the resist-substrate interface. Furthermore, the top sectional view on the right hand side offers a better view of the proximity error effect, exposing adjacent regions of the photoresist outwith the focal point of the writing beam.

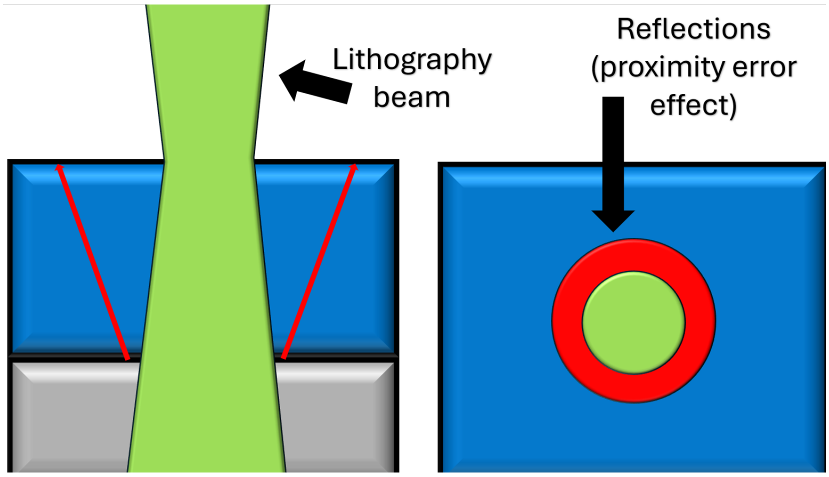

Figure 2.11: Diagram of the proximity error effect caused by beam waist and reflections between boundaries

To compensate for these deviations, a process known as proximity error correction (PEC) is employed [28]. In the absence of commercial PEC software (which can be cost prohibitive), an empirical iterative process is typically used. The fabricated structures are characterised, for example using surface profilometry, and the measured height profiles are compared with the design intent.

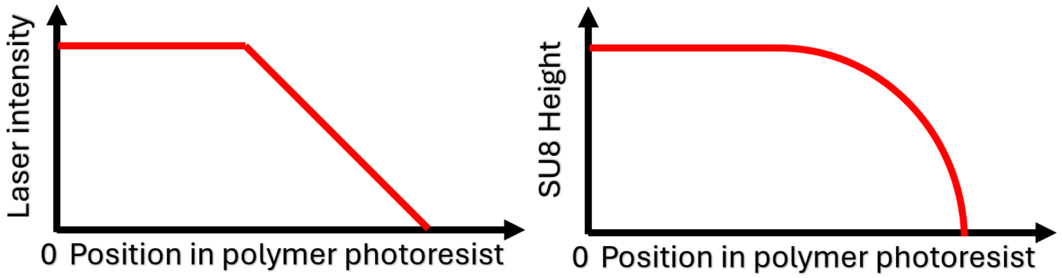

Figure 2.12: Exposure dose and example of profiled structure due to proximity error effect

Figure 2.13: Optimised exposure curve to realise desired structure

As illustrated in fig. 2.12, an example of a linear exposure dose does not correlate to a linear slope in the developed sample - often resulting in a curved slope far from the desired pattern. With optimisation and data interpolation, the exposure distribution can be calibrated after many attempted exposure and calibration runs. For example, fig. 2.13, illustrated and optimised laser intensity distribution of the exposure that results in a full developed sample that directly corresponds to the designed photonic components in either the STL or BMP format. With reference to fig. 2.14, a grayscale bmp design is exposed to a positive photoresist to produces a direct correlation to the design and actual device, noted in the blue structure.

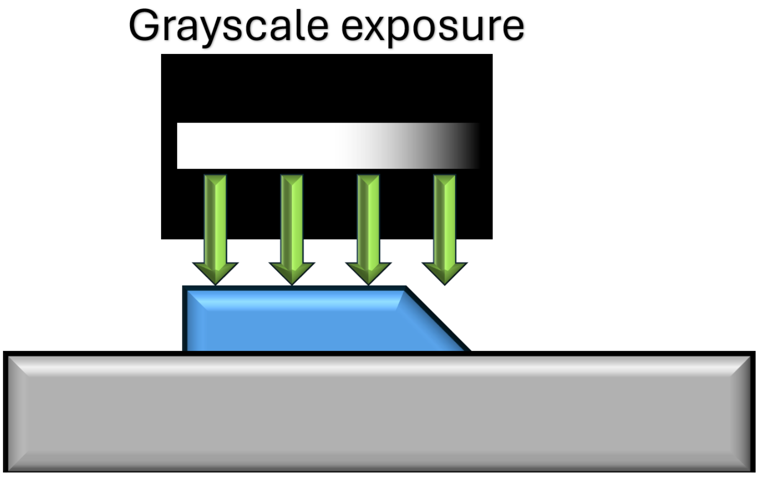

Figure 2.14: Example of generated BMP designed 45° slope transferred to photoresist

2.4 Backside Couplers

2.4.1 Design

Coupling from an external source to a PIC which is of the SU8 on glass platform can be completed using backside coupling. By using the principle of TIR, injecting light to a structure that reflects all light due to the incident angle of light on the sloped surface, reflecting light to and from the optical cavity. Therefore, by changing the surface angle of the SU8, a turning mirror cavity can be used to redirect light to planar waveguides. To obtain these designs, we can apply the use of grayscale lithography to define a structure. For example as illustrated in fig. 2.15, a 45° backside turning mirror to planar waveguide and back to a separate 45° backside turning mirror.

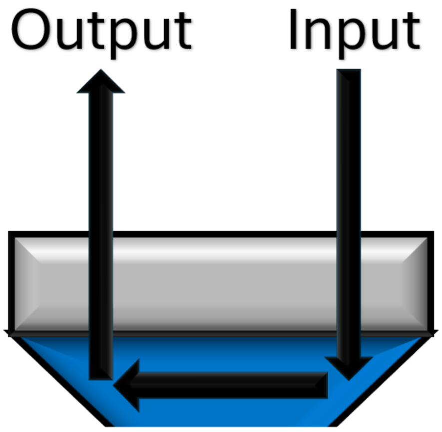

Figure 2.15: Schematic of backside coupling for vertical injection and collection

These designs allow for light to be injected through one backside coupler, propagate through the waveguide and then emitted back via the second turning mirror. This can show via rapid prototyping that the devices work and can therefore be improved depending on the application.

2.4.2 Fabrication

To fabricate these devices, we first need to spin a 5 micron thick layer of SU8 on to the glass cover slip substrate. With a spin speed of 500rpm for 5 seconds and then a spin of 3000rpm for 30 seconds. After the spin has successfully covered the substrate with a uniform layer of SU8, at 5μm post bake step is used to activate the photo reactive polymer [29, 30]. To ensure there is no stress induced between the resist and substrate during any heating step, a first 60s soft bake step at 65°C is carried out and then the hot plate is slowly ramped up to 95°C where it stays for a further 3 minutes. After sufficient cooling, the sample is loaded in to the Heidelberg DWL66+.

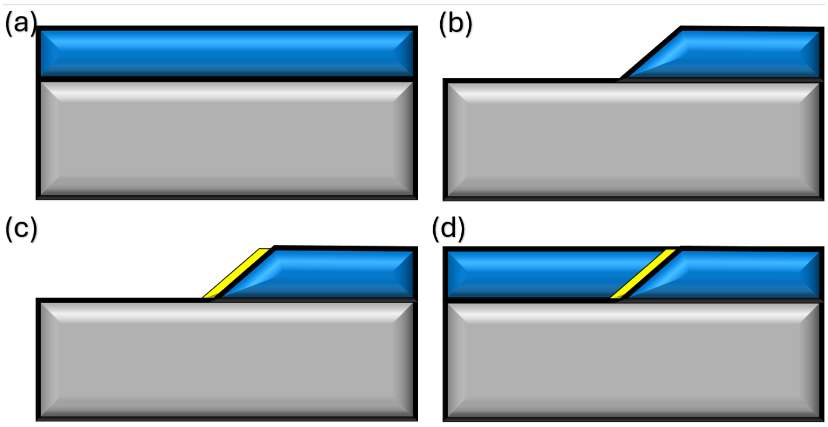

Figure 2.16: Figure 2.18: Illustration of fabrication process using (a) SU8 on glass platform, (b) grayscale lithography patterning, (c) e beam metal deposition and (d) waveguide mirror overlay.

The resist is exposed using the Hi-Res write head, operating at a wavelength of 375nm. After the design has been exposed on to the sample, a post exposure bake is carried out, to activate the cross linking process of the photoresist. The post exposure bake is carried out for 2 minutes at a hot plate temperature of 95°C. To remove the excess resist that has not been exposed involves using an assortment of solvents, this development process also further cross-links the exposed regions of the resist. Two beakers are prepared with sufficient PGMEA and IPA, where PGMEA is the primary developer, and the IPA is used to rinse off the excess resist [7]. Firstly, the sample is submerged in PGMEA for 60s, then in IPA for 10s, back to PGMEA for 15s and finally back in to IPA for 10s. Once developed, the sample can be inspected using standard microscopes. If exposure and development has been successfully, the cross linking of the structures needs to be completed, especially for further device processing. With a hot plate set between 150-200°C, the sample is hard baked for 1 hour plus, with frequent checks under a microscope to monitor the re-flow of the resist. An illustration of the backside coupler fabrication process is illustrated in fig. 2.16 (a-b), where the SU-8 is highlighted as the blue structure with the glass substrate in gray. Furthermore, table 2.1 shows a concise step by step processing flow for these devices

Process	Tools	Time
Solvent clean	Acetone, Methanol, IPA, DI Water	5 min. per solvent
Dehydration	Hot Plate	100°C+ 15 min.
$O_2 ash$	Matrix Asher	200°C 10 min.
Resist spin	Spinner	500rpm 5s, 4500rpm 45s
Soft bake	Hot Plate	110°C 3.5 min
Lithography	Heidelberg DWL66+	N/A
Post exposure bake	Hot Plate	110°C 2min.
Development	PGMEA, IPA	60s, 10s, 15s, 10s
Hard bake	Hot Plate	200°C 1+hour

Table 2.1: Process flow table for the preparation and fabrication of planar waveguide to vertical mode mirror couplers

2.4.3 Test Device Verification

To verify the initial fabricated devices, some steps need to be carried out to continue with prototype fabrication, profilometry and backside injection tests. To ensure a 45° angle has been achieved for the SU8 structures, the profile of the grayscale regions need to be examined. This can be done in multiple ways: AFM scan [31, 32], white light interferometry [33] and AlphaStep contact profiling [34]. Each method has it's own advantages and disadvantages

Profiling Type	Advantage	Disadvantage
AFM	High accuracy + 3d imaging	Convolution
White Light	Rapid and large scan	SU8 transparency
AlphaStep	Large scan area	No 3D and contact damage

Table 2.2: Profiling techniques for PIC components, included advantages and disadvantages of approaches

For the purpose of high resolution surface profiling of the fabricated photonic structures, a NC-SSS (non contact, super sharp silicon) cantilever was employed in the atomic force microscopy (AFM) measurements [35].

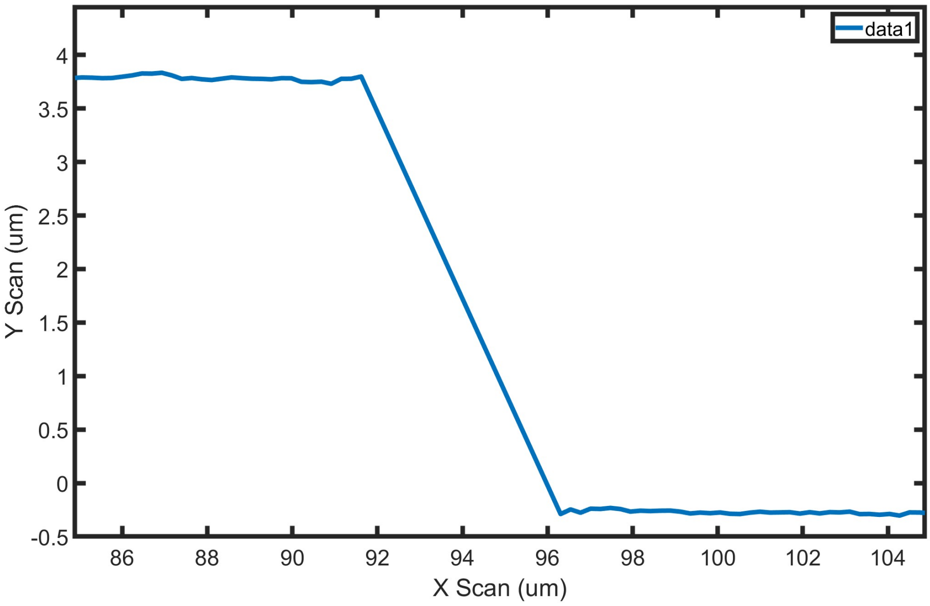

Figure 2.17: AFM scan of 45° mirror structures using the NC SSS cantilever

In the case of our fabricated devices, the target 45° mirror structures forming the basis of the backside couplers were successfully realised with the data displayed in fig. 2.17 using the mentioned AFM techniques to acquire the vertical profile of the fabricated devices to be 45-degrees relative to the substrate. These slanted features were designed to reflect incident light via total internal reflection (TIR), thereby enabling vertical in- and out-coupling of light to and from planar waveguide geometries. To experimentally validate the optical performance of these couplers, an in situ optical transfer printing setup was employed. This rig allows for precise positioning of the devices under optical interrogation while enabling real time monitoring of the light coupling via an integrated imaging system [36, 37].

Before direct injection, a white light profiling scan was carried out. Due to the nature of the mirrors and the interference method used to profile structural heights, a dark region is shown on the final scan where the mirrors are fabricated. Due to the light not being returned in the scan.

Using a laser source emitting at a wavelength of 638nm, light was injected into one of the fabricated mirror regions from the backside of the substrate. The optical injection was aligned to the mirror facet such that the incident beam would undergo TIR at the 45° surface, subsequently propagating through the SU8 waveguide layer. This process is similar to the experiments carried out by S. Bommer, et. al [36], and the illustration in fig. 2.15, shows the optical path taken by light.

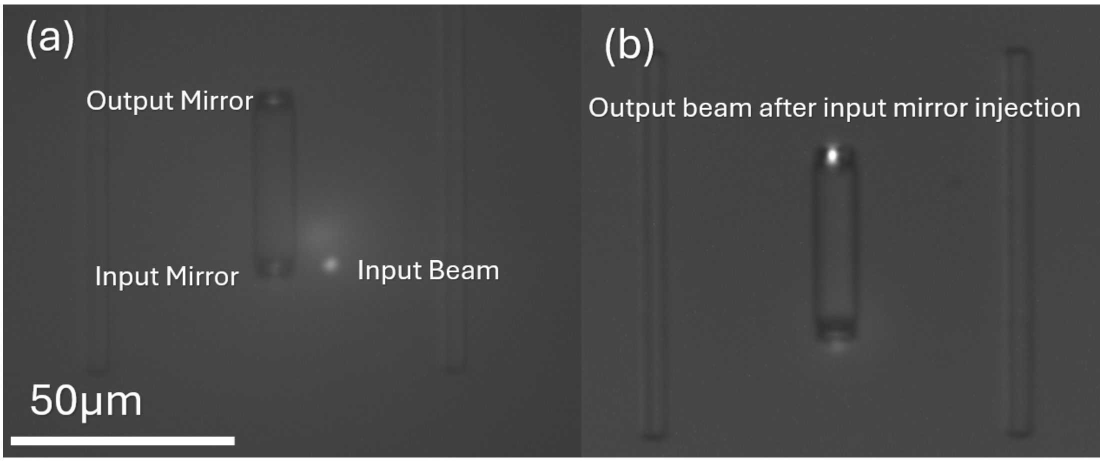

Figure 2.18: Camera image from transfer print and In Situ monitoring setup with (a) reference spot and (b) output spot, with injection on bottom mirror section

As shown in fig. 2.18, the emitted light from the waveguide was monitored using an overhead imaging system integrated into the setup. The captured images show clear evidence of beam emission from the same device, indicating successful coupling through the fabricated 45° backside mirror structures. The sample was mounted onto an x-y-z stage that is used to align the sample to the beam spot shown on fig. 1.18.

2.5 Backside to Topside Couplers

2.5.1 Thin Film Metal Reflective Coating

The idea for turning working backside couplers to topside couplers is to reduce the number of interfaces that the emitted light has to interact with due to the change in effective beam waist at the next point of coupling between interfaces and free propagation length through the substrate that increases beam size due to divergence. Therefore, the illustration of the topside coupler can be seen from fig. 2.17c and operates on the principle of having a highly reflective thin film metal interface between pre-defined 45°

structure and overlay waveguides. With the predefined structures, we use SPR 220 4.5 on the samples and open up metal deposition windows that extend outwith the mirror region by 1 additional micron across the entire perimeter. This allows tolerance with the overlay alignment of the Heidelberg DWL66+ and also helps with the lift-off process of the deposited metal. After exposing the metal opening designs on the positive resist, the resist is developed in a solution of 1:1 MicroDeveloper and DI water for 45s and then submerged in to DI water to halt the development process. The samples are then inspected using a microscope to ensure the pattern has been exposed and developed all the way down to the substrate [38, 39].

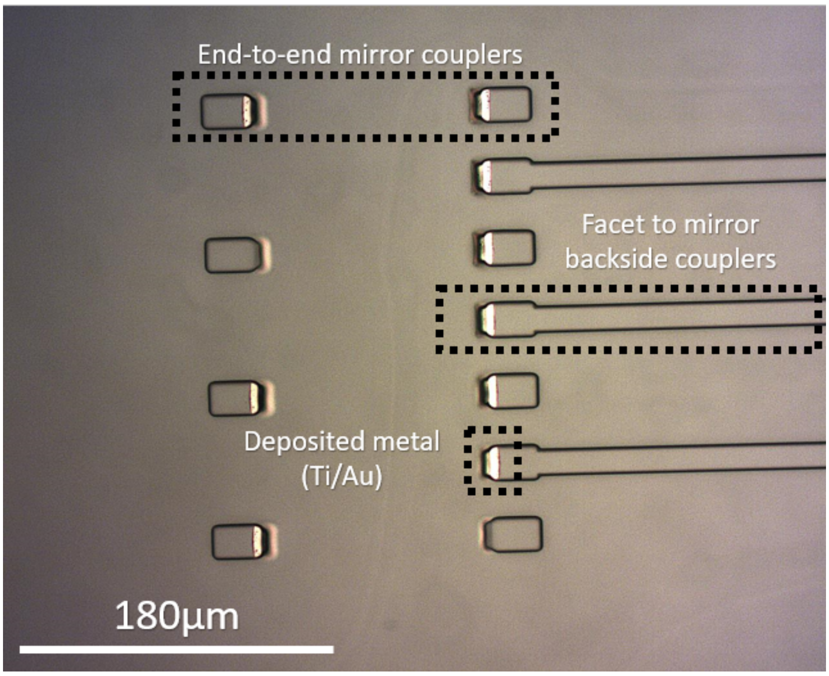

Figure 2.19: Microscope image of lift results. E beam deposition of 50nm Ti and 200nm Au

With the metal openings prepared, metal deposition is carried out using e-beam metal evaporation using a Temescal BJD-2000 [40, 41]. To ensure high reflectivity across a broad range of wavelengths, the material used was gold [42, 43, 44]. The metal deposition process consists of a 50nm Ti deposition for enhanced adhesion between metal and SU8, and then a 200nm metal deposition of Au. To lift off excess metal, a solution of 1165 is prepared in a beaker with the sample fully submerged, allowing for the 1165 to dissolve the positive photoresist and lifting off excess metal. To help with the speed and efficiency of lift off, the beakers can be set in a hot bath set at 85°C, or left overnight at room temperature. A pipette is used to agitate and help with lifting off excess metal. However, this can lead to too much agitation that can strip the entire sample of metal and even delaminate SU8 structures, if they haven't been sufficiently hard baked for long enough. Fig. 2.20, shows a microscope image of the initial devices after metal lift-off. Contained in the devices is a combination of end-to-end mirrors that would allow for topside injection and collection, plus, end waveguide facet injection to mirrors where further waveguide fabrication to embed the mirrors will be discussed in the following section.

2.5.2 Waveguide Overlay

The final step of the devices is to overlay SU8 waveguides with the highly reflective mirror surfaces. To achieve this, the same technique was used to spin a 5 micron thick layer of SU8 on to the substrate to prepare for laser lithography. With the samples spun and design prepared, the design is exposed over the sample and developed as previously described for the original SU8 exposure and development process.

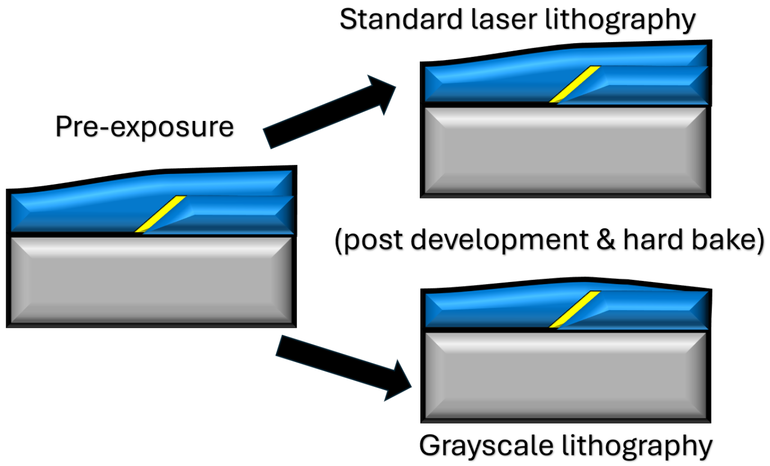

Figure 2.20: Schematic of excess photoresist when spun over pre defined structure and resulting device after processed using standard laser lithography .

However, due to the existence of a predefined structure already on the substrate, the second spin of SU8 will be disturbed by this surface and result in a non-uniform layer of resist as illustrated in the pre-exposure schematic in fig. 2.20. Therefore, when carrying out a simple laser lithography exposure, the waveguide overlap with mirror will be poor, with excess resist over the vertical coupling region as illustrated in the standard laser lithography schematic in fig. 2.20 . Furthermore overlap can be illustrated in fig. 2.21 and by considering the direction of propagation from the input facet, the poor overlap opens a new direction of propagation which reduces the amount of light directed on to the mirror and hence, reduce the vertical transmission of the system.

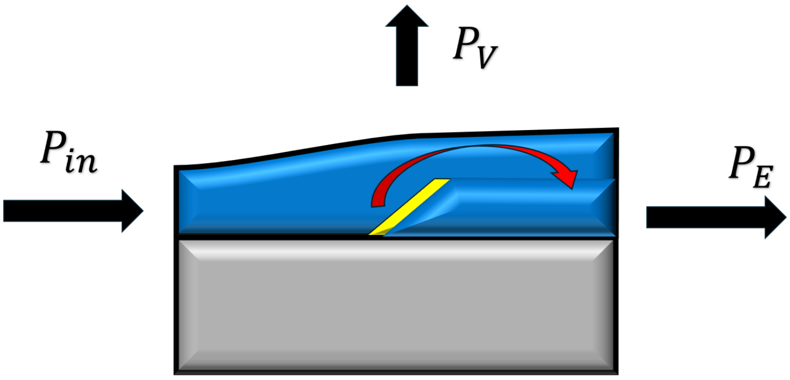

Figure 2.21: Illustration of poor waveguide mirror overlay, causing light to travel to end facet

To optimise the excess resist height at the overlap region, we can employ a grayscale exposure to counteract the increase in the resist height after spinning on to the substrate, with an example of the optimised device shown in fig. 2.21 as the grayscale lithography device, and when compared to the excess height of the standard lithography device, the overlap becomes better optimised. The design consists of a STL element resembling an inverse mirror. The design is used to decrease the exposure in the regions where resist height is maximised, and then linearly increase the exposure, back to match the exposure of the waveguides. However, it is still a challenge to perfectly fabricate the waveguide overlay due to the back reflections of the exposure beam from the Au mirror [45]. The reflectivity at Au is low at the wavelength of the exposure beam but slight back reflections can increase the exposure dose leading to challenges in very broadband

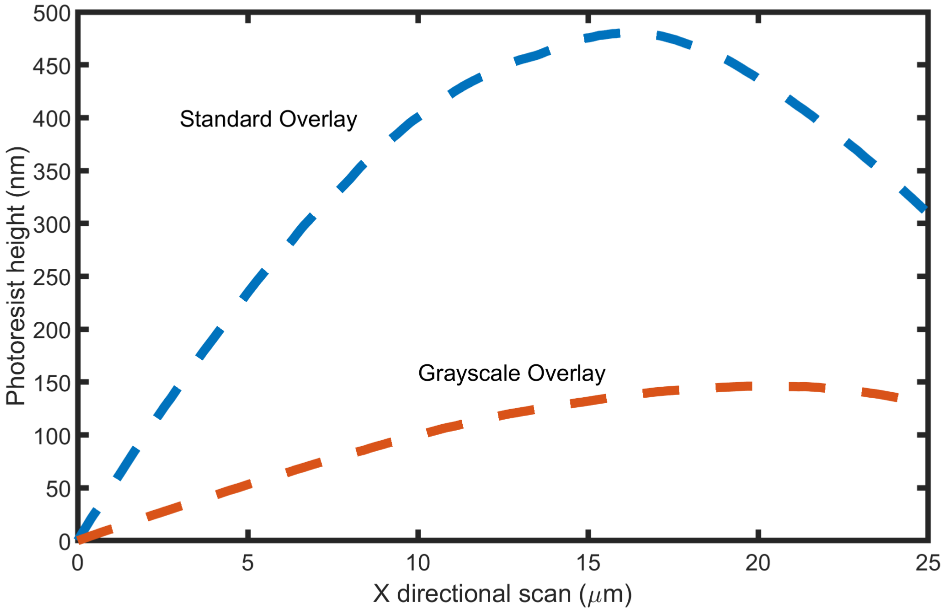

Figure 2.22: Variation of maximum photoresist height offset when applying separate lithography methods for overlayed waveguides.

mirrors [46, 47].

Using the same techniques described in section 2.4.3, an AFM scan of the poor overlap can be indicated in fig. 2.22, with a 500nm increase in excess photoresist height at the overlap region.

When using this method to optimise the devices, we profile and compare the grayscale exposure to the standard exposure using AFM measurements. The standard exposure results in a 500 nm excess height over the transition region while the grayscale exposure reduces this excess height to below 100 nm. This reduction in height is essential to maximise the amount of light incident upon the mirror and thus maximise the total output power for vertical coupling. This is optically measured with respect to the end facet waveguide. With a standard exposure the power lost through the waveguide is 4.4 dB, while the optimised grayscale exposure reduces the loss to 0.4 dB. For example, in fig. 2.23 and fig. 2.24, end transmission images were taken of both devices.

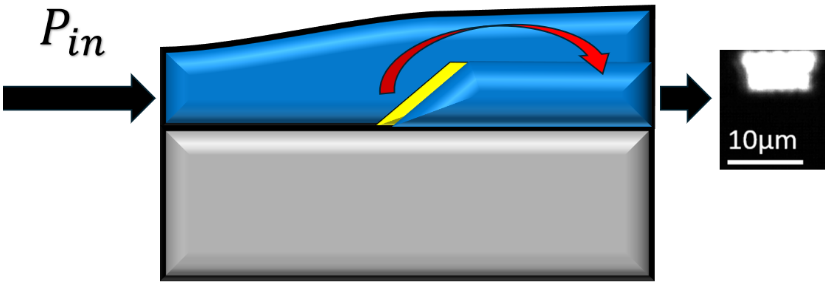

Figure 2.23: lustration of waveguide overlay with standard lithography exposure and captured end facet.

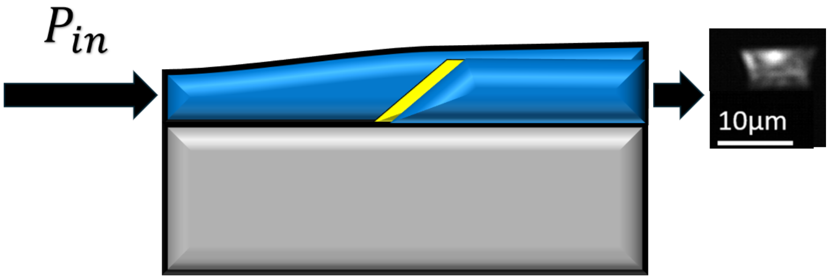

Figure 2.24: Illustration of waveguide overlay with grayscale lithography exposure and captured end facet image.

By comparing fig. 2.23 and 2.24, the imaged mode of the standard overlay is apparently brighter than the grayscale overlay devices, almost over saturating the image with the amount of light. This supports the reduction in loss measurements between the two systems. With the low output power and visualisation of the grayscale device facet, it is clear that with the same input power, the majority of light is incident on the vertical coupler. To determine the power of the vertical mirror output, the following chapter will investigate and show the measurements.

2.6 Summary

This chapter presented the design and fabrication of broadband vertical waveguide mirror couplers on an SU-8 on glass platform. The optical design was validated using

Tidy3D, with mode and flux-monitor simulations at 635 nm and 1550 nm indicating efficient vertical redirection via 45° turning mirrors and predicted mirror losses below 0.1 dB across 600–700 nm and 1500–1600 nm. The SU-8 waveguide geometry (nominally 5 µm thickness and 10 µm width) provides large modal overlap with a lensed SMF-28 (spot size typically 2μm), supporting low coupling loss and rapid prototyping on low-cost substrates. The vertical coupling concept was realised both as backside couplers and as topside couplers by introducing a gold reflective layer at the 45° interface to minimise beam divergence and remove free-propagation gaps.

Grayscale laser lithography was used to produce 2.5D mirror slopes and to correct overlay non-uniformity when spinning a second SU-8 layer over pre-defined topography. Atomic force microscopy confirmed well-formed 45° slopes and quantified the effectiveness of proximity error correction. The overlay optimisation reduced excess photoresist height at the mirror–waveguide junction from about 500 nm to below 100 nm. This improvement translated to a significant reduction in measured excess loss for light bypassing the mirror region, from 4.4 dB down to 0.4 dB, indicating that more power is directed onto the vertical coupler. The fabricated devices therefore meet the aims of broadband operation and low loss, while the process flow remains compatible with rapid, low-cost iteration.

Overall, the combination of simulation, fabrication, and profiling shows that SU-8 vertical mirror couplers are a practical route to broadband, low-loss off-chip coupling. The measured reductions in excess loss, together with the confirmed mirror geometry and reflective coating, indicate strong potential for scalable PIC packaging and wafer-level testing. The next chapter presents full optical characterisation to quantify propagation, coupling, and mirror losses across the visible to infrared bands and to benchmark the devices against established coupling schemes.

Bibliography

[1] Chao Xiang, Warren Jin, and John E. Bowers. Silicon nitride passive and active photonic integrated circuits: trends and prospects. *Photonics Research*, 10(6):A82–A96, 2022.

[2] Daniel J. Blumenthal, René Heideman, Douwe Geuzebroek, Arne Leinse, and Chris Roeloffzen. Silicon nitride in silicon photonics. *Proceedings of the IEEE*, 106(12):2209–2231, 2018.

[3] H. Ma, A.K.-Y. Jen, and L.R. Dalton. Polymer-based optical waveguides: Materials, processing, and devices. *Advanced Materials*, 14(19):1339–1365, 2002.

[4] Aydin Yeniay, Renyuan Gao, Kazuya Takayama, Renfeng Gao, and Anthony F. Garito. Ultra-low-loss polymer waveguides. *J. Lightwave Technol.*, 22(1):154, 2004.

[5] Roger Dangel, Jens Hofrichter, Folkert Horst, Daniel Jubin, Antonio La Porta, Norbert Meier, Ibrahim Murat Soganci, Jonas Weiss, and Bert Jan Offrein. Polymer waveguides for electro-optical integration in data centers and high-performance computers. *Opt. Express*, 23(4):4736–4750, 2015.

[6] Kayaku Advanced Materials. SU-8 tf 6000 photoresist, 2025. [Online; accessed 1 March 2025].

[7] Patrick Abgrall, Veronique Conedera, Henri Camon, Anne-Marie Gué, and Nam-Trung Nguyen. SU-8 as a structural material for labs-on-chips and microelectromechanical systems. *Electrophoresis*, 28(24):4539–4551, 2007.

[8] Minh Hang Nguyen, Hai Binh Nguyen, Tuan Hung Nguyen, Xuan Manh Vu, Jain Ren Lai, Fan Gang Tseng, Te Chang Chen, and Ming Chang Lee. SU-8 lenses:

simple methods of fabrication and application in optical interconnection between fiber/LED and microstructures. *Journal of Electronic Materials*, 45(5):2529–2535, 2016.

[9] Yannik Mahlau, Frederik Schubert, Konrad Bethmann, Reinhard Caspary, Antonio Calà Lesina, Marco Munderloh, Jörn Ostermann, and Bodo Rosenhahn. A flexible framework for large-scale FDTD simulations: open-source inverse design for 3D nanostructures. In *Proceedings of SPIE: Photonic and Phononic Properties of Engineered Nanostructures XV*, volume 13377, page 1337709, 2025.

[10] Zuyang Liu and Joyce K. S. Poon. Comparison of lumerical fdtd and tidy3d for three-dimensional fdtd simulations of passive silicon photonic components. *Opt. Continuum*, 4(10):2427–2451, 2025.

[11] Nikolaos Bamiedakis, Fengyuan Shi, Daping Chu, Richard V. Penty, and Ian H. White. High-speed data transmission over flexible multimode polymer waveguides under flexure. *IEEE Photonics Technology Letters*, 30(14):1329–1332, 2018.

[12] Chenlei Li, Dajian Liu, and Daoxin Dai. Multimode silicon photonics. *Nanophotonics*, 8(2):227–247, 2019.

[13] Md Nafiz Amin, Helio Ramollari, Thomas D. Yuzvinsky, Zoe Weber, Tyler J. Adams, Porter B. Dixon, Kevin Bundy, Aaron R. Hawkins, and Holger Schmidt. Multi-mode interference waveguide spectrometer with optimized performance. *Opt. Express*, 32(26):45873–45883, 2024.

[14] Md Nafiz Amin, Vahid Ganjalizadeh, Tyler J. Adams, Porter B. Dixon, Zoe Weber, Matthew DeMartino, Kevin Bundy, Aaron R. Hawkins, and Holger Schmidt. Multimode interference waveguide chip-scale spectrometer (invited). *APL Photonics*, 9(10):100802, 2024.

[15] Ming Zhou. Low-loss polymeric materials for passive waveguide components in fiber optical telecommunication. *Optical Engineering*, 41(7):1631 – 1643, 2002.

[16] Cong Wang, Sung-Jin Cho, and Nam-Young Kim. Su-8-based structural material for microelectronic processing applications. *Materials and Manufacturing Processes*, 28(8):947–952, 2013.

[17] Y. Z. Tang, W. H. Wang, T. Li, and Y. L. Wang. Integrated waveguide turning mirror in SOI. *IEEE Photonics Technology Letters*, 14(1):68–70, 2002.

[18] Yu Zhang, Anirban Samanta, Kuanping Shang, and S. J. Ben Yoo. Scalable 3d silicon photonic electronic integrated circuits and their applications. *IEEE Journal of Selected Topics in Quantum Electronics*, 26(2):1–10, 2020.

[19] Roberta Ramponi, Roberto Osellame, and Marco Marangoni. Two straightforward methods for the measurement of optical losses in planar waveguides. *Review of Scientific Instruments*, 73(3):1117–1120, 2002.

[20] Daniele Melati, Andrea Melloni, and Francesco Morichetti. Real photonic waveguides: guiding light through imperfections. *Adv. Opt. Photon.*, 6(2):156–224, 2014.

[21] Jiawei Li, Chun Cao, Yiwei Qiu, Cuifang Kuang, and Xu Liu. Optical waveguides fabricated via femtosecond direct laser writing: Processes, materials, and devices. *Advanced Materials Technologies*, 8(18):2300620, 2023.

[22] Yang Zhang, Boyan Yu, Zihao Zhang, Xinghao Duan, and Junli Wang. Developments of waveguide lasers by femtosecond laser direct–writing technology. *Photonics*, 11(9):803, 2024.

[23] H. Miyajima and M. Mehregany. High-aspect-ratio photolithography for mems applications. *Journal of Microelectromechanical Systems*, 4(4):220–229, 1995.

[24] B. Loechel, R. Demmeler, M. Rothe, W. Bruenger, S. Fehlberg, and G. Gruetzner. Application of optical lithography for high aspect ratio microstructures. *Journal of Vacuum Science & Technology B: Microelectronics and Nanometer Structures Processing, Measurement, and Phenomena*, 14(6):4179–4183, 1996.

[25] Anya Grushina. Direct-write grayscale lithography. *Advanced Optical Technologies*, 8(3-4):163–169, 2019.

[26] Nils Kolja Wessling, Saptarsi Ghosh, Benoit Guilhabert, Menno Kappers, Alexander M. Hinz, Miles Toon, Rachel A. Oliver, Martin D. Dawson, and Michael J. Strain. Fabrication and transfer printing based integration of free-standing gan membrane micro-lenses onto semiconductor chips. *Opt. Mater. Express*, 12(12):4606–4618, 2022.

[27] Dietrich Meyerhofer. Resolution and proximity effect in optical lithography. In *Proceedings of SPIE: Optical/Laser Microlithography*, volume 922, pages 174–187, 1988.

[28] Allan Gu and Avideh Zakhor. Optical proximity correction with linear regression. *IEEE Transactions on Semiconductor Manufacturing*, 21(2):263–271, 2008.

[29] Y. Zhao, Y. Liu, Z. Wang, L. Wang, L. Li, F. Hou, Z. Song, and Z. Weng. Study of SU-8 photoresist cross-linking process by atomic force acoustic microscopy. *Journal of Microscopy*, 276(3):136–144, 2019.

[30] Stephan Keller, Gabriela Blagoi, Michael Lillemose, Daniel Haefliger, and Anja Boisen. Processing of thin SU-8 films. *Journal of Micromechanics and Microengineering*, 18(12):125020, 2008.

[31] Chin Y. Poon and Bharat Bhushan. Comparison of surface roughness measurements by stylus profiler, AFM and non-contact optical profiler. *Wear*, 190(1):76–88, 1995.

[32] Li Mei and Guangzhao Guan. Profilometry and atomic force microscopy for surface characterization. *Nano TransMed*, 2(1):e9130017, 2023.

[33] James C. Wyant and Katherine Creath. Advances in interferometric optical profiling. *International Journal of Machine Tools and Manufacture*, 32(1):5–10, 1992. Proceedings of the 5th International Conference on Metrology and Properties of Engineering Surfaces.

[34] S. S. Antsyferov, V. G. Maslov, K. E. Rusanov, and K. N. Fazilova. Method of preparation of heterogeneous height standards for measurements by means of interferometry. *Journal of Physics: Conference Series*, 2373(7):072004, 2022.

[35] Z. J. Zheng, Y. Gao, Y. Gui, and M. Zhu. Studying the fine microstructure of the passive film on nanocrystalline 304 stainless steel by eis, xps, and afm. *Journal of Solid State Electrochemistry*, 18:2201–2210, 2014.

[36] Sean P. Bommer, Christopher Panuski, Benoit Guilhabert, Zhongyi Xia, Jack A. Smith, Martin D. Dawson, Dirk Englund, and Michael J. Strain. Transfer printing micro-assembly of silicon photonic crystal cavity arrays: beating the fabrication tolerance limit. *Nature Communications*, 16:60957, 2025.

[37] Benoit Guilhabert, Sean P. Bommer, Nils K. Wessling, Dimitars Jevtics, Jack A. Smith, Zhongyi Xia, Saptarsi Ghosh, Menno Kappers, Ian M. Watson, Rachel A. Oliver, Martin D. Dawson, and Michael J. Strain. Advanced transfer printing with in-situ optical monitoring for the integration of micron-scale devices. *IEEE Journal of Selected Topics in Quantum Electronics*, 29(3):1–11, 2023.

[38] L. Ouattara, M. Knutzen, S. Keller, M.F. Hansen, and A. Boisen. Double layer resist process scheme for metal lift-off with application in inductive heating of microstructures. *Microelectronic Engineering*, 87(5):1226–1228, 2010. The 35th International Conference on Micro- and Nano-Engineering (MNE).

[39] A.K. Sutton and S. Steen. High resolution metal lift-off characterization. *Proceedings of the 15th Biennial University/Government/ Industry Microelectronics Symposium (Cat. No.03CH37488)*, pages 94–98, 2003.

[40] Hua Ke, Shengrong Ye, R. Lloyd Carroll, and Kenneth Showalter. Motion analysis of self-propelled ptsilica particles in hydrogen peroxide solutions. *The Journal of Physical Chemistry A*, 114(17):5462–5467, 2010. PMID: 20387839.

[41] Abu Ali Ibn Sina, Ramanathan Vaidyanathan, Alain Wuethrich, Laura G. Carrascosa, and Matt Trau. Label-free detection of exosomes using a surface plasmon

resonance biosensor. *Analytical and Bioanalytical Chemistry*, 411(7):1311–1318, 2019.

[42] Thearith Ung, Luis M Liz-Marzán, and Paul Mulvaney. Gold nanoparticle thin films. *Colloids and Surfaces A: Physicochemical and Engineering Aspects*, 202(2):119–126, 2002.

[43] P. Gadenne, Y. Yagil, and G. Deutscher. Transmittance and reflectance in situ measurements of semicontinuous gold films during deposition. *Journal of Applied Physics*, 66(7):3019–3025, 1989.

[44] Anna Kossoy, Virginia Merk, Denis Simakov, Kristjan Leosson, Stéphane Kéna-Cohen, and Stefan A. Maier. Optical and structural properties of ultra-thin gold films. *Advanced Optical Materials*, 3(1):71–77, 2015.

[45] Yuli Vladimirsky. 10. lithography. In J.A.R. Samson and D.L. Ederer, editors, *Vacuum Ultraviolet Spectroscopy II*, volume 32 of *Experimental Methods in the Physical Sciences*, pages 205–223. Academic Press, 1998.

[46] Canfield, L.R., Hass, G., and Hunter, W.R. The optical properties of evaporated gold in the vacuum ultraviolet from 300 Å to 2 000 Å. *J. Phys. France*, 25(1-2):124–129, 1964.

[47] Dieter M. Kolb. UV-visible reflectance spectroscopy. In Robert James Gale, editor, *Spectroelectrochemistry: Theory and Practice*, pages 87–188. Springer, Boston, MA, 1988.

Chapter 3

Optical Performance of Waveguides and Mirror Couplers

3.1 Introduction

In this section the optical performance of both the SU8 waveguides and mirror couplers are detailed. As per the simulation results, low-loss transmission of the mirrors are shown to be achievable. The previous simulation results do not include fabrication imperfections or surface roughness effects that can significantly affect device performance. Furthermore, variability in the fabrication facility environmental conditions can lead to geometric variations in the final devices produced. Therefore, it is important to thoroughly investigate and determine losses of devices. This is extremely important for reliability of processing methods to allow for repeatable manufacturing and replication of results. We use five different light sources to characterise the fabricated waveguide and mirror devices for their coupling losses, propagation losses, and finally the excess mirror losses across a broad spectral range. The aim is to have low-loss waveguide mirror devices across the wavelengths of 510 -1630nm with commercially available measurement equipment.

3.2 Optical Bench Setup

3.2.1 End Fire Transmission

The end fire transmission rig is a valuable configuration for injecting and collecting light within the same plane as the waveguides on a photonic substrate [1, 2]. Standard implementations typically utilise SMF-28 lensed fibres, which are designed to focus light to micron scale beam waists for optimal coupling with waveguide facets. The setup for output light collection can vary, ranging from direct fibre coupling to free-space collimation using an objective lens [3, 4].

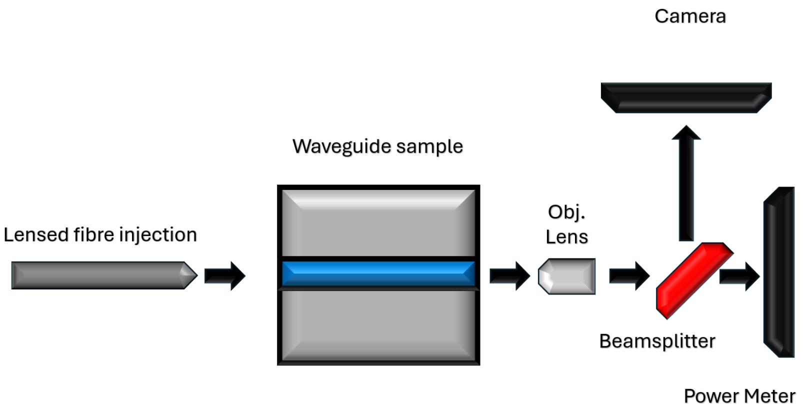

Figure 3.1: End fire transmission setup to characterise the insertion and propagation losses of SU8 waveguides on glass

In our experimental configuration, as shown in fig. 3.1, we used a SMF-28 lensed fibre to couple light in to the SU-8 waveguides. Furthermore, we employed objective lens collimation to facilitate effective alignment with end facet of the waveguides. Within the free space optical setup, a 95:5 beam splitter is used: 5 % of the beam power is reflected onto a camera connected to a PC for visual alignment and monitoring, while the remaining 95 % is transmitted to a power detector connected to an oscilloscope for data acquisition.

3.2.2 Vertical Transmission

The integration of a vertical transmission collection for optical benches is typically not required for characterising photonic integrated circuits, other than grating couplers and LIDAR chips, to name a few [5, 6, 7]. Often, the only vertically optical components consist of boom microscopes that are used by the operator to monitor the chip and help with fibre alignment. However, in our case, we also need to measure power levels in the vertical direction to calculate the excess mirror loss on the device. As with the end fire transmission setup, this can be done in two ways, direct fibre coupling and objective lens collimation. In our case we will use both, but primarily collimation with an objective lens to increase the power collection levels due to the higher angle of acceptance that comes with the objective lens [8, 9]. To show the vertical column setup for characterising the vertical mirror couplers (fig. 3.2), an objective lens is mounted and an L shaped mount that is directly mounted to an xyz translational stage to allow for maximum degrees of freedom of alignment. Directly above the objective lens, is a power meter or an alignment camera.

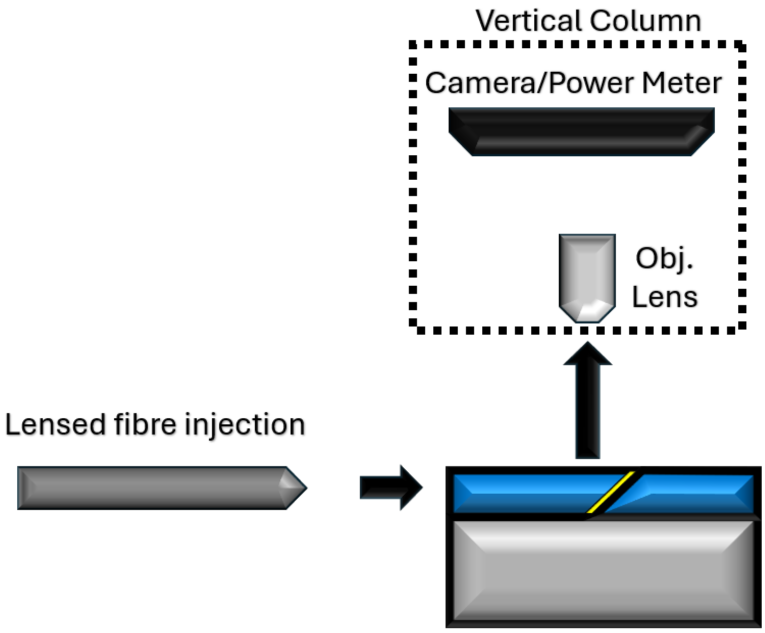

Figure 3.2: Vertical column setup to characterise the vertica mirror couplers

It is important for these pieces of measurement equipment to align the imaged output beam, especially when using InGaAs detectors and cameras due to the smaller footprint of the detection area [10]. By mounting the detection equipped with vertical adjustment, the focal point of the vertical beam can be incident nicely on the detection chip of the device [11, 12].

As discussed previously, direct fibre coupling can also be employed to characterise excess mirror loss. While this approach can be challenging—often requiring custom mounting equipment that may not be ideal for transitioning from research to commercial products, it remains a valuable method. This is particularly relevant for compact photonic integrated circuits (PICs), where compact packaging is also essential [13, 14]. For instance, pluggable transceivers used in data centres and AI hardware commonly rely on direct fibre coupling for input and output light transfer [15, 16].

To evaluate the feasibility of wafer scale testing and potential packaging strategies, we employ a vertically mounted SMF-28 lensed fibre to collect light emitted from the waveguide mirrors [17, 12]. As indicated by simulation results, the expected mirror loss is greater than that observed with free space optics. However, with appropriate mode matching between the waveguide output and the fibre mode, coupling losses below 1 dB are theoretically achievable over a broad wavelength range (fig. 2.6, fig. 2.7) . This performance compares favourably with that of diffraction based Bragg grating couplers, which are commonly used in commercial PICs for fibre to chip coupling.

For experimental implementation, we use 3D printed fibre mounts affixed to an x–y–z translation stage, providing the required degrees of freedom for precise alignment. Device monitoring and alignment are assisted by a boom microscope positioned at an angle relative to the vertical axis.

3.3 Broadband Measurements

3.3.1 Light Sources

To verify broadband spectral operation of the vertical coupling devices, optical tests must be conducted over a large range of wavelengths that are compatible with the SU8 waveguides. In this case, 5 optical sources are selected to cover portions of wavelengths between 510-1630nm. Single wavelength sources cover 510nm and 850nm, while swept sources cover 635-638nm, 1250-1367nm and 1510-1630nm. The two single wavelength sources are ThorLabs fibre coupled laser diodes. The shortest swept wavelength source (635-638nm) is a Newport TLB 6704, with a 110pm free tuning range. The 1250-1360nm source is a HP Fabry Perot step tunable laser. Finally, for the longest wavelengths (1510-1630nm), is a HP 81602A swept laser source. All sources are coupled into SMF-28, provided by OZ optics with lensed fibre tips with specifications: 4μm core, 125μm cladding and a spot diameter of 2.0μm ±0.5μm.

3.3.2 Waveguide Coupling and Propagation Losses

The fabricated chip design incorporates all the individual optical devices needed to characterise the 5x10μm^2 SU8 waveguides. The facet losses are the losses induced from fibre to waveguide coupling and the propagation losses are the losses induced per unit length of the waveguides.

The waveguide facets have an area of approximately 50μm$^{\mathbf{2}}$, which results in a high modal overlap with the lensed fibre mode. This efficient mode matching minimises coupling losses at the waveguide facets [18, 19].

To quantify the facet losses across all light sources used, reference power measurements are first taken directly from the lensed fibre using a free space optical setup. Subsequently, the same measurement is performed with the light coupled into and out of the waveguide device, which has a total length of 8mm. Optimal alignment ensures efficient coupling into the waveguide. Comparing the reference and transmitted powers allows the extraction of total insertion losses, from which facet losses can be inferred.

The device design includes waveguide cutbacks used to determine the propagation losses [20, 21, 22]. The sets of cutbacks increase the waveguide length by 1cm over 6 sets of cutbacks in increments of approximately 1.5mm. With reference power levels for a straight 8mm waveguide, numerous power level measurements are taken for each cutback using the same end fire transmission setup, detailed in fig 3.1. Measurements for the optical power as the waveguide length increases are taken and plotted as a function of transmission against the increase in waveguide length. Fitting a line of best fit through the data gives the propagation losses. For example, the propagation losses at 635nm are 2.09 dB/cm, given by the slope illustrated in fig. 3.3.

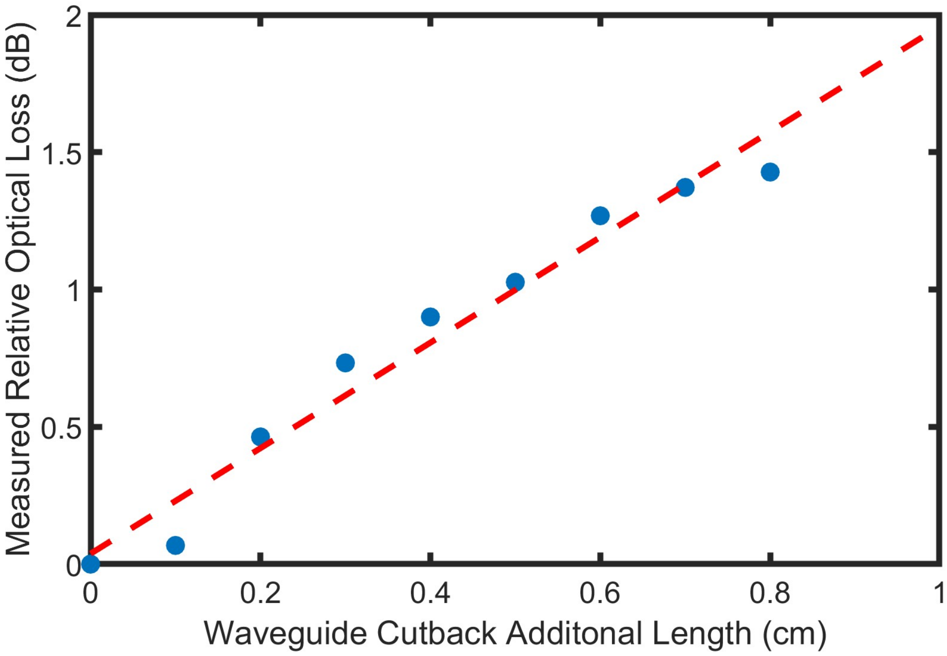

Figure 3.3: Propagation losses of SU-8 waveguides at a wavelength of 635nm

The total loss of a waveguide can be represented as:

$$\beta = 2\alpha_{\text{coupling}} + \alpha L \tag{3.1}$$

Where, β is the total loss of the waveguide (dB), L is the length of the waveguide (typically cm) and α is the propagation losses (dB/cm). With the propagation measurement from the cutbacks, we use the reference waveguide transmission to work back and solve for the coupling losses:

$$\alpha_{\text{coupling}} = \frac{\beta - \alpha L}{2} \tag{3.2}$$

This gives coupling losses in the range 0.4-0.5 dB at each facet, from using the propagation losses in table 3.1. This methodology was used due to the often low output power received through the cutbacks, rather than having an absolute power measurement which leads to the y-intercept being the facet coupling loss.

Wavelength (nm)	Propagation Loss (dB/cm)	Pre mirror loss (dB)
516	2.21	0.88
635	2.09	0.84
850	1.87	0.75
1250	1.66	0.66
1550	1.56	0.62

Table 3.1: Measured propagation losses of SU8 using the cutback method across various wavelengths and estimated losses before mirror structure

The propagation losses shown in table 3.1 are for the multi modal waveguides. Comparing this to a case where for each wavelength, the waveguide is designed to be single mode - Rayleigh scattering dominates the loss mechanism, i.e. shorter wavelengths result in higher losses. Whereas in our multi modal case, multiple loss mechanisms influence the final result.

3.3.3 Excess Mirror Loss

As described in the previous section, the waveguide propagation and coupling losses were calculated. In this section, the focus is to use the information on a device that has a waveguide mirror vertical coupler device to determining the excess loss induced from the reflected beam [23, 24, 25]. The setup used is the same as the end fire setup illustrated in fig. 3.2, while the power detectors and cameras are switched out for the relevant wavelengths across the sweep in order to assist with alignment and power level measurements. Before power measurements are taken, the camera is used to align the vertical beam produced by the mirror, as illustrated with images taken in fig 3.4

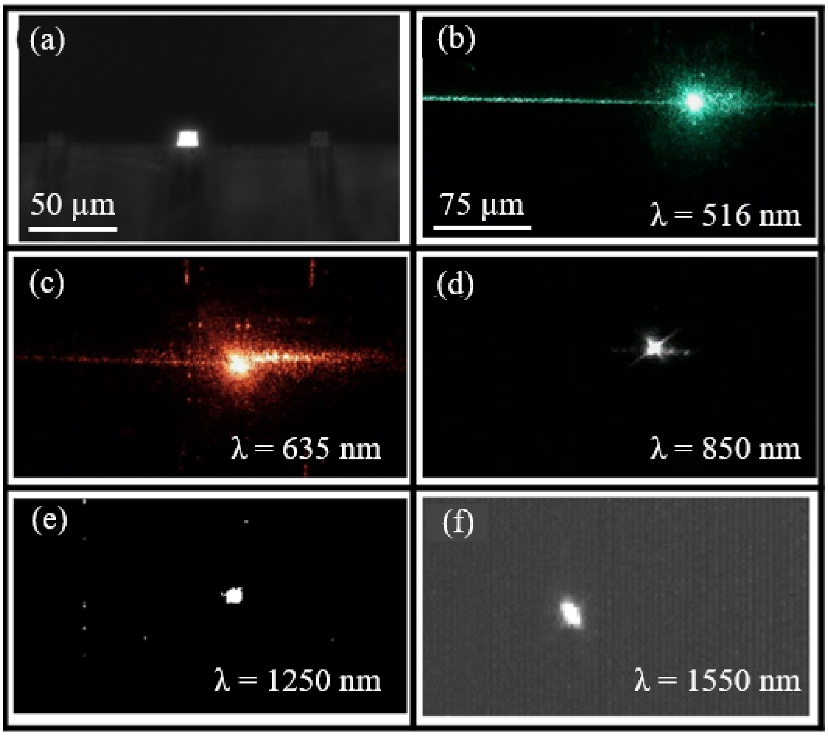

Figure 3.4: (a) facet image of waveguide with top side mirror injection. (b-f) microscope images of mirror outputs from waveguide mirrors with injection from the waveguide facet

Fig. 3.4a differs from 3.4(b-f), with fig. 3.4a showing a waveguide facet image from light directly coupled from a μ LED projector [26, 27, 28].

As mentioned during the waveguide mirror overlay section, during the fabrication process, further grayscale optimisation was used to reduce the amount of excess resist overlapping the waveguide mirror region. The experimental optical loss changes from 4.4 dB to as low as 0.4 dB for light that is propagated towards the end facet, instead of being reflected by the mirror. The mirrors are located at the centre of design (4mm from facet), meaning the the pre-mirror loss of the system can be defined as:

$$\text{Pre-mirror loss (dB)} = \text{Facet loss (dB)} + \frac{\alpha L}{2} \tag{3.3}$$

Furthermore, with the known facet coupling losses, deduced from the propagation losses in table 3.1, and the measurements of the vertical light collimated by an objective lens with NA=0.8 and estimated losses of 0.2 dB [29]. Therefore, by using the following

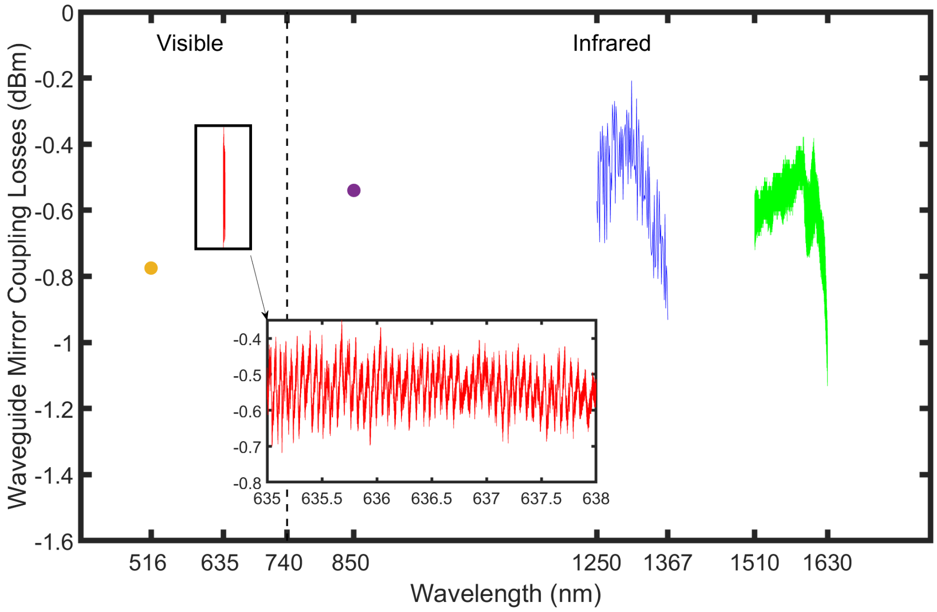

Figure 3.5: Spectra of transmission from waveguide mirror at wavelengths 516-1630nm

formula:

$$\text{Mirror loss (dB)} = \text{Transmission (dB)} - \text{Objective loss (dB)} - \text{Pre-mirror loss (dB)} \tag{3.4}$$

where the transmission is given in dB. The results are shown in fig 3.5.

With waveguide mirror coupling losses below 1 dB across the measured waveguide spectrum, we have successfully shown that performance of low loss waveguide mirror vertical couplers. The Fabry–Perot fringes observed in the measurements arise from interference effects within the optical cavity formed by the partially reflective waveguide facets [30, 31, 32, 33, 34]. Light reflected back and forth between the input and output facets can interfere either constructively or destructively, depending on the wavelength and cavity length. This interference modulates the transmitted power, resulting in oscillations in the vertical axis of the measured spectrum. A further source of interference arises from transition between mediums, i.e. SU8 to air and air to objective lens.

As the operating wavelength increases from shorter values up to 1630nm, the waveguide transitions from being highly multimode to supporting a maximum of approximately four modes. This reduction in the number of guided modes introduces various loss mechanisms [35, 36, 37]. In the multimode regime, the broad angular spread of modes incident on the reflective surface can result in significant scattering, increased back reflection into the cavity, and substantial mode mismatch in the vertical direction [38, 39, 40, 41]. As the wavelength increases and the number of supported modes decreases, these angular effects become less pronounced, contributing to an observed increase in transmission efficiency at longer wavelengths [42, 43, 44]. Nonetheless, even at 1630nm, angular variation of the modes incident on the mirror continues to induce losses. Additionally, surface roughness of the reflective interface can further contribute to scattering and reduce overall transmission [45]. Finally, with the facet losses, these losses are a single wavelength for the swept sources as indicated in table 3.1. As the source shifts from these wavelengths then the facet coupling is no longer optimised and hence effect the final results for the excess mirror loss.

From simulations we can see there is still room for improvement and the limiting factor in this is the equipment and quality control of the fabrication process. To decrease the mirror loss further, the investigation in to the origin of the excess loss can be investigated and nullified. Furthermore, higher quality tools and quality checks on aged resist can be carried out to ensure optimised devices which can open up a whole new level of potential for this regime as a coupling method for commercial PICs.

3.4 Fibre Collection

3.4.1 Experimental Setup

The experimental setup for direct coupling from waveguide mirror to lensed fibre, is similar to some commercial PIC packages that use fibres and grating coupling devices [46, 47, 48]. To achieve maximum coupling transmission, the fibre has to be mounted directly above the waveguide mirror output, ideally, with the fibre tip within the working distance of the fibre lens to allow for mode matching (focused on Gaussian beam waist of output beam). As shown in fig. 3.5, an image of the lens fibre injection to waveguide and direct vertical collection with a lens fibre from the mirror is setup using a custom mounted fibre device.

3.4.2 Direct Fibre Coupling Losses

While free space optical measurements are effective for characterising optical losses, practical, packageable, and wafer scale photonic integrated circuits (PICs) predominantly rely on direct fibre coupling to interface with external systems. As such, it is critically important to evaluate the coupling efficiency between the waveguide mirror structures and standard SMF-28 fibres [13, 14, 46, 47, 48].

To this end, a custom vertical coupling rig was developed using 3D printing technology. The fibre mount was secured to an xyz translational stage, allowing precise control over positioning. An SMF-28 lensed fibre was vertically mounted (fig. 3.6), and its output was connected to an InGaAs detector optimised for measurements at 1550 nm, where the waveguides operate at close to single mode. The same swept wavelength source used for the free-space measurements was employed for consistency in comparison.

For visual alignment and monitoring, a boom microscope camera was angled to observe the fibre tip from above. Additionally, an end fire microscope camera was custom fitted to another xyz translational stage, providing sufficient vertical travel range while preventing unintentional contact between the fibre and the sample surface.

To facilitate the alignment of the vertical fibre, a modulated signal was applied to the 1550 nm laser source. This modulation produced a discernible signal variation on the oscilloscope, allowing real time feedback during the alignment process [49], an example of the detected modulated signal on the oscilloscope is shown in fig 3.7.

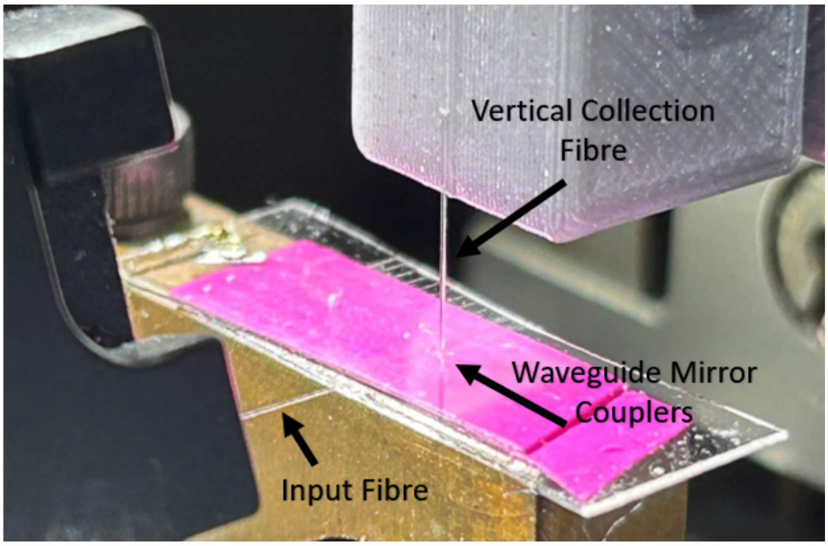

Figure 3.6: Image of the captured modulated laser signal, directly coupled from mirror to SMF-28 lens fibre

Once optimal coupling was achieved, output power readings were recorded over multiple waveguide mirror devices to ensure repeatability. To evaluate wafer scale performance [50, 51, 52], measurements were conducted across multiple devices and chips.

Using the same data processing methodology as applied in the free space coupling loss analysis, the coupling loss between the waveguide mirror and the vertically mounted fibre was determined. While the loss mechanism is conceptually similar to that of edge coupling between fibre and waveguide facet, key differences arise due to the vertical propagation geometry and the differing numerical apertures of the systems involved [53, 54].

The measured coupling loss between the fibre and mirror was found to be 0.8 dB, slightly higher than that observed in the vertical free-space setup. This discrepancy can be attributed to alignment limitations, particularly in the z axis. The minimum travel range of the translation stage posed a risk of the fibre tip colliding with the sample, likely preventing optimal z-axis positioning. Moreover, the free-space configuration benefitted from a high numerical aperture (NA) objective lens, which afforded greater angular tolerance and higher collection efficiency.

Despite this, achieving a sub-1 dB coupling loss via direct fibre coupling demonstrates the feasibility of the mirror-based vertical coupler for wafer-scale testing and packaging integration in compact PIC platforms.

3.5 Summary

In this chapter, the optical performance of SU-8 waveguides and integrated mirror couplers has been presented, from design and fabrication through to broadband experimental characterisation. Using both end-fire and vertical transmission measurement setups, propagation and coupling losses were quantified across a wide spectral range of 510–1630 nm. Waveguide propagation losses were found to be wavelength-dependent but remained low, with facet coupling losses in the range of 0.4–0.5 dB, confirming effective mode matching between the lensed fibre and SU-8 waveguides.

The fabricated vertical mirror couplers demonstrated excess mirror losses below 1 dB across the full measurement range when characterised with free-space collection. These results align closely with simulations and highlight the effectiveness of grayscale lithography in producing 45° mirror facets with reduced resist height, significantly lowering scattering-induced loss. Direct fibre collection experiments further validated the practicality of the devices for packaging applications, with measured coupling losses of 0.8 dB, confirming their compatibility with wafer-scale testing and fibre-based integration.

Overall, the characterisation results show that SU-8 waveguide mirror couplers can deliver broadband, low-loss performance suitable for compact and scalable photonic integrated circuits. While further optimisation in fabrication quality control could reduce residual excess losses, the demonstrated performance already places these devices as a promising alternative to conventional grating couplers, offering both wide spectral coverage and high coupling efficiency.

Bibliography

[1] Thomas F. Krauss and Richard M. De La Rue. Optical characterization of waveguide-based photonic microstructures. *Applied Physics Letters*, 68(12):1613–1615, 1996.

[2] Michael Gehl, Nicholas Boynton, Christina Dallo, Andrew Pomerene, Andrew Starbuck, Dana Hood, Douglas C. Trotter, Anthony Lentine, and Christopher T. DeRose. Accurate photonic waveguide characterization using an arrayed waveguide structure. *Opt. Express*, 26(14):18082–18095, 2018.

[3] A. Piruska, A. A. S. Bhagat, K. Zhou, E.T.K. Peterson, I. Papautsky, and C. J. Seliskar. Characterization of SU-8 optical multimode waveguides for integrated optics and sensing on microchip devices. *Microfluidics, BioMEMS, and Medical Microsystems IV*, 6112:611207, 2006.

[4] Jhonattan C. Ramirez, Juliana N. Schianti, Maria G. Almeida, Aristides Pavani, Roberto R. Panepucci, Hugo E. Hernandez-Figueroa, and Lucas H. Gabrielli. Low-loss modified su-8 waveguides by direct laser writing at 405 nm. *Opt. Mater. Express*, 7(7):2651–2659, 2017.

[5] Dirk Taillaert, Frederik Van Laere, Melanie Ayre, Wim Bogaerts, Dries Van Thourhout, Peter Bienstman, and Roel Baets. Grating couplers for coupling between optical fibers and nanophotonic waveguides. *Japanese Journal of Applied Physics*, 45(8R):6071, 2006.

[6] R. Ulrich. Efficiency of optical-grating couplers. *J. Opt. Soc. Am.*, 63(11):1419–1431, 1973.

[7] G. Roelkens, D. Vermeulen, D. Van Thourhout, R. Baets, S. Brision, P. Lyan, P. Gautier, and J.-M. Fédéli. High efficiency diffractive grating couplers for interfacing a single mode optical fiber with a nanophotonic SOI waveguide circuit. *Applied Physics Letters*, 92(13):131101, 2008.

[8] Carsten Robens, Stefan Brakhane, Wolfgang Alt, Felix Kleißler, Dieter Meschede, Geol Moon, Gautam Ramola, and Andrea Alberti. High numerical aperture (NA = 0.92) objective lens for imaging and addressing of cold atoms. *Optics Letters*, 42(6):1043–1046, 2017.

[9] Wanfu Shen, Chunguang Hu, Shuai Li, and Xiaotang Hu. Using high numerical aperture objective lens in micro-reflectance difference spectrometer. *Applied Surface Science*, 421:535–541, 2017. 7th International Conference on Spectroscopic Ellipsometry.

[10] F.E. Ejeckam, C.L. Chua, Z.H. Zhu, and Y.H. Lo. High-performance ingaas photodetectors on si and gaas substrates. *Proceedings IEEE/Cornell Conference on Advanced Concepts in High Speed Semiconductor Devices and Circuits*, pages 194–200, 1995.

[11] Guomin Jiang, Sarfaraz Baig, and Michael R. Wang. Flexible polymer waveguides with integrated mirrors fabricated by soft lithography for optical interconnection. *J. Lightwave Technol.*, 31(11):1835–1841, 2013.

[12] W.-H. Juan and S.W. Pang. High-aspect-ratio si vertical micromirror arrays for optical switching. *Journal of Microelectromechanical Systems*, 7(2):207–213, 1998.

[13] Lee Carroll, Jun-Su Lee, Carmelo Scarcella, Kamil Gradkowski, Matthieu Duperron, Huihui Lu, Yan Zhao, Cormac Eason, Padraic Morrissey, Marc Rensing, Sean Collins, How Yuan Hwang, and Peter O'Brien. Photonic packaging: Transforming silicon photonic integrated circuits into photonic devices. *Applied Sciences*, 6(12), 2016.

[14] Wim Bogaerts, Daniel Pérez, José Capmany, David A. B. Miller, Joyce Poon, Dirk Englund, Francesco Morichetti, and Andrea Melloni. Programmable photonic circuits. *Nature*, 586:207–216, 2020.

[15] Erman Timurdogan, Zhan Su, Ren-Jye Shiue, Matthew J. Byrd, Christopher V. Poulton, Kenneth Jabon, Christopher DeRose, Benjamin R. Moss, Ehsan S. Hosseini, Ivan Duzevik, Michael Whitson, Ronald P. Millman, Dogan A. Atlas, and Michael R. Watts. 400g silicon photonics integrated circuit transceiver chipsets for cpo, obo, and pluggable modules. *Optical Fiber Communication Conference (OFC) 2020*, page T3H.2, 2020.

[16] Brandon J. Isaac, Bowen Song, Sergio Pinna, Larry A. Coldren, and Jonathan Klamkin. Indium phosphide photonic integrated circuit transceiver for fmcw lidar. *IEEE Journal of Selected Topics in Quantum Electronics*, 25(6):1–7, 2019.

[17] Satoshi Maekawa, Kouichi Nitta, and Osamu Matoba. Transmissive optical imaging device with micromirror array. In *Proceedings of SPIE: Three-Dimensional TV, Video, and Display V*, volume 6392, page 63920E, 2006.

[18] Yi-Ming Chen, Cheng-Lin Yang, Yao-Ling Cheng, Hsiu-Hsiang Chen, Ying-Chih Chen, Yen Chu, and Tsung-Eong Hsieh. 10gbps multi-mode waveguide for optical interconnect. *Proceedings Electronic Components and Technology, 2005. ECTC '05.*, pages 1739–1743 Vol. 2, 2005.

[19] Anthony S. Holland, Arnan Mitchell, Vishal S. Balkunje, Mike W. Austin, and Mukund K. Raghunathan. Fabrication of raised and inverted SU8 polymer waveguides. *Optoelectronic Devices and Integration*, 5644:353 – 366, 2005.

[20] R. Kappeler, P. Kaspar, and H. Jäckel. Propagation loss computation of w1 photonic crystal waveguides using the cutback technique with the 3d-fdtd method. *Photonics and Nanostructures - Fundamentals and Applications*, 9(3):235–247, 2011.

[21] Francesco Dell'Olio, Samuel M. Hörmann, Teresa Natale, Roel Baets, and Alexander Bergmann. Numerical and experimental methods for estimating the propaga-

tion loss in microphotonic waveguides. *Advanced Photonics Research*, page 2500103, 2025.

[22] G. T. Reed. Methods of measurement of passive integrated optical waveguides. In *IEE Colloquium on Measurements on Optical Devices*, pages 2/1–2/7, 1992.

[23] D.I. Babic, Y. Chung, N. Dagli, and J.E. Bowers. Modal reflection of quarter-wave mirrors in vertical-cavity lasers. *IEEE Journal of Quantum Electronics*, 29(6):1950–1962, 1993.

[24] Yasutomo Johraku and Yasuo Kokubun. Low loss vertical optical path conversion using 45° mirror for coupling between optical waveguide devices and planar devices. *Japanese Journal of Applied Physics*, 47(8S1):6744, 2008.

[25] Shaoliang Yu, Luigi Ranno, Qingyang Du, Samuel Serna, Colin McDonough, Nicholas Fahrenkopf, Tian Gu, and Juejun Hu. Free-form micro-optics enabling ultra-broadband low-loss off-chip coupling. *Laser & Photonics Reviews*, 17:202200025, 2023.

[26] Zhongyi Xia, Dimitars Jevtics, Benoit Jack Eloi Guilhabert, Jonathan J. D. McKendry, Qian Gao, Hark Hoe Tan, Chennupati Jagadish, Martin D. Dawson, and Michael John Strain. Modulation of nanowire emitter arrays using micro-led technology. *ACS Nano*, 19(16):15813–15819, 2025. PMID: 40241407.

[27] G. E. Johnstone, J. Gray, S. Bennett, S. D. Johnson, C. F. Higham, F. Dehkhoda, E. Xie, J. Herrnsdorf, P. Murray, M. J. Padgett, R. Murray-Smith, R. K. Henderson, M. D. Dawson, and M. J. Strain. High speed single pixel imaging using a microLED-on-CMOS light projector. *Optics Express*, 32(14):24615–24628, 2024.

[28] Alexander D. Griffiths, Johannes Herrnsdorf, Michael J. Strain, and Martin D. Dawson. Scalable visible light communications with a micro-led array projector and high-speed smartphone camera. *Opt. Express*, 27(11):15585–15594, 2019.

[29] P. Kruit and H. Shuman. The influence of objective lens aberrations in energy-loss spectrometry. *Ultramicroscopy*, 17(3):263–267, 1985.

[30] Naichia Yeh. Analysis of spectrum distribution and optical losses under fresnel lenses. *Renewable and Sustainable Energy Reviews*, 14(9):2926–2935, 2010.

[31] Sareh Taebi, Mohammadreza Khorasaninejad, and Simarjeet Singh Saini. Modified fabry-perot interferometric method for waveguide loss measurement. *Appl. Opt.*, 47(35):6625–6630, 2008.

[32] T. Feuchter and C. Thirstrup. High precision planar waveguide propagation loss measurement technique using a fabry-perot cavity. *IEEE Photonics Technology Letters*, 6(10):1244–1247, 1994.

[33] B. Lombardet, R. Ferrini, L. A. Dunbar, R. Houdré, C. Cuisin, O. Drisse, F. Lelarge, F. Pommereau, F. Poingt, and G.-H. Duan. Propagation loss measurements and fabry–pérot mode analysis using out-of-plane light scattering in photonic crystal waveguides. *Applied Physics Letters*, 86(11):111111, 2005.

[34] Yiming He, Dan Lu, and Lingjuan Zhao. Reflection airy distribution of a fabry-pérot resonator and its application in waveguide loss measurement. *Opt. Express*, 27(13):17876–17886, 2019.

[35] Alfredo De Rossi, Valentin Ortiz, Michel Calligaro, Loïc Lanco, Sara Ducci, Vincent Berger, and Isabelle Sagnes. Measuring propagation loss in a multimode semiconductor waveguide. *Journal of Applied Physics*, 97(7):073105, 2005.

[36] Shuai Cui, Yuan Yu, Kaixiang Cao, Zhao Pan, Xiaoyan Gao, and Xinliang Zhang. Integrated waveguide coupled ultralow-loss multimode waveguides based on silicon nitride resonators. *Opt. Express*, 32(2):2179–2187, 2024.

[37] Bin Ni, Hao Xu, Chenyang Luo, Shengbao Wu, and Jichuan Xiong. Low-loss and broadband silicon-based multimode waveguide crossing at 2 µm using 2-D subwavelength holey metamaterials. *Optics Express*, 33(4):6788–6798, 2025.

[38] J. A. Mores, G. N. Malheiros-Silveira, H. L. Fragnito, and H. E. Hernández-Figueroa. Efficient calculation of higher-order optical waveguide dispersion. *Optics Express*, 18(19):19522–19531, 2010.

[39] Ying Shi, Lin Ma, Yudi Zhuang, and Zuyuan He. Investigation on roughness-induced scattering loss of small-core polymer waveguides for single-mode optical interconnect applications. *Optics Express*, 28(26):38733–38744, 2020.

[40] Sangsik Kim, Daron A. Westly, Brian J. Roxworthy, Qing Li, Alexander Yulaev, Kartik Srinivasan, and Vladimir A. Aksyuk. Photonic waveguide to free-space gaussian beam extreme mode converter. *Light: Science & Applications*, 7:73, 2018.

[41] Quandong Huang, Kin Seng Chiang, and Wei Jin. Thermo-optically controlled vertical waveguide directional couplers for mode-selective switching. *IEEE Photonics Journal*, 10(6):1–14, 2018.

[42] Steven Spector, Michael W. Geis, Donna Lennon, Richard C. Williamson, and Theodore M. Lyszczarz. Hybrid multi-mode/single-mode waveguides for low loss. In *Optical Amplifiers and Their Applications / Integrated Photonics Research*, page IThE5, 2004.

[43] E. Murphy and T. Rice. Low-loss coupling of multiple fiber arrays to single-mode waveguides. *Journal of Lightwave Technology*, 1(3):479–482, 1983.

[44] Firehun Dullo, Jean-Claude Tinguely, Stian Solbø, and Olav Hellesø. Single-mode limit and bending losses for shallow rib $\mathrm{Si_3N_4}$ waveguides. *IEEE Photonics Journal*, 7:7800107, 2015.

[45] Dmitry I. Yakubovsky, Aleksey V. Arsenin, Yury V. Stebunov, Dmitry Yu. Fedyanin, and Valentyn S. Volkov. Optical constants and structural properties of thin gold films. *Opt. Express*, 25(21):25574–25587, 2017.

[46] W. Bogaerts, D. Taillaert, B. Luyssaert, P. Dumon, J. Van Campenhout, P. Bienstman, D. Van Thourhout, R. Baets, V. Wiaux, and S. Beckx. Basic structures for photonic integrated circuits in silicon-on-insulator. *Opt. Express*, 12(8):1583–1591, 2004.

[47] Ming Dai, Leilei Ma, Yelong Xu, Minghui Lu, Xiaoping Liu, and Yanfeng Chen. Highly efficient and perfectly vertical chip-to-fiber dual-layer grating coupler. *Optics Express*, 23(2):1691–1698, 2015.

[48] Shiang Yu Huang and Stefanie Barz. Compact inverse designed vertical coupler with bottom reflector for sub-decibel fiber-to-chip coupling on SOI platform. *Scientific Reports*, 15:86161, 2025.

[49] Marco Carminati, Stefano Grillanda, Pietro Ciccarella, Giorgio Ferrari, Michael Strain, Marco Sampietro, Andrea Melloni, and Francesco Morichetti. Fiber-to-waveguide alignment assisted by a transparent integrated light monitor. *IEEE Photonics Technology Letters*, 27:157–160, 2014.

[50] Daniel Schmid, René Eisermann, Anna Peczek, Georg Winzer, Lars Zimmermann, and Stephan Krenek. Wafer-scale experimental determination of coupling and loss for photonic integrated circuit design optimisation. *Photonics*, 12(3):234, 2025.

[51] Abdullah J. Zakariya, Tao Liu, Julien G. Noel, and Roberto R. Panepucci. Flexible waveguide coupling probe for wafer-level optical characterization of planar lightwave circuits. In *Proceedings of the SBMO/IEEE MTT-S International Microwave and Optoelectronics Conference (IMOC)*, pages 458–461, 2007.

[52] Ramgopal Venkateswaran, Jay W. Reddy, and Maysamreza Chamanzar. A semi-automated system for wafer-scale optical waveguide characterization. In *Proceedings of the 43rd Annual International Conference of the IEEE Engineering in Medicine & Biology Society (EMBC)*, pages 7502–7505, 2021.

[53] Fang Zhang, Chuanlu Dend, Yi Huang, Qi Zhang, Xiaobei Zhang, and Tingyun Wang. Optimization of vertical coupling induced by 45° micro-mirrors in double-layer polymer optical waveguides with co2 laser smoothing. *Opt. Express*, 32(21):36298–36314, 2024.

[54] Lvyi Zhong, Maoqing Guo, Shilong Li, Yuhang Chen, Jie Li, Jitao Li, and Dingyu Yang. Progress of grating couplers for light exchange between space and on-chip. *Advanced Optical Materials*, page e01171, 2025.

Chapter 4

Advanced Devices and Light Source Integration

4.1 Introduction

Integrating active photonic sources such as LEDs and VCSELs is central to reducing form factor in PICs and eliminating bulky free-space optics [1, 2, 3, 4, 5, 6]. Building on the low-loss, broadband vertical coupling techniques developed earlier, this chapter investigates and integrates active devices with SU-8 waveguide-to-vertical-mode couplers. We demonstrate receiver structures and electrical interconnects for 850 nm VCSEL arrays and 416 nm μLEDs, targeting a low-cost, rapid-prototype route to active–passive optoelectronic chips.

4.2 VCSEL Integration

4.2.1 Waveguide Mirror Receiver Devices

To scale the number of functional waveguide mirror devices on a single substrate, mirror arrays with a pitch of 590 µm × 590 µm were designed and fabricated. This pitch balances optical isolation with manufacturability, enabling dense integration across the chip. As illustrated in Fig. 4.1, microscope images confirm successful fabrication of the array.

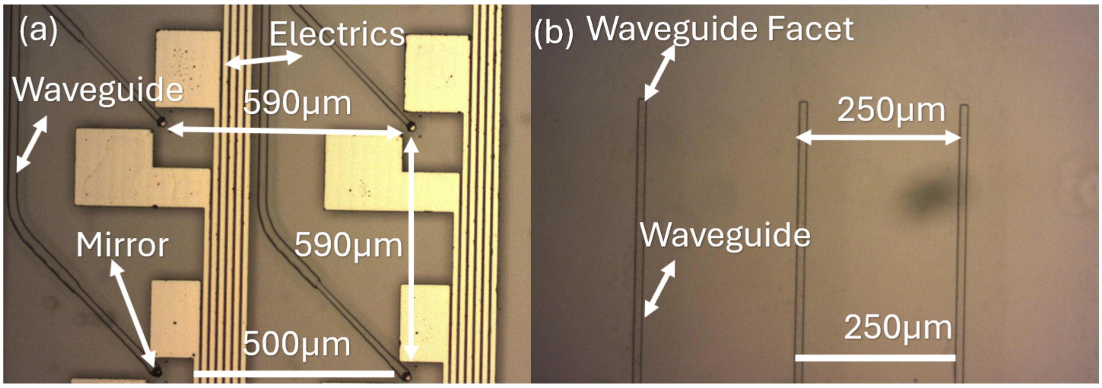

Figure 4.1: (a) Array of SU8 waveguide mirror devices with integrated electrical connections. (b) Cleaved end-facet array prepared for fibre or free-space collection.

Fig. 4.1a shows the fabricated mirror array with electrical interconnects, while Fig. 4.1b shows the waveguide facet array that can be cleaved for subsequent optical collection.

A dual-layer device architecture was implemented, combining optical mirror structures with an overlaid electrical interface. Patterned metal deposition windows extend from probing contact pads to landing sites for each VCSEL emitter, with conductive ink deposited onto the landing pads for integration. The routing design is illustrated in Fig. 4.2.

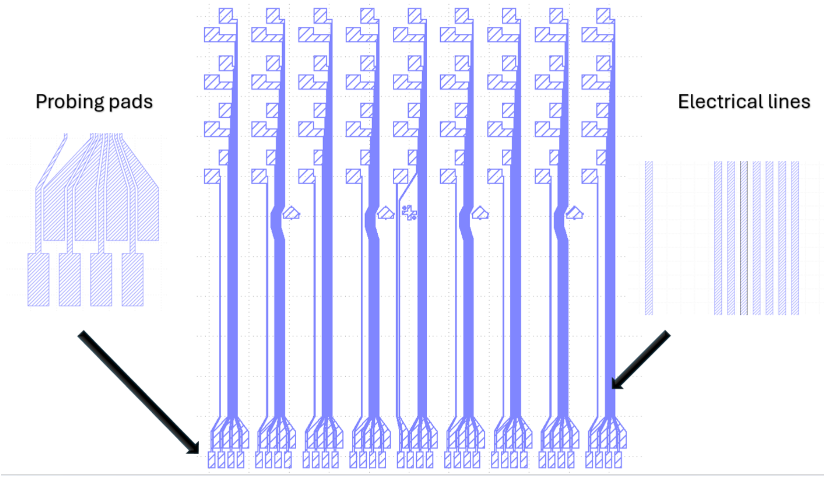

Figure 4.2: GDS layout of electrical contact lines, pads, and probing points for VCSEL integration.

This configuration provides individual electrical addressability across the 4 × 9 VC-

SEL array (36 channels), enabling full parallel control during experimental validation.

To realise these interconnects, a bilayer metallisation scheme was employed: a 50 nm titanium (Ti) adhesion layer followed by 500 nm of gold (Au), deposited by electron-beam evaporation. The increased gold thickness relative to the optical mirror coatings minimises the risk of delamination and ensures low-resistance electrical paths, even under repeated probing or thermal stress [7, 8]. By contrast, thinner reflective layers suffice for the optical mirrors, enabling a streamlined single-step deposition for prototyping.

Large-area arrays introduce challenges in uniform resist coating. Variations in spin thickness, substrate tilt, or particulates can shift the laser focal plane during lithography, producing non-uniform geometries [9, 10]. Such imperfections degrade waveguide confinement and increase scattering losses [11, 12, 13, 14, 15]. To mitigate this, substrate cleaning, dehydration baking, optimised spin protocols, and profilometry checks were employed. The overall fabrication sequence is summarised in Table 4.1.

Step number	**Process**
1	45° SU8 structure
2	Metal openings for mirrors, electronic interconnects
3	Metal deposition and lift off
4	Waveguide overlay with mirrors
5	Facet cleave

Table 4.1: Fabrication flow for scaling waveguide mirror devices to electronic integration

The final arrays were characterised via end-facet injection, using the same setup as in earlier loss measurements. Fig. 4.3 shows stitched microscope images of turning mirrors emitting at 635 nm under single-fibre injection.

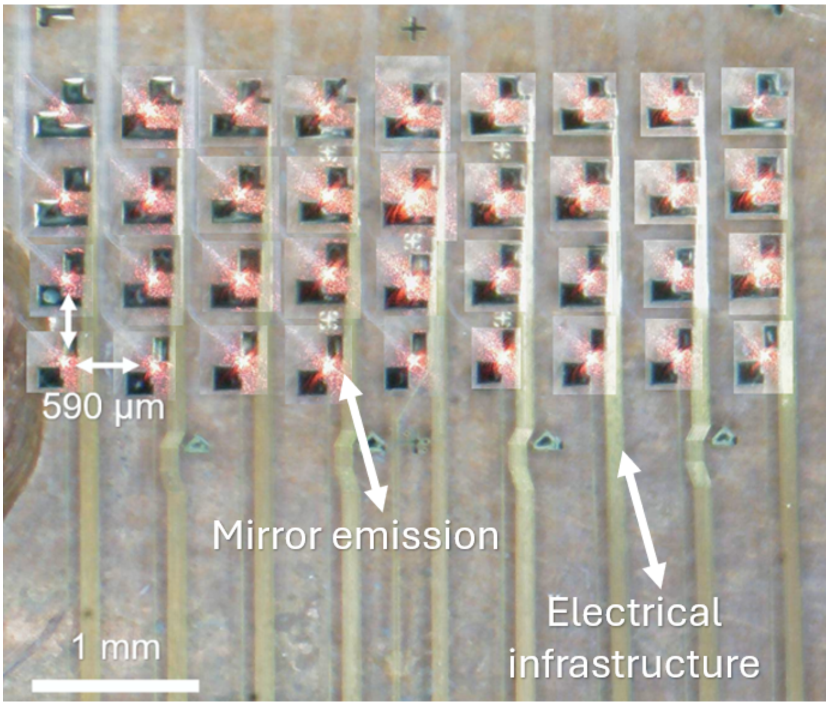

Figure 4.3: Stitched microscope images of vertical emission from individual waveguide mirrors at $\lambda = 635$ nm. Electrical contacts visible on the device enable testing prior to full integration.

Despite functional operation, the observed losses in this final integrated array were significantly higher than those measured in earlier (> 1dB), low-loss reference devices. This increase in loss can be attributed to several factors. Firstly, fabrication imperfections play a critical role, particularly those introduced during the laser lithography process. In densely packed regions of the design [16], specifically, where metal conductive tracks run in close proximity to the waveguides, the exposure dose increases due to proximity effects. This results in waveguides with overexposed cross sections, leading to increased optical scattering, reduced confinement, and degraded modal quality [17]. In some fabrication runs, the overexposed regions and non-uniformity in the waveguide structure are apparent. For example, fig. 4.4 residual photoresist is apparent in areas where overexposure has taken place, while waveguides can also be deformed as indicated which while change the mode properties and confinement

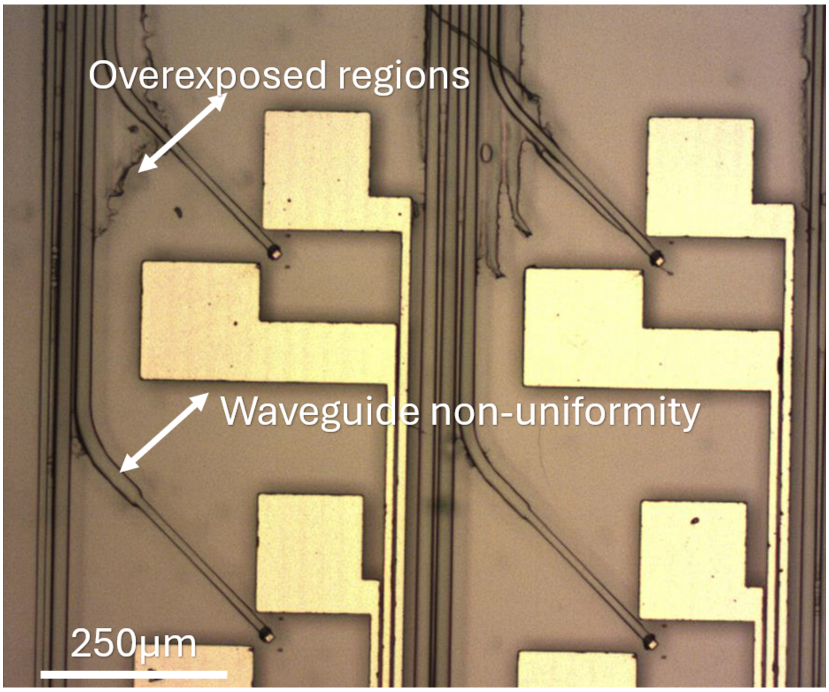

Figure 4.4: Overexposed and waveguide structure issues due to fabrication imperfections caused by metal tracks

Moreover, the routing of the waveguides in this array necessitates multiple bends and parallel sections, which introduces additional complexity. Overexposure in these regions can induce lateral mode leakage and evanescent coupling between adjacent waveguides [18, 19]. Such parasitic coupling is particularly detrimental in closely spaced routing sections, where the mode field may partially extend into neighbouring guides, resulting in crosstalk and mode distortion. These effects are exacerbated by the non-uniformity in exposure caused by focal drift and laser defocusing as the writing system scans across the substrate, which further degrades the reproducibility and fidelity of the waveguide profiles.

4.2.2 Integration Method

To form the electrical interconnects, conductive ink was dispensed using a Voltera direct-write system. The Voltera printer operates by dispensing silver nanoparticle ink through a 25 µm nozzle, under computer-controlled positioning. The tool enables repeatable deposition of conductive traces with high spatial precision, while also allowing reflow and curing of the printed ink under controlled heating. This method is highly suited to rapid prototyping as it avoids the need for photolithography masks and can be reprogrammed for new designs within minutes. Repeatability is ensured by calibration of dispensing pressure, nozzle height, and curing temperature, all of which can be software-controlled to maintain consistent line width and conductivity [20, 21, 22, 23].

Using the gds design illustrated in fig. 4.2, conductive ink is successfully deposited to each of the landing pads across the array, allowing for next steps of integration, as illustrated in fig. 4.5.

Figure 4.5: Microscope image of ink deposited using Voltera across the landing pad array

To integrate the VCSEL and waveguide device, two methods will be discussed. In the flip-chip method [24, 25, 26, 27], the VCSEL die is inverted and directly placed onto the substrate, with its contact pads aligned to the pre-printed conductive ink pads. Thermal curing is then performed to solidify the ink and establish electrical continuity. The main advantage of this approach is speed: it requires minimal equipment and can bond large arrays in a short time. However, a key limitation is the lack of real-time visual alignment during placement. Once the die is lowered, the position is fixed, and small lateral or rotational misalignments between the VCSEL emission aperture and the waveguide mirror can occur. Since the mode field diameter of the VCSEL is only a few microns, even sub-micron offsets translate into significant coupling losses. As a result, flip-chip assemblies often showed reduced yield, with only a subset of devices achieving efficient optical coupling.

By contrast, the transfer printing method uses a transparent polydimethylsiloxane (PDMS) stamp to first pick up the VCSEL die and then place it on the substrate [28, 29, 30]. The transparency of the PDMS allows direct visual monitoring of the die during alignment, enabling micron-scale control of both lateral and rotational placement. The flexibility of the PDMS stamp also permits controlled release of the die onto the conductive ink pads without lateral slip. This approach led to a marked improvement in coupling yield, as more VCSELs were correctly aligned to the SU8 turning mirrors. However, transfer printing introduces new process constraints. The conductive ink begins curing immediately after deposition, meaning that the die must be positioned within a narrow time window before the ink partially solidifies. If curing progresses too far before placement, poor adhesion and high contact resistance result. This introduces a trade-off between achieving optimal alignment and maintaining throughput in multi-die integration.

Using the transfer print method, integration was realised as seen in fig. 4.6, a microscope image captures the back side integration through the glass substrate. The mirror and VCSEL device is labelled to show overlap between emission aperture and coupling device.

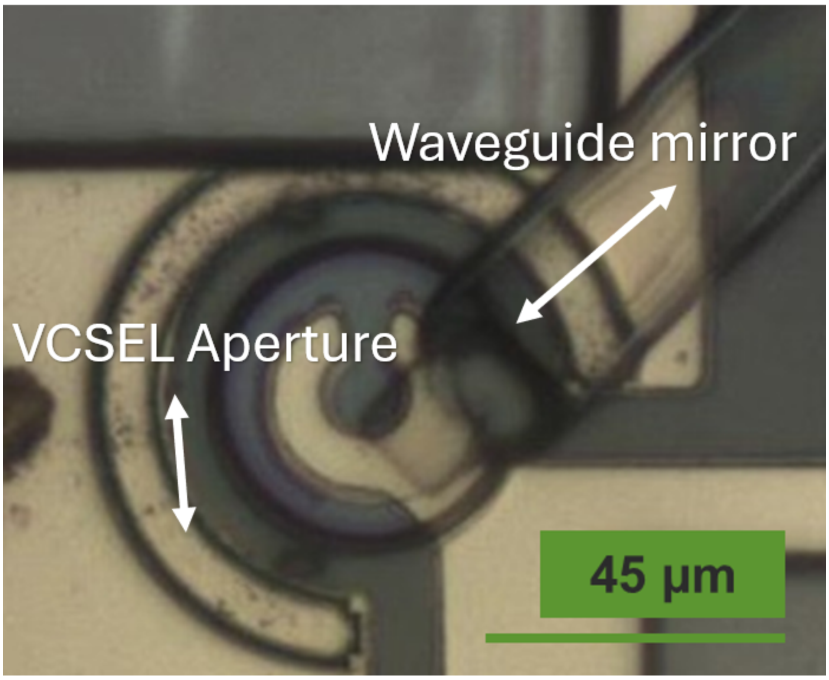

Figure 4.6: Microscope image captured through backside of glass substrate of the fully integrated coupling region

Therefore, with a fully integrated device, each individual VCSEL can be addressed and activated. The emission of a single waveguide facet with an active VCSEL is displayed in fig. 4.7.

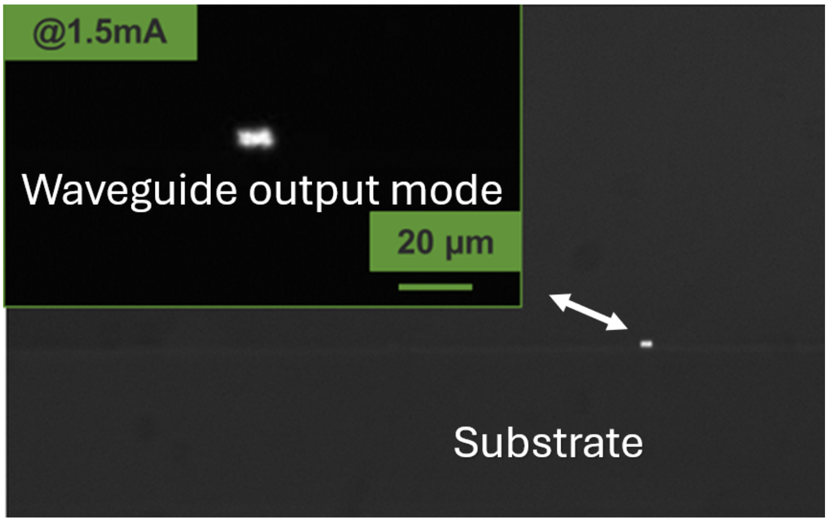

Figure 4.7: Output image captured of waveguide mode after successful VCSEL probing and coupling

With reference to fig. 4.6, the overlap between VCSEL and coupling region is not the best aligned, a factor in which draws back the flip chip method. From the image captured in fig. 4.7, the waveguide shows good illumination, however the power levels detected at high detector gain settings were less than mW. Therefore, traditional optimisation needs to be carried out for fully functional devices

4.3 μLED Integration

4.3.1 Waveguide Mirror Devices

As previously fabricated, the waveguide mirror devices utilise a combination of titanium (Ti) (50nm) and gold (Au) (200nm) to form the thin film reflective surface, which is adhered to a 45° mirror surface. However, as the wavelength decreases into the visible spectrum (particularly below 500nm), the reflectivity of gold diminishes significantly, and it begins to absorb most of the incident light [31, 32]. To enable further integration with active sources in the blue region of the visible spectrum, it is necessary to replace gold with an alternative material for the thin film reflective layer.

As a cost effective and efficient alternative, aluminium (Al) is chosen for this purpose. In the blue region of the visible spectrum, aluminium exhibits superior performance compared to gold, with reflectivity ranging from 0.80 to 0.96 for wavelengths in the blue spectrum [33, 34, 35]. This is of particular interest for the integration of GaN based μLEDs, which emit light primarily in the blue region. Furthermore, compared to gold, aluminium is also silicon foundry compatible - allowing for wafer scale devices along with the reduction of cost.

The adhesion of thin film aluminium to SU8 structures, achieved through e-beam metal evaporation, is robust and does not require an additional adhesion buffer layer. With a thickness of 100nm, the aluminium thin film achieves a reflectivity of 0.96 at a wavelength of 416nm, according to data [36].

4.3.2 μ LED Devices

The μLEDs were previously fabricated in house on a commercially available wafer, with details herein [37, 38, 39, 40, 41]. The emitted wavelength of the μLED is at 416nm with a turn on voltage around 2.8V on Si. The surface area of the μLEDs are approximately 100x100 μm^2. It is important to note that the emission area of the μLED devices is significantly larger than the mirror devices, but serves as proof of concept integration

4.3.3 Integration Method

The waveguide mirror devices were prepared as described previously, with a 100nm aluminium (Al) thin reflective film layer. To prepare the SU8 on glass receiver chip, a layer of polydimethylsiloxane (PDMS) was spun onto the sample. With a refractive index of approximately 1.41–1.43, the PDMS reduces the index contrast for the upper waveguide cladding, while still permitting effective light propagation [42]. The PDMS layer serves multiple purposes: it provides insulation between the μLED and the waveguide devices, creates the necessary spacing for light coupling into the waveguides, and acts as an adhesion layer to ensure stability during the printing process. This adhesion is crucial for maintaining the stability of the μLED during probing [43, 44, 45].

The printing method described by [ref here] uses the following process - The μLEDs are first released from their native growth substrate by selectively under-etching the underlying material, leaving the devices tethered by narrow anchors. This partial release ensures that the LEDs remain mechanically stable on the donor wafer until transfer [46].

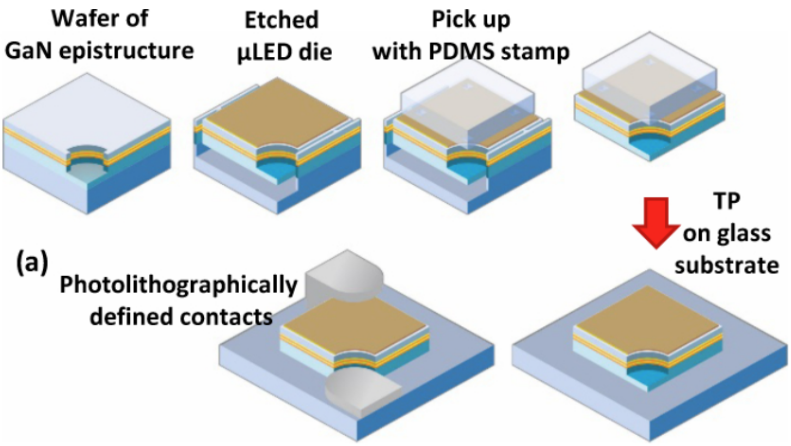

Figure 4.8: Transfer print process. Credit: [39]

A polydimethylsiloxane (PDMS) stamp is then used to pick up the released μLEDs. The viscoelastic adhesion of the PDMS enables strong attachment during a fast peel from the donor wafer, while a slow peel onto the receiver substrate allows controlled release [47, 48]. In this way, μLEDs can be accurately positioned and printed onto the target SU8 waveguide structures. The process described can be referred to fig. 4.8, where the same μLED devices are transfer printed from donor to receiver chip.

Moreover, due to the integration of the μLEDs onto the PDMS, the turn on voltage increases to 4V, as observed and detailed herein [37, 38, 39, 40, 41].

4.3.4 Results

After successful fabrication of the active μLEDs on PDMS and their integration with waveguide mirror devices, facet output monitoring was performed using methods similar to those employed for end fire optical characterisation fig. 3.2. The vertical emission was captured in fig. 4.9.

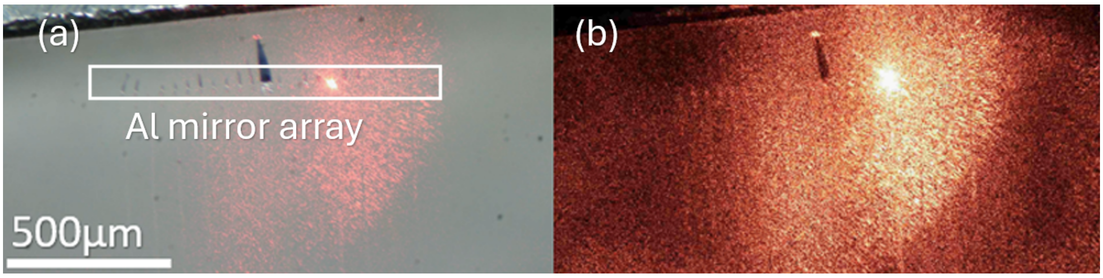

Figure 4.9: (a) illuminated microscope image of vertical beam emission from Al mirrors and (b) dark field image of vertical emission

From fig. 4.9, the vertical emission is apparent from the new Al mirrors. Fig 4.9a shows the captured beam emission with the array of mirrors labelled under direct illumination from white light. Furthermore, fig. 4.9b shows the same beam emission under a dark field setup.

To probe and activate the devices, the Moku Pro FPGA multi-instrument was used, which is a software-defined instrument that integrates arbitrary waveform generation, lock-in detection, oscilloscopes, and frequency analysis in one device [49]. Due to the previously noted increase in the turn on voltage, the voltage from the Moku was gradually ramped from 3V to 4–5V. When the voltage was increased to approximately 6V, the μLEDs failed, causing the PDMS region around the device to turn black, indicating overheating or device damage.

Facet output monitoring was conducted to detect the light emitted from the μLED and coupled into the waveguide. A single photon avalanche diode (SPAD) camera was initially used for this purpose, but it could be replaced by an optical power meter or an oscilloscope for power modulation measurements. The optical signal, modulated by a sine wave at 80MHz using the Moku.

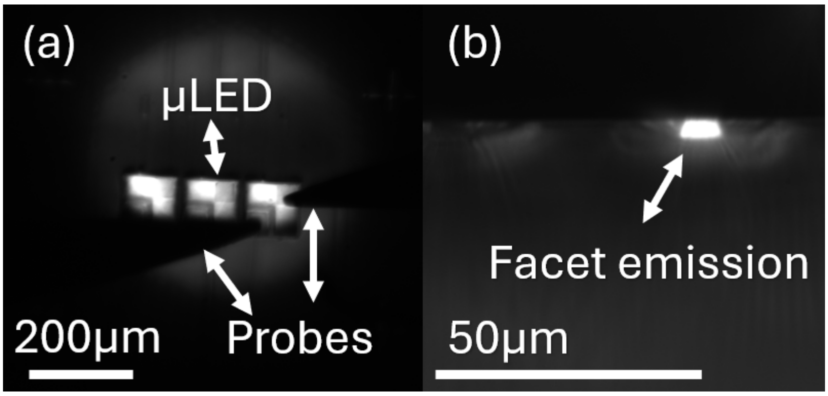

Figure 4.10: (a) µLED projection image of printed µLED on PDMS on waveguide mirror devices and (b) end facet emission of coupled light

Fig. 4.10 shows a combination of images from the direct probing of the integrated devices on waveguides (4.10a) and the imaged facet emission (4.10b). As shown in Fig. 4.10a, the devices are probed with the indicated probes. Furthermore, the end facet image from fig. 4.10b, shows the emitted mode nce the devices are activated from probing, coupled in to the waveguides and directly emitted from the free space setup. As expected, due to the challenges of free space coupling, lower waveguide cladding contrast, and numerical aperture (NA) mismatch, the overall coupling efficiency was reduced. However, this approach provides a rapid integration method, which can be further optimised to improve the coupling efficiency from the active μLED to the waveguide mirror coupling. However, it would be important to note that coupling efficiency between µLED and single mode waveguide or fibre would have lower coupling due to the poor modal overlap between the two devices.

4.4 Summary

In this chapter, the integration of active photonic sources with broadband vertical SU-8 waveguide mirror couplers has been demonstrated. Arrays of 590 µm × 590 µm waveguide mirrors were fabricated with dual-layer architectures that combined optical structures with patterned electrical interconnects. Using gold-based metallisation and conductive ink printed via a Voltera system, individually addressable channels for VC-

SEL integration were realised. Flip-chip and transfer printing methods were explored for die placement, with transfer printing offering superior alignment precision and coupling yield, though still limited by curing time and residual misalignment. Characterisation confirmed functional vertical emission, but also highlighted increased optical losses due to fabrication imperfections, proximity effects, and routing complexity.

For blue-emitting devices, aluminium thin films were introduced as reflective layers to enable efficient coupling at 416 nm. GaN-based μLEDs were successfully released, picked, and transfer printed onto SU-8 waveguide platforms via PDMS stamping. Integration on PDMS cladding enabled electrical probing and modulation using the Moku system, with facet monitoring confirming light coupling into the waveguides. While coupling efficiency remained modest due to cladding index mismatch and free-space limitations, this work demonstrates a scalable and low-cost route for integrating compact active light sources directly with broadband photonic couplers.

Overall, these results highlight the feasibility of combining active and passive photonic elements on the same platform, providing a pathway towards fully integrated optoelectronic chips.

Bibliography

[1] Chenhui Li, Srivathsa Bhat, Ripalta Stabile, Yuchen Song, Christian Neumeyr, and Oded Raz. Hybrid integration of vcsel and 3-m silicon waveguide based on a monolithic lens system. *IEEE Transactions on Components, Packaging and Manufacturing Technology*, 12(5):883–886, 2022.

[2] Yisu Yang, Gligor Djogo, Moez Haque, Peter R. Herman, and Joyce K. S. Poon. Integration of an o-band vcsel on silicon photonics with polarization maintenance and waveguide coupling. *Opt. Express*, 25(5):5758–5771, 2017.

[3] Sonia Buckley, Jeffrey Chiles, Adam N. McCaughan, Galan Moody, Kevin L. Silverman, Martin J. Stevens, Richard P. Mirin, Sae Woo Nam, and Jeffrey M. Shainline. All-silicon light-emitting diodes waveguide-integrated with superconducting single-photon detectors. *Applied Physics Letters*, 111(14):141101, 2017.

[4] Marc de Cea, Zheng Li, Milica Notaros, Jelena Notaros, and Rajeev J. Ram. Single-mode waveguide-coupled light emitting diodes in unmodified silicon photonics fabrication processes. *APL Photonics*, 8(8):081301, 2023.

[5] Jinlong Piao, Linfeng Lu, Yanzhe Wang, Yuling Ding, Jiabin Yan, Hao Zhang, Pengzhan Liu, and Yongjin Wang. Monolithic integration of light emitting diode, waveguide modulator, and photodiode on a gan-on- si led epitaxial wafer. In *2023 20th China International Forum on Solid State Lighting 2023 9th International Forum on Wide Bandgap Semiconductors (SSLCHINA: IFWS)*, pages 374–376, 2023.

[6] Tao Li, Jie Hou, Jinli Yan, Rulin Liu, Hui Yang, and Zhigang Sun. Chiplet heterogeneous integration technology—status and challenges. *Electronics*, 9(4):670, 2020.

[7] Hajdin Ceric, Roberto Lacerda de Orio, and Siegfried Selberherr. Statistical study of electromigration in gold interconnects. In *Proceedings of the 2022 IEEE International Symposium on the Physical and Failure Analysis of Integrated Circuits (IPFA)*, pages 1–5, 2022.

[8] Xue Ling, Yusheng Wang, and Xide Li. Characterization of micro-contact resistance between a gold nanocrystalline line and a tungsten electrode probe in interconnect fatigue testing. *Review of Scientific Instruments*, 85(10):104708, 2014.

[9] Srinivasan Purushothaman, S. Heeravathi, K. Arulvendhan, M. Gohul, and G. Saravanan. Coating performance prediction using a modified spin coater and the taguchi technique for solar cells. *Recent Advances in Electrical & Electronic Engineering*, 18(1):95–107, 2025.

[10] Xiao guo Feng and Lian chun Sun. Mathematical model of spin-coated photoresist on a spherical substrate. *Opt. Express*, 13(18):7070–7075, 2005.

[11] E. Kuramochi, M. Notomi, Shellene Hughes, A. Shinya, Toyohiko Watanabe, and Lora Ramunno. Disorder-induced scattering loss of line-defect waveguides in photonic crystal slabs. *Physical Review B*, 72:161318, 2005.

[12] Miloš Ljubotina, Marcus Albrechtsen, Zhe Liu, Leonardo Midolo, Andraž Debevc, Marko Topič, and Janez Krč. Origins and mitigation of scattering-related propagation losses in suspended GaAs waveguides for quantum photonic integrated circuits. *IEEE Journal of Selected Topics in Quantum Electronics*, 31:3576388, 2025.

[13] Yang Yang, Yinghui Guo, Yijia Huang, Mingbo Pu, Yanqin Wang, Xiaoliang Ma, Xiong Li, and Xiangang Luo. Crosstalk reduction of integrated optical waveguides with nonuniform subwavelength silicon strips. *Scientific Reports*, 10:4491, 2020.

[14] Mack Johnson, Mark G. Thompson, and Döndü Sahin. Low-loss, low-crosstalk waveguide crossing for scalable integrated silicon photonics applications. *Opt. Express*, 28(9):12498–12507, 2020.

[15] Weiwei Song, Robert Gatdula, Siamak Abbaslou, Ming Lu, Aaron Stein, Warren Y. C. Lai, J. Provine, R. Fabian W. Pease, Demetrios N. Christodoulides, and Wei Jiang. High-density waveguide superlattices with low crosstalk. *Nature Communications*, 6:8027, 2015.

[16] Yujie Liu, Lei Lin, Chulchae Choi, Bipin Bihari, and R.T. Chen. Optoelectronic integration of polymer waveguide array and metal-semiconductor-metal photodetector through micromirror couplers. *IEEE Photonics Technology Letters*, 13(4):355–357, 2001.

[17] Tymon Barwicz, Charles W. Holzwarth, Peter T. Rakich, Miloš A. Popović, Erich P. Ippen, and Henry I. Smith. Optical loss in silicon microphotonic waveguides induced by metallic contamination. *Applied Physics Letters*, 92(13):131108, 2008.

[18] Donghwan Ahn, Lionel C. Kimerling, and Jürgen Michel. Efficient evanescent wave coupling conditions for waveguide-integrated thin-film Si/Ge photodetectors on silicon-on-insulator/germanium-on-insulator substrates. *Journal of Applied Physics*, 110(8):083115, 2011.

[19] Yang Yang, Yinghui Guo, Yijia Huang, Mingbo Pu, Yanqin Wang, Xiaoliang Ma, Xiong Li, and Xiangang Luo. Crosstalk reduction of integrated optical waveguides with nonuniform subwavelength silicon strips. *Scientific Reports*, 10:4491, 2020.

[20] Mateusz Łysień, Łukasz Witczak, Aneta Wiatrowska, Karolina Fiączyk, Jolanta Gadzalińska, Ludovic Schneider, Wiesław Stręk, Marcin Karpiński, Łukasz Kosior, Filip Granek, and Piotr Kowalczewski. High-resolution deposition of conductive and insulating materials at micrometer scale on complex substrates. *Scientific Reports*, 12:9327, 2022.

[21] Amal M. Al-Amri. Recent progress in printed photonic devices: A brief review of materials, devices, and applications. *Polymers*, 15(15):3234, 2023.

[22] Iara J. Fernandes, Angélica F. Aroche, Ariadna Schuck, Paola Lamberty, Celso R. Peter, Willyan Hasenkamp, and Tatiana L. A. C. Rocha. Silver nanoparticle conductive inks: synthesis, characterization, and fabrication of inkjet-printed flexible electrodes. *Scientific Reports*, 10:65698, 2020.

[23] Geoffrey Rivers, Jonathan S. Austin, Yinfeng He, Adam Thompson, Negar Gilani, Nathan Roberts, Peng Zhao, Christopher J. Tuck, Richard J.M. Hague, Ricky D. Wildman, and Lyudmila Turyanska. Stable large area drop-on-demand deposition of a conductive polymer ink for 3d-printed electronics, enabled by bio-renewable co-solvents. *Additive Manufacturing*, 66:103452, 2023.

[24] Guojiong Li, Xiangyang Dai, Yuanhao Zhang, Liyuan Song, Panpan Yu, Minwen Xiang, Can Liu, Juan Xia, Qiaoyin Lu, and Weihua Guo. A novel hybrid photonic integration scheme based on flip-chip bonding combined with vertical coupling. *IEEE Photonics Journal*, 17(3):1–7, 2025.

[25] Huihui Lu, Jun Su Lee, Yan Zhao, Carmelo Scarcella, Paolo Cardile, Aidan Daly, Markus Ortsiefer, Lee Carroll, and Peter O'Brien. Flip-chip integration of tilted vcsels onto a silicon photonic integrated circuit. *Opt. Express*, 24(15):16258–16266, 2016.

[26] Sudip Shekhar, Wim Bogaerts, Lukas Chrostowski, John E. Bowers, Michael Hochberg, Richard Soref, and Bhavin J. Shastri. Roadmapping the next generation of silicon photonics. *Nature Communications*, 15:751, 2024.

[27] Ibrahim Murat Soganci, Antonio La Porta, and Bert Jan Offrein. Flip-chip optical couplers with scalable I/O count for silicon photonics. *Optics Express*, 21(13):16075–16085, 2013.

[28] Benoit Guilhabert, Sean P. Bommer, Nils K. Wessling, Dimitars Jevtics, Jack A. Smith, Zhongyi Xia, Saptarsi Ghosh, Menno Kappers, Ian M. Watson, Rachel A.

Oliver, Martin D. Dawson, and Michael J. Strain. Advanced transfer printing with in-situ optical monitoring for the integration of micron-scale devices. *IEEE Journal of Selected Topics in Quantum Electronics*, 29(3):1–11, 2023.

[29] J. A. Smith, D. Jevtics, B. Guilhabert, M. D. Dawson, and M. J. Strain. Hybrid integration of chipscale photonic devices using accurate transfer printing methods. *Applied Physics Reviews*, 9(4):041317, 2022.

[30] Nils Kolja Wessling, Saptarsi Ghosh, Benoit Guilhabert, Menno Kappers, Rachel A. Oliver, Martin D. Dawson, and Michael J. Strain. Integration of single gan microlenses with high index semiconductors by transfer printing. In *Conference on Lasers and Electro-Optics*, page JW3A.35. Optica Publishing Group, 2022.

[31] Zihao Lin, Yuxiang Long, Xupeng Zhu, Peng Dai, Feng Liu, Mengjie Zheng, Yanming Zhou, and Huigao Duan. Extending the color of ultra-thin gold films to blue region via fabry-pérot-cavity-resonance-enhanced reflection. *Optik*, 178:992–998, 2019.

[32] Sara Zuccon, Enrico Napolitani, Enrico Tessarolo, Paola Zuppella, Alain Corso, Francesca Gerlin, Marco Nardello, and Maria Guglielmina Pelizzo. Effects of helium ion bombardment on metallic gold and iridium thin films. *Optical Materials Express*, 5:176–187, 2014.

[33] H. E. Bennett, Jean M. Bennett, and E. J. Ashley. Infrared reflectance of evaporated aluminum films. *J. Opt. Soc. Am.*, 52(11):1245–1250, 1962.

[34] Robert Lugolole and Sam Obwoya Kinyera. The effect of thickness of aluminium films on optical reflectance. *Journal of Ceramics*, 2015:1–6, 2015.

[35] Paul Schmitt, Sven Stempfhuber, Nadja Felde, Adriana V. Szeghalmi, Norbert Kaiser, Andreas Tünnermann, and Stefan Schwinde. Influence of seed layers on the reflectance of sputtered aluminum thin films. *Opt. Express*, 29(13):19472–19485, 2021.

[36] Mikhail N. Polyanskiy. Refractiveindex.info database of optical constants. *Scientific Data*, 11:94, 2024.

[37] J. F. C. Carreira, A. D. Griffiths, E. Xie, B. J. E. Guilhabert, J. Herrnsdorf, R. K. Henderson, E. Gu, M. J. Strain, and M. D. Dawson. Direct integration of micro-LEDs and a SPAD detector on a silicon CMOS chip for data communications and time-of-flight ranging. *Optics Express*, 28(5):6909–6917, 2020.

[38] J. F. C. Carreira, E. Xie, R. Bian, C. Chen, J. J. D. McKendry, B. Guilhabert, H. Haas, E. Gu, and M. D. Dawson. On-chip gan-based dual-color micro-led arrays and their application in visible light communication. *Opt. Express*, 27(20):A1517–A1528, 2019.

[39] K. Rae, P. P. Manousiadis, M. S. Islim, L. Yin, J. Carreira, J. J. D. Mckendry, B. Guilhabert, I. D. W. Samuel, G. A. Turnbull, N. Laurand, H. Haas, and M. D. Dawson. Transfer-printed micro-led and polymer-based transceiver for visible light communications. *Opt. Express*, 26(24):31474–31483, 2018.

[40] A. J. Trindade, B. Guilhabert, D. Massoubre, D. Zhu, N. Laurand, E. Gu, I. M. Watson, C. J. Humphreys, and M. D. Dawson. Nanoscale-accuracy transfer printing of ultra-thin AlInGaN light-emitting diodes onto mechanically flexible substrates. *Applied Physics Letters*, 103(25):253302, 2013.

[41] Pengfei Tian, Jonathan J. D. McKendry, Zheng Gong, Shuailong Zhang, Scott Watson, Dandan Zhu, Ian M. Watson, Erdan Gu, Anthony E. Kelly, Colin J. Humphreys, and Martin D. Dawson. Characteristics and applications of micro-pixelated GaN-based light emitting diodes on Si substrates. *Journal of Applied Physics*, 115(3):033112, 2014.

[42] Zhiyi Zhang, Ping Zhao, George Xiao, Benjamin Watts, and Changqing Xu. Sealing su-8 microfluidic channels using pdms. *Biomicrofluidics*, 5:46503–465038, 2011.

[43] Xinming Wang, Yuting Zhao, Heming Li, Weiguo Gao, Yan Liu, Anning Sun, Ke Ma, Zhizhi Hu, and Yongqi Wang. Adhesion and transparency enhancement be-

tween flexible polyimide-PDMS copolymerized film and copper foil for LED transparent screen. *Polymers*, 16(11):1591, 2024.

[44] Shaojie Zhou, Biwei Meng, and Chao Yuan. Polydimethylsiloxane (PDMS)-assisted non-destructive transient thermoreflectance characterizations. *Review of Scientific Instruments*, 95(5):053003, 2024.

[45] Sara Hassanpour-Tamrin, Amir Sanati-Nezhad, and Arindom Sen. A simple and low-cost approach for irreversible bonding of polymethylmethacrylate and polydimethylsiloxane at room temperature for high-pressure hybrid microfluidics. *Scientific Reports*, 11:4821, 2021.

[46] Eleni Margariti, Gemma Quinn, Dimitars Jevtics, Benoit Guilhabert, Martin D. Dawson, and Michael J. Strain. Continuous roller transfer-printing and automated metrology of $>$75,000 micro-LED pixels in a single shot. *Optical Materials Express*, 13(8):2236–2250, 2023.

[47] Changhong Linghu, Shun Zhang, Chengjun Wang, and Jizhou Song. Transfer printing techniques for flexible and stretchable inorganic electronics. *npj Flexible Electronics*, 2:37, 2018.

[48] Daekyeong Jung, Taeksu Lee, Jaejong Lee, Jaegu Kim, Jaehyun Kim, and Hyungjun Lim. Selective transfer of light-emitting diodes onto a flexible substrate via laser lissajous scanning. *ACS Omega*, 5(43):27749–27755, 2020. PMID: 33163757.

[49] Zhongyi Xia, Dimitars Jevtics, Benoit Jack Eloi Guilhabert, Jonathan J. D. McKendry, Qian Gao, Hark Hoe Tan, Chennupati Jagadish, Martin D. Dawson, and Michael John Strain. Modulation of nanowire emitter arrays using micro-led technology. *ACS Nano*, 19(16):15813–15819, 2025. PMID: 40241407.

Chapter 5

Outlook

This thesis has explored the design, fabrication, and integration of broadband vertical coupling devices for photonic integrated circuits (PICs), with a focus on low-cost polymer platforms. Across the chapters, SU-8 waveguides and 45° vertical mirror couplers were established as practical, scalable solutions for broadband fibre-to-chip coupling. Through a combination of simulation, grayscale lithography, and experimental characterisation, these devices demonstrated low propagation and coupling losses across the visible and infrared bands, validating their potential as alternatives to conventional grating couplers.

The work extended beyond passive device development to integration with active sources. Arrays of waveguide mirror receivers were fabricated and equipped with electrical interconnects for 850 nm VCSELs, using both flip-chip and transfer printing techniques. Transfer printing showed improved alignment fidelity, although alignment tolerances and conductive ink curing times remain bottlenecks. At shorter wavelengths, aluminium-coated mirrors were introduced to support integration of 416nm GaN-based μLEDs. Transfer-printed μLEDs were successfully probed and coupled into SU-8 waveguides, with optical monitoring confirming vertical emission and waveguide coupling. These demonstrations highlight the feasibility of combining passive broadband couplers with active light sources on a single, low-cost platform.

Looking forward, the next steps involve improving fabrication precision and reproducibility to bring device performance closer to the theoretical limits predicted by simulation. While grayscale lithography and PDMS-based transfer printing have enabled rapid prototyping of complex three-dimensional structures, yield and uniformity are currently limited by exposure variations, proximity effects, and alignment tolerances. Incorporating enhanced process control strategies, such as in-situ dose calibration, proximity effect correction, and optimised resist formulations, could significantly reduce these issues and improve device repeatability.

Grayscale lithography in particular offers substantial scope for extending the functionality of the demonstrated platform. Beyond the planar and tilted mirror structures explored in this work, the technique could be exploited to realise three-dimensional polymer micro-optical elements, including integrated microlenses for beam collimation, focusing, or numerical aperture matching between waveguides and external sources. Such microlenses could be monolithically aligned to the vertical mirror couplers, reducing divergence losses and improving overall coupling efficiency, particularly for incoherent or highly multimode emitters such as LEDs. In addition, similar micro-optical elements could be used to focus or reshape optical beams onto integrated photodetectors. By combining grayscale microlenses with transfer printing or flip-chip integration of detector devices, it would be possible to improve optical mode matching, enhance responsivity, and relax alignment tolerances in receiver architectures.

Further investigation of mirror geometries represents another important direction for future research. While the 45° planar mirror has proven effective for broadband and multimode operation, it is fabricated using a 2.5D grayscale lithography approach, in which the mirror angle is defined through a controlled height profile rather than a fully three-dimensional surface. Within this fabrication paradigm, alternative mirror profiles could be explored by engineering the grayscale height distribution in combination with lateral patterning. In particular, parabolic or stepped beam-shaping mirrors could enable improved mode control and higher coupling efficiency while retaining the relative simplicity and scalability of the fabrication process. Such structures may allow the reflected field to be tailored for improved overlap with specific fibre modes or detector apertures, or to suppress higher-order modes for more selective operation. A systematic study comparing planar and engineered 2.5D mirror profiles would provide valuable insight into the trade-offs between fabrication complexity, bandwidth, and modal purity.

Grayscale lithography could also be employed as a method for local or global planarisation within polymer photonic platforms. Controlled grayscale exposure could be used to smooth topographical variations arising from multi-layer integration, mirror formation, or transfer-printed active devices. Improved planarisation would benefit subsequent lithographic steps, enhance cladding uniformity, and reduce scattering losses caused by surface roughness or step discontinuities. This would improve both optical and electrical reliability.

Another important future direction is scaling the demonstrated devices towards wafer-level fabrication and packaging. Practical deployment of photonic integrated circuits requires not only efficient coupling but also compatibility with automated assembly, passive alignment, and high-throughput manufacturing. The use of polymer-based grayscale structures, combined with transfer printing of active devices, is well suited to such environments, but further work is required to improve alignment tolerance windows, reflective coating durability, and long-term mechanical stability.

Finally, while this thesis has demonstrated operation across a wide spectral range from 416 to 1630 nm, extending these concepts to other wavelength regimes remains an attractive opportunity. Grayscale-defined mirrors and micro-optics could be adapted for ultraviolet applications such as biosensing and lab-on-chip diagnostics, as well as longer-wavelength systems including short-wave and mid-infrared photonics for environmental monitoring and spectroscopy. In these regimes, the ability to rapidly prototype broadband coupling structures using low-cost materials could provide a significant advantage over conventional planar coupling approaches.

In summary, this thesis has shown that low-cost, broadband SU-8 vertical mirror couplers can bridge the gap between optical fibres, free space, and integrated photonics. By demonstrating both passive coupling and active source integration, the work points towards a new generation of fully integrated optoelectronic chips that are scalable, versatile, and manufacturable. With continued development of grayscale lithography for micro-optics, beam shaping, and planarisation, alongside improvements in alignment strategies and packaging, these devices have the potential to play a central role in the evolution of photonic integrated circuits beyond conventional platforms.